NASA CONTRACTOR REPORT
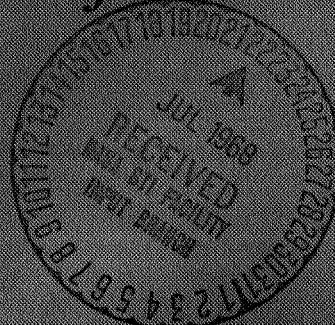
A STUDY OF FULLY-MANUAL AND AUGMENTED-MANUAL CONTROL SYSTEMS FOR THE SATURN V BOOSTER USING ANALYTICAL PILOT MODELS

by H. R. Jex, G. L. Teper, D. T. McRuer, and W. A. Johnson

Prepared by
SYSTEMS TECHNOLOGY, INC.
Hawthorne, Calif.
for Ames Research Center

NATIONAL AERONAUTICS AND SPACE ADMINISTRATION • WASHINGTON, D. C. • JULY 1968

A STUDY OF FULLY-MANUAL AND AUGMENTED-MANUAL

CONTROL SYSTEMS FOR THE SATURN V BOOSTER

USING ANALYTICAL PILOT MODELS

By H. R. Jex, G. L. Teper, D. T. McRuer, and W. A. Johnson

NATIONAL AERONAUTICS AND SPACE ADMINISTRATION

SUMMARY

The preliminary design of manual control systems for large flexible boosters of the Saturn V class was investigated by manual control systems analysis techniques. The approach employed empirically based mathematical models for the pilot (including quasi-linear describing functions and remnant); mission-derived design criteria and constraints; and a set of efficient control system analysis and synthesis tools. Most of the study was done as an analytical supplement to a concurrent large scale simulation program on related problems at the Ames Research Laboratory.

Two roles for the pilot were studied in detail: fully-manual control and a series pilot plus stability-augmented booster. The control system characteristics evolved included the different describing functions likely to be adopted by the pilot, and the best loop structure from the criteria of simplicity, good handling qualities, wind load relief, and attenuation of the pilot's remnant.

It was shown that fully-manual control of one axis was feasible, but that tracking performance, load relief, and handling would be poor. The augmented-manual control system included lead-double-lag pitch equalization in the inner loop, an integrating filter downstream of the pilot in the outer loops, and pilot-selected switching between trajectory and load relief control modes by shifting his attention from the attitude to the accelerometer display. The augmented system combined good pitch attitude tracking with substantial load relief, excellent remnant rejection, good handling qualities, and a simple fixed-equalization system.

Appendices contain: a synopsis of the analysis techniques used, the "Sawtooth Bode" criterion for bending mode suppression, and some specialized data on pilot remnant.

CONTENTS

TABLES

FIGURES

viii

NOTATION

c.g.	Center of gravity
C_1	First bending mode weighting coefficient at attitude gyro location
C_2	Second bending mode weighting coefficient at attitude gyro location
C_3	First bending mode weighting coefficient at rate gyro location
C_4	Second bending mode weighting coefficient at rate gyro location
D	Total drag force, kg
$\left.\begin{array}{c} F_\alpha \\ F_\beta \\ F_\varphi \end{array}\right\}$	Time-varying force coefficients
g	Acceleration due to gravity at sea level, 9.8 m/sec^2
g'	Vehicle's longitudinal acceleration, m/sec^2
$H_n(j\omega)$	Filter transfer function of filter used to approximate remnant spectra
ICR	Instantaneous center of rotation
j	$\sqrt{-1}$
K	Static gain, generally
K_c	Controlled element gain
K_d	Attitude displacement gain
K_E	Equalization gain
K_p	Pilot's gain
K_{p_A}	Pilot's gain in fully manual attitude control loop
K_{p_C}	Pilot's gain in series pilot/augmented-vehicle attitude control loop
$K_{p\ddot{\gamma}}$	Pilot's gain in load relief loop
K_r	Attitude rate gain
K_1	First bending mode shape coefficient at accelerometer station
K_2	Second bending mode shape coefficient at accelerometer station

K_3	First bending mode shape coefficient at pilot's station
K_4	Second bending mode shape coefficient at pilot's station
l_a	Distance from vehicle c.g. to load relief accelerometer, m
l_p	Distance from vehicle c.g. to pilot's station measured along vehicle centerline, m
M	Total vehicle mass, kg
M_α, M_β	Time-varying moment coefficient
M_{des}	Design bending moment, kg·m
M_x	Bending moment at vehicle station x, kg·m
n	Pilot's remnant contribution, referred to a specified point of injection
$N_{(\ )_i}$	Numberator of vehicle transfer function identified by $(\ )_i$
q	Dynamic pressure, kg/m^2
rms	Root mean square value
s	Laplace transform operator
t	Time, sec
T	Total thrust, kg
T	Time constant
$T_L \begin{cases} \\ \end{cases}$	Pilot's lead time constant (for fully manual system) Controller lead time constant (for augmented manual system)
T_1	g'/V
T_2	Vehicle time constant with ideal pitch control, sec
V	Vehicle velocity, m/sec
W	Total vehicle weight, kg
x	Vehicle position normal to flight path, m
x	Station along vehicle centerline measured from geocenter, m
Y	Transfer function, in general
Y_c	Controlled element transfer function

Y_{CL} — Closed-loop transfer function

$Y_{D\varphi}$ — Attitude display transfer function

$Y_{D\ddot{\gamma}_a}$ — Acceleration display transfer function

Y_E — Equalization transfer function

Y_{OL} — Open-loop transfer function

Y_p — Human pilot's describing function

Y_{p_A} — Pilot's describing function in fully manual attitude control loop

Y_{p_C} — Pilot's describing function in series pilot/augmented-vehicle attitude control loop

$Y_{p\ddot{\gamma}}$ — Pilot's describing function in load relief loop

$Y_{\ddot{\gamma}_p^E}$ — $\ddot{\gamma}_p^E/\beta_c$

$Y_{\ddot{\gamma}_p^R}$ — $\ddot{\gamma}_p^R/\beta_c$

$Y_{\varphi_{AG}}$ — φ_{AG}/β_c

$Y_{\varphi_{RG}}$ — φ_{RG}/β_c

$Y_{\dot{\varphi}_{RG}}$ — $\dot{\varphi}_{RG}/\beta_c$

α — Angle of attack, deg

α_w — Wind angle of attack, deg

β — Rocket gimbal angle, deg

β_c — Gimbal command to servo, deg

β_ϵ — Gimbal error, deg

β_f — Gimbal command from feedback loop, deg

β_p — Gimbal command resulting from pilot's control, deg

$\ddot{\gamma}_a$ — Normal acceleration sensed at accelerometer location, m/sec^2

$\ddot{\gamma}_c$ — Command normal acceleration, m/sec^2

$\ddot{\gamma}_D$ — Normal acceleration error at display, cm

$\ddot{\gamma}_\epsilon$	$\ddot{\gamma}_c - \ddot{\gamma}_a$
$\ddot{\gamma}_p^E$	Normal acceleration at pilot's station due to elastic modes, m/sec^2
$\ddot{\gamma}_p^R$	Normal acceleration at pilot's station due to rigid-body modes, m/sec^2
δ	Pilot's stick deflection, deg.
$\triangle$	Denominator of vehicle transfer function
$\triangle'$	Denominator of vehicle if one feedback loop is closed
$\triangle''$	Denominator of vehicle if two feedback loops are closed
ζ	Damping ratio
ζ_N	Damping ratio of pilot's neuromuscular system characteristics
η_1	First generalized elastic bending mode coordinate
η_2	Second generalized elastic bending mode coordinate
κ	Root locus gain, in general
μ	Bending moment criterion
ρ	Density, kg/m^3
σ_n	Root mean square value of remnant input
$\sigma_{\ddot{\gamma}_p^E}$	Root mean square value of transverse acceleration at pilot's station due to elastic modes, m/sec^2
$\sigma_{\ddot{\gamma}_p^R}$	Root mean square value of transverse acceleration at pilot's station due to rigid-body modes, m/sec^2
τ	Reaction time delay, sec
τ_e	Effective reaction time delay, sec
φ	Pitch attitude angle, deg
$\triangle\varphi$	Pitch attitude error, deg
φ_c	Pitch attitude command, deg
φ_d	Pitch attitude error at display, cm
φ_D	Pitch error at the attitude display, cm
φ_m	Phase margin

φ_{AG} Attitude sensed at the attitude gyro location, deg

φ_{RG} Attitude sensed at the rate gyro location, deg

$\dot{\varphi}_{RG}$ Attitude rate sensed at the rate gyro location, deg/sec

$\Phi_i(\omega)$ Input power spectral density

$\Phi_o(\omega)$ Output power spectral density

Φ_{nn_e} Remnant power spectral density

$\Phi_{\ddot{\gamma}E_p}$ Power spectral density of normal acceleration at pilot's station due to elastic modes which are excited by the remnant

$\Phi_{\ddot{\gamma}R_p}$ Power spectral density of normal acceleration at pilot's station due to rigid-body modes which are excited by the remnant

ω Frequency, rad/sec

ω_c Crossover frequency, rad/sec

ω_i Input or forcing function bandwidth, rad/sec

ω_n Remnant spectra filter break frequency, rad/sec

ω_{n_1} Undamped natural frequency of first bending mode, rad/sec

ω_{n_2} Undamped natural frequency of second bending mode, rad/sec

ω_N Undamped natural frequency of pilot's neuromuscular system characteristics, rad/sec

      The dimensional units used are consistent with the equations of motion and data provided by the Ames Research Center, which were originally supplied by the Marshall Space Flight Center. They correspond to the following form of Newton's second law of motion:

$$F = \frac{ma}{g}$$

where   F   is expressed in kilograms of force

        m   is expressed in kilograms of mass

        a   is the acceleration in meters per second

        g   is the "standard acceleration of gravity," namely, $9.8 \ m/sec^2$

SECTION I

INTRODUCTION

Several large scale studies of manual booster control have been made during the past few years (Refs. 1 — 6). In all but one (Ref. 2) the emphasis has been on simulation. The present study was initiated to introduce more analytical efforts as a supplement to simulation. There were good reasons to hope that analytical procedures could materially increase the efficiency, understanding, and generality of simulation efforts. Further, there was a desire to establish how well analysis could play an independent role, especially in the earlier stages of preliminary design when detailed simulation is not yet feasible.

A variety of systems analysis techniques for designing manual control for manned vehicles have recently been developed at Systems Technology, Inc., and elsewhere (e.g., Refs. 7 — 11). A basic purpose of this study was to apply these techniques to a booster problem. Particular emphasis was to be placed on application of human-pilot response models to the functional characteristics of the manual control system for a large booster of the Saturn V class. Secondary goals included the specification of both "minimal" and "good" manual control system functional characteristics, and the determination of the resulting wind load and vibratory disturbance of the pilot with these systems.

From the program outset it was intended that these analytical results be compared with empirical results obtained from a concurrent Ames Research Center simulation program along similar lines. To keep the comparison between the analytical and empirical synthesis processes as valid as possible, the study reported herein was performed with the same ground rules and design criteria as the Ames simulation effort. So that the analysis activities could be assessed as a completely separate entity of the design process, none of the simulation results were made available to the analytical team in the course of the initial study. Then, near the end, some of the Ames data were made available, and the final system iteration was completed. Of course, this procedure is not generally desirable,

since both analysis and simulation gain much by interaction and complete integration — but in the present instance it led to a reasonably independent validation of the analytical approach.

A report such as this cannot be presented with smoothly flowing continuity; frequent digressions, footnotes, and appendices are required to provide the scarce material or to explain unaccustomed assumptions. To help provide an overview of the report, and to aid in selective reading, a Synopsis showing the relationship of one section to another is given below.

SYNOPSIS
(Showing the relationships among the various sections)
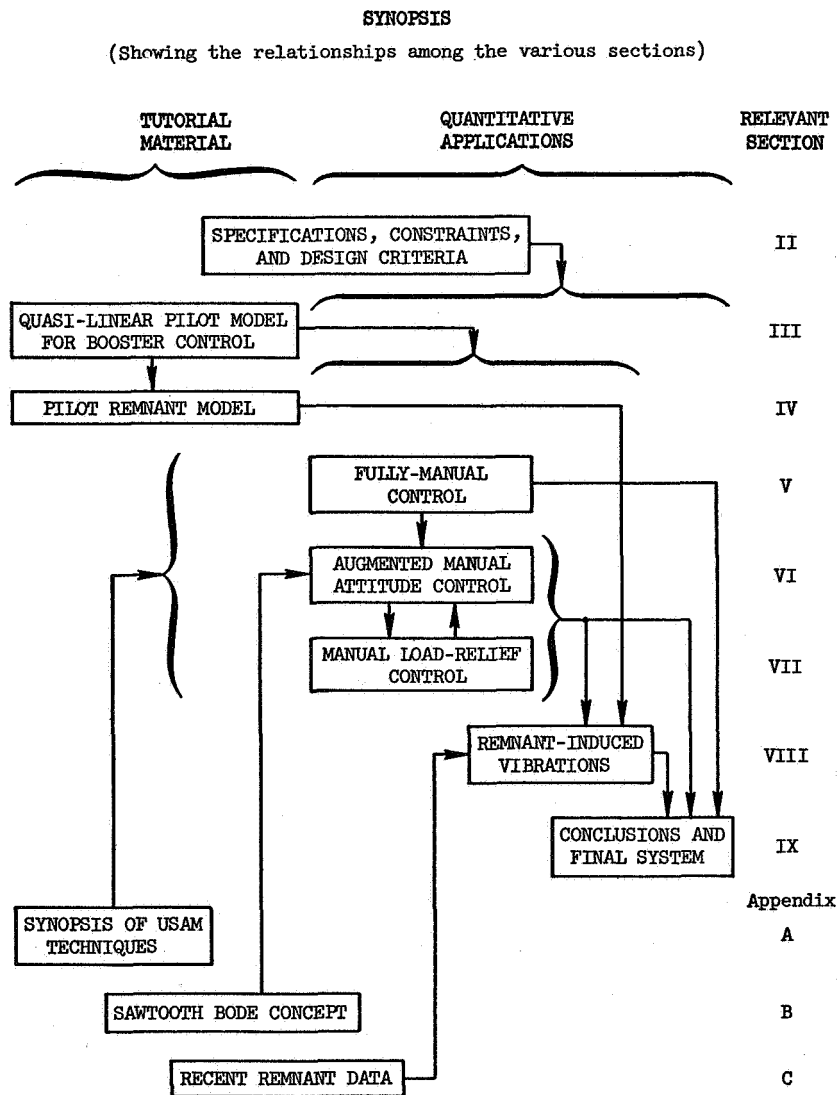
SECTION II

SPECIFICATIONS

Well-defined ground rules, system inputs, performance criteria and constraints, and desired design qualities are essential to any synthesis effort; those set up for this manual-control-of-boost study are presented below.

A. GROUND RULES

1. General Situation

The situation involved is the manual control of a large flexible booster up to first-stage burnout. The effectiveness and feasibility of manual control will be determined by comparing fully manual and augmented manual control. Performance quantities of interest include the vehicle attitude errors in following guidance commands, the bending moments resulting from flight through the wind disturbances, the vibratory accelerations felt by the pilot, and the required thrust deflection angles.

2. Booster

A booster of the Saturn V class was selected as the study vehicle. The overall configuration and some pertinent dimensional data are shown in Fig. 1. Equations of motion, dimensional data, and the inertial, aerodynamic, and structural data were originally supplied to Ames Research Center by the Marshall Space Flight Center. These data are reproduced in Tables I and II. The equations are written in "aero-ballistic" axes, in which the axes are pitched along the desired gravity-turn flight path.

3. Degrees of Freedom

The vehicle dynamics involve two rigid-body degrees of freedom (plunging and pitching), and two structural bending modes. Fuel slosh was elimi-nated on the basis of previous studies at the Ames Research Center which

3

indicated that the slosh dynamics were not a dominant problem in the design of the first-stage manual control system. The engine actuator (servo) dynamics are approximated by a third-order system.

4. Design Conditions

The key design flight condition was near maximum dynamic pressure (t = 77 sec from launch). At this condition both attitude control and load relief from wind spikes were to be considered. The unstable vehicle dynamics are the most difficult to control at this condition and it is also the most critical from a structural standpoint. Consequently, the control systems evolved were to emphasize this flight condition in any of the tradeoffs considered enroute to a balanced design. However, the systems were also to be satisfactory for control near launch (t = 10 sec) and burnout (t = 150 sec).

5. Sensor Locations

Prescribed locations for the attitude and the rate gyros had been fixed as shown in Fig. 1. The accelerometer positions available are shown by the shaded bars. Also shown in Fig. 1 is the center of gravity at each of the three flight conditions.

6. Exclusions

Beyond the foregoing ground rules, the following items were specified as being outside the scope of this study:

> Axial modes (i.e., "pogo stick" modes)
> Engine failure conditions
> Atmospheric turbulence effects
> Guidance laws
> All detailed hardware design aspects

4

B. SYSTEM INPUTS

1. Guidance Commands

The booster is assumed to be flying a nominal attitude pitch-over program, as shown in Fig. 2a. Following lift-off, this program provides a period of nearly constant pitching acceleration initiated at t = 10 sec, which subsequently approaches a conventional gravity turn for the remainder of the flight. During first-stage flight, the flight path angle changes from vertical (90 deg) to somewhat above horizontal (approximately 25 deg), while the commanded pitch rate never exceeds 1 deg/sec.

Over and above this basic guidance command, load relief was to be accomplished as required by strength limitations and by wind-induced loads; however, load relief is not considered a guidance function as such.

2. Disturbances

The only specific disturbance to be considered here was a typical large wind spike near the maximum dynamic pressure condition, as shown in Fig. 2b. Previous studies, e.g., Ref. 12, have shown that the dominant booster bending stresses result from such large scale wind spikes rather than the finer-grained wind variations which are usually attributed to turbulence.

One other disturbance which has little effect on the trajectory but which has been found to produce significant vibratory accelerations at the cockpit, is inadvertent control motion by the pilot. Inadvertent pilot outputs are those which are not necessary to make the booster follow the guidance command or to cope with the wind disturbance, but are the unavoidable result of such control participation by the pilot. They are included in the "remnant" term in pilot mathematical models, as will be explained later.

5

C. PERFORMANCE CRITERIA AND CONSTRAINTS

1. Attitude Tracking Accuracy

One key performance criterion was that the closed-loop manually controlled system should closely follow the commanded attitude program. Although no specific numerical criterion was given, the implied specification was that the closed-loop output should equal the commanded input, over the effective bandwidth of the guidance commands. Therefore a closed-loop tracking performance criterion was established as follows:

$$\varphi/\varphi_c \; = \; 1.0 \pm 0.1 \;\; \text{for} \;\; \omega_i \; < \; 0.1 \; \text{rad/sec}$$

or, in terms of decibels,

$$\varphi/\varphi_c \; \doteq \; 0 \; \text{dB} \pm 1 \; \text{dB} \;\; \text{for} \;\; \omega_i \; < \; 0.1 \; \text{rad/sec}$$

So that malfunction detection can be based on concrete limits, the maximum transient deviation from the nominal guidance program was to be limited to less than

$$\text{Transient} \; \Delta\varphi \; \leq \; 15 \; \text{deg}$$

2. Bending Moment Criterion

The aerodynamic loads which are imposed along the booster, plus the side loads due to engine (thrust) deflection, produce a bending-moment distribution which varies along the length of the vehicle. Even when a wide variety of loadings are considered, the maximum structural bending moments resulting from wind spike disturbances occur at, or near, the same axial location on the booster. This permits an approximate design limit to be established in terms of a combination of dynamic pressure, angle of attack, gimbal deflection, and bending mode deflections. The resulting ratio of bending moment to the design bending moment is called

6

"μ" herein, and is defined numerically in Table I. The performance constraint on μ was specified as:

$$\mu = \frac{M_x}{M_{des}} \leq 0.75$$

3. Transverse Cockpit Vibrations

Slight movements of the thrust vector at frequencies near the bending modes can excite considerable transverse accelerations at the pilot's station, depending on the proximity of that station to the mode deflection antinodes. The accelerations felt by the pilot due to the bending vibrations occur at frequencies where only small fractions of a "g" are tolerable (Ref. 13). Accordingly, a specific vibration constraint was imposed, namely

$$\ddot{\gamma}_P^E \leq \pm 0.1g$$

4. Thrust Vector Control Angle

When the thrust vector command exceeds the gimbal travel limits, the closed-loop system becomes essentially open loop. Without closed-loop control an aerodynamically unstable booster tends to diverge. To avoid such operation, the commanded thrust vector angle is limited to levels well below its physical travel limits. Based on the Saturn V engine limits, the command limit was set at:

$$\beta_c \leq 5 \text{ deg}$$

D. DESIGN QUALITIES

A number of important design qualities which do not fall in the category of performance requirements or constraints, but which are of equal importance as either specified or implied requirements, are briefly summarized below.

1. Minimum Complexity

Simplicity is a primary factor in achieving good reliability and straightforward development of the overall control system. Specific design qualities sought here were:

> Minimum number of components in the automatic flight control system
>
> Fixed equalization networks, where possible
>
> Minimum amount of gain changing

2. Minimal Design Parameter Sensitivity

One of the marks of a good control system design, and in fact the primary reason for using feedback in most cases, is to make its performance insensitive to changes in the control system and vehicle parameters. Such a constraint often precludes the use of highly tailored devices such as fixed-parameter notch filters or fixed blending of multiple gyros.

3. Handling Qualities

Because all the systems considered here have the pilot in the loop, a specification on the handling qualities is essential. For this purpose the Cooper rating scale (Ref. 14) is used. This scale orders the vehicle characteristics into nine categories, ranging from "excellent, includes optimum" (1.0) to "unacceptable-uncontrollable" (9.0). The key dividing points on the scale occur at 3.5, between "satisfactory" and "acceptable, but with unpleasant characteristics" and at 6.5, between "acceptable for emergency condition only (failure of a stability augmenter)" and "unacceptable even for emergency condition."

Thus, for the fully manual system considered here (in which the pilot is in full command of one axis during an emergency, with no stability augmentation) the specification was that the simulated system would be considered "flyable" only if it would achieve a Cooper rating of better than 6.5. For a "good" system, suitable for operating in all axes simultaneously with the aid of an augmented

and equalized vehicle, Cooper ratings of less than 3.5 were required. A subsidiary handling qualities specification was that with a "good" system, all axes should be simultaneously controllable with the pilot in the loop. With the fully manual system, only one axis at a time would have to be controlled. A situation in which all axes required manual control would be considered as an abort.

4. Efficient Manual/Automatic Interface

Various levels of pilot participation versus automatic control participation were to be considered, starting from fully manual control to a minimum pilot role.

All the specifications discussed were obtained from the sponsor either directly or by implication at the outset of the study.

SECTION III

A QUASI-LINEAR PILOT MODEL FOR BOOSTER CONTROL

A. GENERAL APPROACH

The pilot's goals as an element in the booster guidance/control loop are: to cause the booster to follow the guidance command accurately; to compensate for any instabilities which might be present; and to correct for gust disturbances; all while avoiding unstable coupling with the relatively low-frequency booster bending modes. To estimate the pilot's dynamic behavior in a given system configuration a mathematical model, which has parameters adjusted in conformance with a series of adaptation rules, is substituted for the pilot. These adjustment rules are based on an extensive backlog of human pilot response data obtained for many combinations of forcing functions and controlled element dynamics.* The degree of difficulty in achieving the predicted behavior and performance can be estimated from the parameters which the pilot must adopt to achieve both stability and satisfactory performance while remaining within his physiological constraints. The probability of maintaining the predicted performance for any reasonable time period is indicated by the allowable tolerances on pilot parameters consistent with stability. Finally, based on not yet fully developed correlations between the subjective pilot handling qualities opinions and ratings with the control parameters adopted by the pilot, a reasonable guess of the probable handling qualities characteristics of the manned booster can be made (Ref. 7).

The pilot's parameters are affected by four task variables — the forcing function characteristics, the display characteristics, the

---

*For a general review of mathematical pilot models and their use, see Refs. 7, 8, and 15. Reference 15 summarizes current rationale and mathematical model forms, and covers an extensive experimental program designed to validate and refine these models. References 9, 10, and 11 illustrate typical applications of these pilot models to piloted-vehicle problems.

controlled element dynamics, and the manipulator. Many other factors are implicitly involved. These include operator-centered variables such as training, fatigue, and motivation, and external environmental characteristics such as g-level, vibrations, illumination, and temperature. Ideally, all of these implicit and procedural variables should be taken into account, and someday perhaps they will. For the present the central aim is to exploit existing knowledge of the pilot's dynamics in a specialized, but realistic, simulation situation in which these variables are held constant.

For the booster control situation considered herein the displays (instruments) are compensatory. Therefore the dynamics of the controls, the vehicle and the display can be lumped into a "controlled element," and any forcing functions not appearing at the pilot's input modified via block diagram algebra into equivalent forcing functions and shifted to the input location. Thus, the manual control situation appears as shown in Fig. 3. The control loop signals are represented as time functions and/or Fourier transforms, or as power spectral densities. The controlled element is assumed to be reasonably well approximated by constant (average) coefficient differential equations at each of the three flight conditions of interest; it can be defined for control purposes by its linear transfer function, $Y_c(s)$. The nonlinear time-varying human pilot requires a <u>random</u> <u>input</u> <u>describing</u> <u>function</u>, Y_p (which depends on the forcing function, controlled element, manipulator, frequency, and time), plus a <u>remnant</u> (that portion of the pilot's output not described by the quasi-linear describing function) to provide an adequate dynamic description of his behavior.

B. THE RANDOM-INPUT DESCRIBING FUNCTION MODEL

The random-input describing function portion of the quasi-linear model for the human pilot comprises two elements:

1. A generalized describing function form

2. A series of "adjustment rules" which specify how to set the parameters in the generalized describing function so that it becomes an approximate model of human behavior for the particular situation of interest

The most extensive and generalized describing function form for one- and two-dimensional compensatory tasks developed in Ref. 15 is

$$Y_p = K_p K_T \left[\frac{a_T}{\sigma_T}\right] e^{-j\omega\tau} \left(\frac{T_L j\omega + 1}{T_I j\omega + 1}\right) \left\{\left(\frac{T_K j\omega + 1}{T_K' j\omega + 1}\right) \left[\frac{1}{(T_{N_1} j\omega + 1)\left[\left(\frac{j\omega}{\omega_N}\right)^2 + \frac{2\zeta_N}{\omega_N} j\omega + 1\right]}\right]\right\} \quad (1)$$

where

K_p = gain

τ = reaction time delay (transport lag)

$\dfrac{(T_L j\omega + 1)}{(T_I j\omega + 1)}$ = equalization characteristics

$K_T \left[\dfrac{a_T}{\sigma_T}\right]$ = indifference threshold describing function

$\doteq 1 - \left(\dfrac{2}{\pi} \dfrac{a_T}{\sigma_T}\right)$; when $\dfrac{a_T}{\sigma_T} \ll 1$

(a_T is the threshold value and σ_T is the rms input to the threshold characteristic)

$\dfrac{T_K j\omega + 1}{T_K' j\omega + 1} \dfrac{1}{\left[\left(\dfrac{j\omega}{\omega_N}\right)^2 + \dfrac{2\zeta_N j\omega}{\omega_N} + 1\right]\left(T_{N_1} j\omega + 1\right)}$

= neuromuscular system characteristic

The describing function is written in terms of the frequency operator, $j\omega$, instead of the Laplace transform operator, s, to emphasize that this

12

describing function is only valid in the frequency domain and under reasonably time-stationary conditions. For instance, it should not be used to compute the pilot's response to a discrete input. A detailed discussion of how the parameters of this complete model vary is beyond the scope of this report, and the reader is referred to Ref. 15 for an up-to-date presentation of the numerous factors involved. It is, however, necessary to discuss some of these here to the extent needed to justify the specialization of Eq. 1 to the much simpler approximate forms appropriate to the several types of booster control. Simplifications are possible because practical experience shows that it is not essential to use the complete form of the describing function model for every controlled element which is to be studied. The dominant stability and performance characteristics are determined by the characteristics of the operator-plus-controlled-element in the "crossover" frequency region of unity-amplitude-ratio (see Appendix A), so the characteristics at frequencies appreciably greater or less than this region may often be lumped into variables and the form of the describing function simplified accordingly.

The easiest quantity to eliminate in this case is the indifference threshold effect, represented in Eq. 1 by $K_T(a_T/\sigma_T)$. This is a factor which reduces gain for low amplitude inputs, to which the pilot may be indifferent without incurring serious performance degradation. Because the booster is unstable, indifference at almost any input amplitude level can lead to trouble, so K_T will be essentially unity for the direct manual control configuration.

The major elements of apparent complication in the complete model are those in the braces of Eq. 1. These terms arise from the neuro-muscular system, which is both input- and output-adaptive, i.e., its detailed characteristics depend on the system forcing function band-width and on the manipulator. Relative to crossover frequencies, the neuromuscular subsystem has both high- and low-frequency effects. The first terms, $(T_K j\omega + 1)/(T_K' j\omega + 1)$, are a lag/lead which creates a lagging phase angle and amplitude ratio rise at very low frequencies. This entire effect will be neglected for the booster control case because the time

constants, T_K and T_K', involved are of the same order as the trajectory time constants ignored in the vehicle dynamics. It is worth noting, however, that this neglect of the very low frequency phase will be optimistic, that is, if the phase lag were included in the pilot model, the stability limits of the pilot/booster combination, to be discussed subsequently, would be narrowed. Neglect of the amplitude ratio increase at low frequencies is conservative since it will turn out that this would generally improve the very low frequency closed-loop pilot/booster system response.

The high frequency portion of the neuromuscular system is the third-order system involving the parameters T_{N_1}, ω_N, and ζ_N. These are adjusted as a function of task demands in such a way as to decrease the high frequency phase lag, when such a decrease would be effective in improving closed-loop system characteristics. For manual vehicular control studies involving control of only rigid-body motions, it is almost always satisfactory to approximate the third-order characteristic by a first-order lag which gives an equivalent phase shift at the frequencies in the crossover region. For the booster control case, however, the presence of the flexible modes makes a higher order approximation necessary. In fact, the detailed analyses discussed in the next section will reveal that at least a second-order lag is needed to stabilize the bending modes. Consequently the quadratic portion of the third-order characteristic is retained in the simplest form when bending modes are important in the manual control problems.

The pure time delay represented by the $e^{-j\omega\tau}$ term is due to sensory excitation (the retina plus preliminary data processing in associated cells in the visual case), nerve conduction, computational lags, and other data processing activities in the central nervous system. It is a component of, and hence related to, certain kinds of classical reaction times. It is, of course, necessary to retain this time delay in the pilot describing function for booster control. In fact, it will be increased somewhat over its nominal value of 0.1 sec to better approximate the high frequency neuromuscular characteristic. In essence the pure time delay τ is replaced by $\tau_e \doteq \tau + T_{N_1}$. By this accounting, the

14

phase lag in the neuromuscular system due to the first-order $(T_{N_1}j\omega + 1)$ is included in τ_e.

The equalizing parameters T_L, T_I, and K_p are the major elements in the adaptive capability of the human which allow him to control many differing dynamic devices. Their function is the modification of the stimulus signal to a suitable neuromuscular command which is properly scaled and phased for proper pilot/vehicle operation. The form of equalizer is adapted to compensate for the controlled element dynamics and the pilot's reaction time delay.

Following all of this discussion, the general describing function form of Eq. 1 can be specialized, for manned booster problems, to:

$$Y_p(j\omega) = K_p \left(\frac{T_L j\omega + 1}{T_I j\omega + 1} \right) \frac{e^{-j\omega\tau_e}}{\left[\left(\frac{j\omega}{\omega_N} \right)^2 + \frac{2\zeta_N}{\omega_N} j\omega + 1 \right]} \qquad (2)$$

Although subject to considerable variation with manipulator characteristics, neuromuscular tension, etc., available fixed-base measurements (Ref. 15) indicate that the neuromuscular characteristics for this particular problem can be satisfactorily approximated with:

$$\omega_N \doteq 10 \text{ rad/sec} \quad , \quad \zeta_N \doteq 1.0$$

The effective delay time, τ_e, will range from approximately 0.2 sec for single-axis, full-attention situations to as much as 0.5 sec for multi-axis control. In this latter instance τ_e is the sum of the effective sampling delays as well as the neural velocity and residual neuromuscular delays.

The only terms in Eq. 2 remaining unspecified are the equalizing elements and the gain. These are adjusted as functions of the controlled element dynamics and forcing function to conform with the empirically based adjustment rules. The latest version of these is developed in Ref. 15 and discussed there in detail. For present purposes not all are needed, and a brief summary of the rules is given below.

15

1. Equalization Form Selection

The form selected for the equalizer, $(T_L j\omega + 1)/(T_I j\omega + 1)$, is such that:

    a. The system can be stabilized by proper selection of gain, preferably over a very broad region.

    b. $|Y_p Y_c|$ tends toward a -20 dB/decade slope in the crossover region (the crossover region is that frequency band centered on the crossover frequency, ω_c).

    c. $|Y_p Y_c| \gg 1$ at low frequencies, to provide good low frequency closed-loop response, i.e., good following, to system forcing functions, and suppression of disturbances.

2. Parameter Adjustment

After adaptation of the equalizing form, the describing function parameters are adjusted so that:

    a. Closed-loop low-frequency performance in operating on the forcing function is optimum in some sense analogous to that of minimum mean-squared error.

    b. System phase margin, φ_M, is directly proportional to forcing function bandwidth, ω_i, for values of ω_i less than about 2.0 rad/sec. For very low forcing function bandwidth, $\varphi_M \to 0$.

    c. Equalization time constants T_L or T_I, when form selection requires $1/T_L$ or $1/T_I \ll \omega_c$, will be adjusted such that low frequency response will be essentially insensitive to slight changes in T_L or T_I.

3. ω_c Invariance Properties

    a. $\omega_c - K_c$ independence. After initial adjustment, changes in controlled element gain, K_c, are offset by changes in pilot gain, K_p; i.e., system crossover frequency, ω_c, is invariant with K_c.

    b. $\omega_c - \omega_i$ independence. System crossover frequency depends only slightly on forcing function bandwidth for $\omega_i < 0.8 \, \omega_{c_0}$ (ω_{c_0} is that value of ω_c adopted for $\omega_i \ll \omega_c$).

    c. ω_c regression. When ω_i nears or becomes greater than $0.8 \, \omega_{c_0}$, the crossover frequency regresses to values much lower than ω_{c_0}.

A summary statement about the adjustment rules which is often helpful to engineers skilled in controls analysis is: The pilot describing function adapted for a given task is very similar to the one that a control engineer would select if he were given an element to control to specific criteria, together with a controller "black box" which contains elements mechanizing Eq. 2 and knobs for the adjustment of T_I, T_L, and K_p.

SECTION IV

PILOT REMNANT

A. SOURCES

Remnant is defined as the portion of the pilot's control output power which is not linearly correlated with the system input. Recent measurements (Ref. 15) have shown that, for run lengths comparable to the time required to define the operator's describing function over a broad frequency band, the remnant signals have a continuous and reasonably smooth spectrum. During closed-loop operation the total pilot's control output spectrum is defined as the sum of two linearly uncorrelated spectra:

$$\Phi_{cc}(\omega) = \Phi_{cc_i}(\omega) + \Phi_{cc_n}(\omega)$$

$$= |H|^2 \, \Phi_{ii}(\omega) + \Phi_{cc_n}(\omega) \qquad (3)$$

$$\uparrow \qquad\qquad \uparrow \qquad\qquad \uparrow$$

Total   Linearly   Remnant
correlated
with input

Here, H is the closed-loop describing function relating the command input and the pilot's control output for a particular set of task variables:

$$H = \frac{\Phi_{ic}}{\Phi_{ii}} = \frac{Y_p}{1 + Y_p Y_c} \qquad (4)$$

In Eq. 3, Φ_{cc_n} represents signals which have been passed around the loop, i.e., it is the closed-loop remnant. To ascribe this closed-loop spectrum of signals to processes internal to the pilot requires opening the loop and computing the signal properties which would have to be injected at the specified places to yield the total closed-loop spectrum.

18

In general, the sources of remnant are impossible to identify uniquely using only input/output measurements. As matters stand at present, one can only attempt to list and, by indirect measurement, to infer the dominant sources and most usable remnant models for a particular set of task variables. In ascending order of importance, the sources of remnant are considered to be due to:

Pure noise injection. There are numerous potential sources of "noise" along the sensing, equalizing, and actuating paths of the human pilot. These include component parts of the output position which are similar to the "range effect" (i.e., in a sequence of random amplitude steps, a tendency to undershoot the large and overshoot the small amplitudes), but on a continuous basis.

Nonlinear operations. Nonlinearities such as indifference thresholds, control output and rate saturation, or relay-like "sgn" functions produce harmonics of frequencies other than input frequencies, although their dominant (fundamental) effect is taken into account by the describing function. If the nonlinearities are large compared with the signal levels, involved, then appreciable remnant can result from this source (Ref. 16).

Nonsteady pilot behavior. The parameters of the pilot describing function can be defined meaningfully only as averages over certain lengths of time (Ref. 18). However, there is increasing evidence that significant time variations in the pilot's parameters occur during tracking, with variations in pilot gain and time delay as the prime offenders (Refs. 18, 19).

Clearly, the most appropriate way to treat remnant effects depends on the actual component sources present. When, however, mean-squared values of signals within the control loop are of central interest, the remnant can be satisfactorily represented by a signal having a specified power spectral density injected into the closed-loop system (see Fig. 3).

Considered as an injected signal, the point of application of the remnant can be moved from the pilot's output to other locations in the loop as long as the presumably small nonlinear elements are neglected in the process. Thus, properly shaped remnant may be considered to be injected at the pilot's output, input, or somewhere in between. Referring to Fig. 3

19

and denoting the injected remnant at e and c in the loop as Φ_{nn_e} and Φ_{nn_c}, respectively, the various remnant forms are related by

$$\Phi_{cc_n} = \left| \frac{1}{1 + Y_p Y_c} \right|^2 \Phi_{nn_c} \tag{6}$$

$$\Phi_{ee_n} = \left| \frac{Y_p}{1 + Y_p Y_c} \right|^2 \Phi_{nn_e} \tag{7}$$

B. DATA

Remnant data are far more sparse than describing function information, and the data available are not especially reliable. Reference 15 contains new data on the remnant which are not completely definitive but have resulted in considerable refinement to the above ideas. These findings show the following:*

- Careful examination of the output power spectral density indicated no evidence for periodic sampling or strongly nonlinear behavior. Nonperiodic sampling is not ruled out, however, for the run lengths considered (20 sec to 4 min).

- At low frequencies the remnant data for a wide variety of controlled elements coalesce best when all the remnant is injected at the pilot's input.

- Remnant increases with controlled element gain, with forcing function bandwidth, and with control order.

- Some evidence for asynchronous pulsing behavior in control of controlled elements requiring generation of lead is indicated by control amplitude distributions.

---

*To augment the data shown here, and supply some more recent STI remnant data, Appendix C has been included. However, these data were not available at the time the original analysis was performed.

Some typical open-loop remnant spectra referred to the pilot's input are given in Fig. 4. Included are a range of controlled elements of varying difficulty and requiring both no lead and full lead equalization by the pilot. (The scale is referenced to inches on the CRT error display.)

C. MODEL

Until more definitive and exhaustive data become available, two options are available for analyzing remnant effects in manual control systems. When the controlled element is identical to one for which data of the type shown are available, the actual data points can be used to perform a brute force numerical computation on a frequency-by-frequency basis. More often, a simple mathematical model which fits the essential features of the data is desired, so that analytical techniques can be employed.

The simplest model which seems appropriate to represent these remnant input data is white noise passed through a first-order filter. The break frequency and level are chosen to best fit the relevant data. The resulting remnant spectrum model is:

$$\Phi_{nn_e} = \left| \frac{2\sigma_n \sqrt{\omega_n}}{j\omega + \omega_n} \right|^2 \tag{8}$$

where ω_n is the remnant spectrum break frequency

   σ_n is the rms remnant, referred to the error display

A curve of this form is shown in Fig. 4 fitted by the parameters $\omega_n = 1.0$ rad/sec, $\sigma_n = 0.22$ in. (0.56 cm). This is the injected remnant model used for the analysis of manual booster control later in this report.

D. DESIGN TO MINIMIZE THE EFFECTS OF REMNANT

Means to alleviate effects of the remnant on the vehicle response
are important in the analytical design of manual control systems.
Fundamentally, there are two aspects to the consideration of remnant
effects. The first is the determination of the consequences of the
remnant on vehicle motions; and the second is the alleviation of these
consequences by proper tailoring of the controlled element. Only the
latter will be explored in this section, postponing examples of the first
until later.

The remnant data just given provide the basis for two simple design
concepts to minimize the effects of pilot remnant. These are:

    a. The use of stability augmentation techniques to
        modify the effective controlled element dynamics
        to a form requiring no low-frequency lead genera-
        tion. This implies that the controlled element
        characteristics should approximate K_c/s in the
        frequency region around the pilot/vehicle system
        crossover.

    b. The adjustment of the controlled element gain to
        its optimum value, after the controlled element
        form has been appropriately modified. This gain
        is most easily determined by a systematic experi-
        mental survey of gains using pilot ratings as the
        basic performance measure.

Besides the controlled element adjustments in the region of pilot/
vehicle system crossover, consideration can also be given to the use
of filtering to reduce the higher frequency remnant effects. This
is especially important on vehicles with flexible modes which may
be excited by the remnant and thereby degrade the manual control
performance.

To reduce flexible-mode excitation, two things are desirable. Sharp,
discrete control surface inputs having high-frequency content should be
reduced to the extent feasible, and the circulation of high-frequency
power should be reduced. If low-frequency lead generation is not re-
quired, the pilot's outputs are in general much smoother and the remnant

bandwidth, as well as its amplitude, is reduced — so the use of stability augmentation to provide a better controlled element is an example of the first remedy. The second form of suppression can be accomplished by filtering. Here, the goal is to provide the greatest possible smoothing without destabilizing or increasing the effective order of the controlled element in the crossover region. These two factors inevitably require a tradeoff. This tradeoff possibility is unique to manual control systems, since automatic controllers do not incur additional significant remnant penalties from lead equalization.

SECTION V

FULLY MANUAL CONTROL

A. BASIC ANALYSIS

To analyze the dynamics of the fully manual control mode, the adaptive pilot model of Eq. 2 is combined with the servo and booster transfer functions in Table III (resulting from the equations of Table I and the data of Table II) to determine the open- and closed-loop characteristics of the pilot-plus-booster combination. There are two different steps involved in the analysis of the resulting man/machine feedback system. The first is unique to systems involving human components: the estimation of the forms and parameter values for the pilot's equalization. The second step is the same for manual or automatic systems: the estimation of closed-loop characteristics. Because the pilot's equalization form is limited, and the parameter adjustments are similar to those selected by a controls engineer for an automatic system incorporating a similar equalizer, the theoretical distinctions raised above are of no practical consequence. Instead the two steps of the analysis are combined into an "iterative synthesis" process. "System surveys" are made to select the best tradeoff among the various pilot and adjustable system parameters over the range of operating conditions involved. This process requires both experience and good judgment in servo analysis, combined with a set of versatile and rapid systems analysis techniques. One such set of analysis tools has been developed over the past several years by STI and has been termed Unified Servo Analysis Method—USAM, for short (Refs. 20-22). To avoid unduly complicating the text at this point with a resume of these techniques, Appendix A has been prepared for the unfamiliar reader. There, these techniques are briefly explained and a complete system survey applied to the booster used in this study is presented to show the interrelationships among the various graphical plots involved. The reader who is not familiar with this approach to the analysis of servo systems should review Appendix A, because at least a passing acquaintance with its content is necessary in the work to follow.

With the form of the pilot response model in mind, system surveys of the attitude control loop were made at each flight condition, using the USAM methods (see Figs. 5 and 6). The results of the surveys at each of the three design conditions (see Table III) reveal the following information about the basic _attitude_ loop closure:

1. The booster alone is dynamically unstable at the lift-off condition, statically unstable at the design condition (high dynamic presssure), and almost neutrally stable at the burnout condition (see Table III).

2. The use of pure gain attitude feedback is not sufficient to stabilize the rigid-body modes. For example, the φ_{RG}/β_c Bode plot of Fig. 5 nowhere exhibits a frequency region with positive phase margin.

3. To stabilize the rigid-body modes at all three conditions, appreciable rate feedback is required to establish a region of positive phase margin. If pure lead equalization is used (e.g., via display of attitude rate) the low-frequency amplitude ratio will be very small relative to unity, and the attitude tracking accuracy criterion cannot be met. Consequently, a combination of feedbacks amounting to lead equalization of rigid-body attitude is required. Typical desirable values for the lead time constant, T_L, are 1.5 sec or larger (see Fig. 6).

4. With only the above lead equalization, the rigid-body modes are stabilized, while the bending modes are destabilized. To avoid this, additional lag equalization comprising at least a second-order filter is needed to provide proper phasing at bending frequencies. Figure 6 shows that this can be accomplished with a second-order lag with a time constant of 0.1 sec.

5. Examination of the effective attitude dynamics for the two possible sensor locations at all three flight conditions showed that only the present rate gyro location would permit fixed equalization throughout first-stage flight, presuming that only one instrument location is considered. (A mixture of signals from the two locations was not investigated.)

6. An attitude gain reduction at a point near t = 100 sec is necessary to provide the high gain needed during the early stages of flight while avoiding destabilization of the system near burnout.

7. Due to the extremely low lifting effectiveness of the booster relative to its mass, the amplitude ratio of the

open-loop system is essentially flat out to the short-period frequency region. To insure stability, gain cross-over must occur just beyond this region. The low-frequency open-loop amplitude ratio will only be somewhat-greater-than-1 instead of the much-greater-than-1 needed for "good" low-frequency response. This implies that good attitude tracking performance will be impossible to achieve without some form of low-frequency lag or lag/lead equalization. This problem will manifest itself to the pilot as poor trim control (Ref. 23).

The desired equalization indicated by the above considerations consists of a low-frequency lead and a relatively high-frequency second-order lag. The generalized describing function form of Eq. 2 is therefore specialized to contain only these terms, the effective time delay, τ_e, and the gain chosen to insure stability. With the exception of the additional low-frequency lag/lead equalization necessary to achieve good attitude tracking performance, a comparison of the minimum equalization with the generalized describing function form of the human pilot given in Eq. 2 indicates that the pilot can adopt the necessary equalization.

The second-order approximation to the nonadjustable neuromuscular characteristics used in Eq. 2 is a most appropriate lag equalization for phase and/or gain stabilization of the bending modes just as is (i.e., $\omega_N \doteq 10$, $\zeta_N \doteq 1$). A similar statement can be made about a higher-order (third-order system) approximation to the neuromuscular system, so this estimate is not sensitive to the slight simplification made. (As already noted, any lower-order approximation for the neuromuscular system is not suitable.)

The basic adjustment required of the pilot is the provision of a substantial amount of lead equalization. A minimum value for T_L of about 2 sec is needed to satisfy the dual requirements (based on the adjustment rules) of providing reasonable gain margins and low sensitivity of the closed-loop dominant modes to T_L. The sensitivity would be, in fact, somewhat better if T_L were made even larger than 2 sec, so this value should be considered the lower limit. This value of lead is well within the pilot's capabilities for single-axis control. An implicit requirement here is that the attitude display be suitable for the ready extraction of rate information by the pilot.

As noted in item 7 above, additional lag/lead equalization would improve the low-frequency response to attitude commands from the guidance system. However, most of the pilot's low-frequency lead equalization capacity is already in use, so it is very unlikely that the pilot will also provide the additional low-frequency lag/lead equalization required for good trim control. Because of the rather tight gain margins and relatively low phase margins, it is also unlikely that the pilot will have sufficient scanning reserve left to control another axis, unless an integrated display is used.

Finally, sensitivity analyses of the type described in Appendix A were performed for variations of some of the booster dynamic parameters. These show that the pilot equalization characteristics selected are in a fairly insensitive region, i.e., changing pilot characteristics (other than gain) somewhat will not have an extremely large effect on the closed-loop dynamics. The gain, of course, is an exception and must be confined within fairly narrow bounds.

In summary, the estimated describing function typifying pilot behavior during fully manual control of this booster can be approximated by

$$Y_p = \frac{K_p e^{-0.2j\omega}(2j\omega + 1)}{\left[\left(\frac{j\omega}{10}\right)^2 + \frac{2(1.0)j\omega}{10} + 1\right]} \tag{8}$$

The resulting attitude-loop dynamics are given for each flight condition in Table IV-A and are shown in Fig. 6 for t = 77 sec. This system survey shows that:

1. The pilot can close the loop at a unity gain crossover frequency of $\omega_c \doteq 1.0$ rad/sec with small but adequate gain and phase margins.

2. $|Y_{OL}|$ is not very much greater than unity at the low frequencies characteristic of the guidance input and the system will have poor tracking performance.

3. The bending modes can be phase-stabilized by the combined neuromuscular and reaction time lags.

The foregoing describing function estimate, predicated on the application of the adjustment rules, can be supplemented in this case by specifically

27

applicable human pilot data (Ref. 15). Of these, the form tested which is closest to the booster problem was

$$Y_c = \frac{K_c}{s(s - 1/T)} \qquad (9)$$

The quantity $1/T$ represents the time constant of a second-order divergent controlled element and may be considered similar to the inverse time constant of the static divergence of the booster near the design (maximum-q) condition. The value for the booster divergence is $1/T \doteq 0.3$ to 0.4 rad/sec. The human response data for the similar $K_c/s(s-1/T)$ case, with $1/T = 1.0$ rad/sec, is shown in Fig. 7 along with curves for the describing function estimated above. It can be seen that the behavior and parameters predicted for the booster pilot are within the capabilities of the human operator as observed in these experiments, and that the form of the operator's describing function is reasonably consistent with experimental data for a similar control task. The major difference between the actual data and the estimate of Eq. 8 is in the additional very-low-frequency phase lags exhibited by the experimental data. These are due to the low-frequency neuromuscular lag/lead term shown in Eq. 1 and neglected in the approximate model of Eq. 2. The lag/lead is an adaptive term (Ref. 15), and the amount of low-frequency phase lag shown here is somewhat more than should be anticipated with the booster control system. However, it is likely that the relatively small maximum phase margin indicated in Fig. 6 will be further reduced in practice by this very-low-frequency effect.

B. HANDLING QUALITIES

Attention can now be turned to the handling qualities of this task. Two aspects are important—a summary of likely pilot comments and an estimate of pilot ratings. The first of these is accomplished by reviewing all the features of the loop closure of Fig. 6, most of which have been discussed above in technical terms, and then translating these into phrased subjective statements in pilot language. This is a difficult and somewhat artistic enterprise, but some insight into the process may

be obtained from Table V, which reviews the loop closure control characteristics and gives some of the pilot opinions which would be expected as subjective impressions of these characteristics.

The pilot ratings depend on many factors, the most objective of which are the controlled element, the parameters the pilot must adopt, the degree of stationarity he must maintain in his characteristics, etc. Some correlations relating these characteristics and pilot rating exist (e.g., Ref. 7, Refs. 23-28, plus unpublished STI data) and rough estimates are possible. Again, some experience and judgment are required. A Cooper rating of 8 ("unacceptable;" see the previous discussion in Section II) was obtained during the experiments leading to the pilot describing function data shown in Fig. 7 (unpublished data). But the task there was in the context of long-time control of an aircraft with a short-period instability. For the short-time (at high dynamic pressure) control of the booster at high dynamic pressure, and as a backup mode only, the rating will undoubtedly be somewhat better. In no case would it be as high as the rating of about 4 associated with the best obtainable when low-frequency lead must be generated, because of the tight gain margin. Taking such factors as these into account, the estimated Cooper ratings for the fully manual control mode should range from unsatisfactory to unacceptable (5 through 8) even if only one axis is under control.

C. MULTIAXIS CONTROL

The feasibility of fully manual control of more than one axis will depend greatly on the type of display arrangement. When the requisite guidance and control information must be obtained from the scanning of separate displays, the effective time delay in the pilot's describing functions for each axis is increased. Considering the extreme equalization required for single-axis fully manual control and the, at best, marginal stability, there is little margin in effective time delay allowed for the scanning of separate displays. Consequently, it will be extremely difficult, if not impossible, for the booster pilot to perform the full mission with fully manual control in the presence of any significant disturbances, wind spikes, or off-nominal conditions.

The rigid-body dynamics and the thrust vector control moments are roughly the same in the pitch and yaw degrees of freedom, so it should be possible to integrate the displays of these two axes. The error signal would then appear as the tip of a vector and the control action would be directly opposite to this vector error. The experience of a number of investigators with such combined displays (e.g., Refs. 27-30) implies that the effective dimensionality is reduced, and that performance roughly equivalent to that for a one-dimensional display results. Therefore, it is predicted that the pilot probably could handle two axes in the fully manual control mode, provided that an integrated error display exists, the commands and wind disturbances are predominantly along one pitch axis, and the control stick gains are equal in each axis.

Control of the roll axis is not considered a severe problem by itself, but would be extremely difficult if fully manual control were required about the other two axes simultaneously. Piloted control of the roll axis was not within the scope of this study.

D. SUMMARY OF PREDICTIONS FOR FULLY MANUAL CONTROL

The foregoing analyses of the fully manual control mode (minimal flight control system) lead to the following main predictions for this pilot role:

1. Fully manual control about one booster axis is feasible.

2. To accomplish this control the pilot must generate low-frequency lead (to create a region of conditionally stable operation) and high-frequency lag (to gain and phase-stabilize the first two bending modes).

3. Extreme pilot attention is required to the basic stabilization task, and even then the pilot will be near his limits of control. Therefore, the handling qualities will be very poor and there will be little delay time margin available for monitoring other instruments.

4. The accuracy in tracking pitch guidance commands will be poor. To the pilot this will appear as difficulty in trimming the booster and frequent exceedance of the guidance tolerances.

30

5. If pitch and yaw axes are combined on an integrated display, and if the pilot is provided with an integrated controller, then simultaneous fully manual control of two axes should be possible.

6. The pilot should not try to "chase" any bending modes discernible on his display, but should let his normal neuromuscular lags filter them out, i.e., adopt a "smooth" control technique.

These predictions are tentative in that they do not reflect the effects of pilot remnant.

SECTION VI

AUGMENTED MANUAL ATTITUDE CONTROL

A. DESIGN PRINCIPLES

To illustrate the analytical synthesis of a "good" manual control system at the preliminary design stage, this section will review the design of an augmented-manual system for the booster. The pilot is fully in the loop with a compensatory display of guidance attitude deviations, but the stability and handling qualities of the booster vehicle are augmented with an automatic flight control system to provide an "effective" controlled element* with "good" dynamics.

Just what features are necessary and sufficient to constitute "good" controlled element dynamics are not too well defined. However, several sufficient features are known, and these will serve as a starting point. Most generally, "good" controlled element dynamics are those which the pilot can easily and comfortably control to any desired level of precision within a wide range. Such dynamics are rewarded with good pilot ratings. Previous work (Refs. 7, 31) has indicated that the best handling qualities ratings are achieved when the pilot is not required to develop low-frequency lead equalization, i.e., when he acts (on the average) as a pure gain element (or a low-frequency lag element) plus a time delay. The time delay is composed of his basic transport lag and additional components to approximate any higher frequency neuromuscular lags, sampling of the various displays, etc. For unattended operation, the effective controlled element should possess at least neutral static stability, that is, no roots in the right-half plane and no more than one root at the origin. Although definitive experimental results are still lacking, available data (Refs. 7, 26, 32, and unpublished STI data) indicate that a prerequisite to obtain Cooper ratings of 3 or better in tracking tasks is a controlled element form which

---

*The effective controlled element here comprises the dynamics from the pilot's control stick (manipulator) output all the way around the loop to the displayed error.

32

in the region of pilot/vehicle system crossover has a smoothly varying amplitude ratio characteristic lying somewhere between $Y_c = K_c$ and $Y_c = K_c/s$. Forms which approximate $Y_c = K_c/s^2$ in the crossover region tend to have a minimum rating of 4 or worse. It will also be recalled that controlled element dynamics which approximate K_c/s are also desirable to reduce the remnant (K_c must also be adjusted to an optimum value). This is especially important as a means to reduce pilot excitation of bending modes.

Besides good handling qualities there are other system features which must be provided for a good pilot/vehicle system. These, and the handling qualities based considerations, are summarized below.

1. Effective vehicle dynamics having $Y_c \doteq K_c/s$ in the desired region of crossover (for good handling qualities and minimum remnant); and at least neutral static stability (for unattended operation).

2. Large $|Y_{OL}|$ at very low frequencies to improve the guidance tracking accuracy.

3. Filtering to reduce the vibrations induced by the pilot's remnant.

4. Compatibility with the load relief mode of operation (to be discussed in the next chapter).

5. Good mechanizational design qualities, such as simplicity, insensitivity, etc.

Bear in mind that the final augmented attitude control system was evolved in conjunction with the load relief system (see Section VII). The attitude control system was given first priority, however, because the load relief mode is only used near the time of passage through the atmospheric jet stream. The distribution of equalizations, filters, and gains in various parts of the loop did depend on consideration of all of the factors listed above, and not just the attitude loop alone.

B. SYSTEM SYNTHESIS

First the form of the attitude equalization is derived from the basic system requirements and then the specific values will be found by iterative servo analysis techniques.

As noted in Section V the rigid-body short-period mode is statically unstable and about neutrally damped, so pitch rate feedback is essential for positive damping. Pitch attitude feedback is desirable to increase the static stability for stable unattended operation. Three schemes can be used to obtain the desired lead time constant, T_L, of the controller:

Lead equalization schemes:

1. Weighted sum of present attitude and rate gyro feedbacks:

$$\beta_F = K_d \varphi_{AG} + K_r \dot{\varphi}_{RG} \quad ; \quad T_L = \frac{K_r}{K_d}$$

2. Lead (network) equalization on the present attitude gyro output:

$$\beta_F = K_d(1 + T_L s)\varphi_{AG}$$

3. Parallel integration on the present rate gyro output:

$$\beta_F = \left(K_r + \frac{K_d}{s}\right)\dot{\varphi}_{RG}$$

$$= K_d(1 + T_L s) \frac{\dot{\varphi}_{RG}}{s} \quad ; \quad T_L = \frac{K_r}{K_d}$$

Although each of the above schemes gives the same increase in rigid-body mode stability, there are significant differences in their bending mode interactions, because the attitude and rate gyros are at different body stations and pick up different bending mode slopes.

A first cut at the lead time constant for satisfactory rigid-body dynamics has already been established as a by-product of the fully manual backup mode analysis; this value was $T_L \doteq 2.0$ sec ($1/T_L = 0.5$ sec^{-1}). As a general rule of thumb, it is desirable to put the lead break frequency just at or beyond the short-period mode, so as to obtain the majority of phase advance at frequencies somewhat higher than the short-period break, while not flattening the amplitude-frequency slope below about —20 dB/decade in the region of desired gain crossover. In this case, a lead break point of $1/T_L = 0.5$ sec^{-1} is a compromise value; perhaps a little low for T = 77 sec,

34

but somewhat high for the launch and burnout conditions. Anywhere in the region of $1/T_L = 0.5$ to 1.0 sec^{-1} is good from the standpoint of insensitivity of the closed-loop bending modes, because they are at a much higher frequency and "see" nearly the full phase lead when $1/T_L$ is in this range.

Bending modes are usually stabilized with either notch or low pass filters. In this case the system surveys showed that low pass, second-order lags would be preferable to notch filters because they (1) attenuate both the bending modes and system internal noise, and (2) increase the damping of the bending modes if the sensors are properly located (so-called phase stabilization). The phase stabilization of the bending modes is critically dependent on the relative location of the poles and zeros in the s-plane. Expressed in terms of the frequency domain, phase stabilization depends on the achievement of a "sawtooth" Bode plot with the proper order of successive poles and zeros. Appendix B contains a brief description of the sawtooth Bode concept. Boiled down to its simplest implications for the case at hand, the sawtooth Bode concept insures that the closed-loop roots will depart in a generally stabilizing direction from their open-loop starting points. For further discussion see Ref. 33.

As shown in Fig. 1, the attitude and rate gyros are not located at the same points on the Saturn V booster. Since the location of bending mode zeros is dependent on the weighted sums of the mode shape slopes at various locations, it is often possible to achieve a desired sawtooth Bode configuration by a proper choice of gyro location or by summing or "blending" the outputs from two gyro locations. In the case at hand, detailed system surveys using the Unified Servo Analysis Methods showed that the attitude gyro location (scheme 2) satisfied the sawtooth Bode criterion at the maximum-q condition but not at the other flight conditions, whereas the rate gyro location (scheme 3) satisfied the sawtooth Bode criterion at all three flight conditions. Thus the desired equalization is simply obtained as the sum of the $\dot{\varphi}_{RG}$ signal plus a constant times its integral (achieved either with an integrator or with a first-order lag having a very long time constant). The mixture of scheme 1 was not considered in detail for reasons of analytical simplicity, although the analysis technique of Ref. 22 can readily handle such multiloop problems.

A summary of the possibilities considered in evolving the final stability augmenter loop is given in Table VI, while a typical system survey for the augmenter loop closure is shown in Fig. 8. The detailed equalization gains and resulting closed inner loop transfer functions are tabulated in Tables III-B-2 and IV-B.

Besides proving the effectiveness of the equalization picked on a preliminary basis, the detailed analyses also showed that a reduction in gain between the maximum-q and burnout conditions was necessary if good augmentation loop characteristics were to be obtained. However, with this gain shift as nominal, the gain margin was fairly insensitive to changes in lead equalization. The surveys also indicated that it is not necessary to mechanize the second-order bending filters very precisely. For instance, a pair of real roots at 4.0 and 6.0, or a quadratic pair of roots having a natural frequency of 5 rad/sec and a damping ratio anywhere from 0.8 to 1.0, would be acceptable. Consequently, the design is fairly insensitive to system parameter changes other than gain.

The final equalization for the stability augmenter loop is as follows:

$$\frac{\beta_c}{\dot{\phi}_{RG}} = \frac{25\,K_r(s + 0.5)}{s(s + 5)^2} \tag{10}$$

with $K_r = -1.26$ for $0 < t < 100$ sec

decreasing to $K_r = -0.29$ for $105 < t < 150$ sec

Close inspection of the Bode plot in Fig. 8 at low frequencies shows that the open-loop amplitude ratio at low frequencies is not very large (approximately 12 dB, or 4:1), so the closed-loop following of attitude commands (ϕ_c) would be poor. Based on the fundamental feedback equation of error/input $= 1/(1 + |Y_{OL}|) = 1/(1 + 4)$, the error would be about 20 percent of the command input. To provide more accurate guidance, the closed augmenter loop should be preceded by a prefilter having properties approximating an integrator in the frequency range from 0.02 to 0.10 rad/sec, which brackets the time variation of the main gravity turn commands (e.g., Fig. 2).

At this stage in the investigation the pitch attitude equalization comprising display, pilot, and manipulator dynamics was considered as one block in the forward loop of a simple unity feedback system, as in the block diagram of Appendix A. This form is similar to what might be synthesized for an automatic pilot system having a transfer function form and adjustments similar to the pilot's describing function plus display and manipulator dynamics. Remnant calculations had not yet been made, so the rearrangement of elements (as in Fig. 8) to provide post-pilot-filtering of remnant effects (while still retaining identical total open-loop pilot/ vehicle system describing function characteristics) was not considered in detail at this juncture. However, the possibility of remnant-induced bending vibrations was recognized, and the likely requirement for stick motion filter was indicated. The load-relief controls were then investigated separately as described in the next main section of this report. These independent mechanizations were termed the "Phase I systems." The next phase included the pilot/vehicle integration, during which required compromises between the attitude and load-relief loop mechanizations were considered. At this point, some preliminary results from a concurrent Ames Research Laboratory simulation program (both fixed- and moving-base) were made available (Ref. 34). These results showed an encouraging degree of similarity in the control problems and solutions uncovered by the analytic and simulation studies. They also emphasized the extreme importance of filtering inadvertent pilot control action (remnant) and the feasibility of the pilot switching between manual attitude and load-relief control modes by merely shifting his attention to one or the other display. Thus, the availability of supporting simulation data made the system integration phase much more efficient.

C. OPTIMUM CONFIGURATION OF EQUALIZATION ELEMENTS

Before considering the distribution of the equalization elements in the forward or feedback portions of the augmentation loop, the pilot's stick shaping filter should be discussed since it is the combined inner and outer loops which must be optimized. A series of USAM surveys was performed for various combinations of pilot shaping filter and forward and feedback loop equalization. If all of the augmenter loop equalization is put into the forward portion of its loop, a more complex pilot shaping filter is required than if some of the equalization is allowed to remain in the feedback loop.

37

Other considerations such as the ease of summing signals, systems integration with load-relief operation, and the desirable location of the bending mode filters in the engine servo amplifier package (for maintenance and checkout convenience) resulted in splitting the augmentation loop into two parts, with the low-frequency equalization in the feedback loop and the bending mode filter in the forward portion of the loop as shown in Fig. 8.

The main factors determining the outer (guidance) loop equalization were:

- Use of the existing high-precision, precessed-command attitude gyro for the basic outer loop error feedback;

- High open-loop amplitude ratios at frequencies below approximately 0.1 rad/sec, the frequency range of the basic guidance commands;

- K/s-like response near crossover frequencies for good handling qualities;

- Strongly attenuated pilot outputs at high frequencies to suppress the pilot's inadvertent control outputs at bending mode frequencies.

It was found possible to satisfy the performance, handling qualities, and the remnant suppression criteria by the use of a simple stick output filter approximating a pure integrator in the frequency range from 0.02 to 10.0 rad/sec. The open-loop controlled element as seen by the pilot is shown as the dotted line in Fig. 9. It can be seen that the controlled element approximates K/s over a wide frequency range. With the preferred nonequalized pilot model, crossover can be achieved at frequencies from 0.4 to 0.8 rad/sec, depending on the value assumed for the pilot's effective time delay. Experience has shown that pilot delay time of about 0.5 sec corresponds to a fair allowance for scanning other instruments and axes of control. With this value, the resulting pilot/vehicle open-loop response is shown as a solid line in Fig. 9, and the resulting closed-loop guidance loop response is shown as a dashed line. The closed-loop tracking accuracy is very good for frequencies up to about 0.3 rad/sec and the bandwidth (to the -3 dB point) is about 0.5 rad/sec.

D. HANDLING QUALITIES

The handling qualities of the augmented vehicle should be appreciably better than those for the direct manual mode case. If the controlled element (φ_D/δ) approximated K_c/s without any additional phase lags, then we would expect the Cooper ratings to be near-optimum, i.e., in the range from 1 to 3. However, the additional lags apparent in Fig. 9 tend to bias the estimated ratings toward the higher values. Still, the ratings obtained should be better than those expected for $Y_c = K_c/s^2$, which experience has shown to range from roughly 4 to 6. From the standpoint of good tracking accuracy and minimization of internal system disturbances (especially remnant rejection, which will be discussed later), this augmenter system vehicle should be very superior to the fully manual mode.

E. SENSITIVITY TO FLIGHT CONDITIONS

Calculations of the inner and outer attitude loop roots were made at all three design conditions (t = 0, 77, 150 sec). Tables IV-B and IV-C show that the selected equalization stabilizes all modes at all conditions (except for a very small divergent real root near burnout with a 2000 sec time constant). The inner loop gain should be reduced by roughly a factor of four somewhere between t = 77 and 150 sec (say, t $\doteq$ 100 sec). This gain reduction should be smoothly accomplished over a 5 sec period so as not to produce large transients in the system.

The validity of selecting the rate gyro location for attitude pickup is proven by the improved damping of the bending modes at all conditions. While fixed equalization may not always be feasible when slosh and still higher bending modes are considered, it does appear quite satisfactory in this case.

One caution is in order at this point. Examination of the root locus plots near the $j\omega$-axis at $j\omega \doteq 7$ rad/sec shows that the first bending mode depends strongly on the bending filter phase lag for its increased damping (see Fig. 8), and that this mode has no zeros nearby to help absorb its detection by the attitude gyro (see Fig. 9). Any loss or cancellation of

39

this phase lag may easily give zero (or even slightly negative) damping, and hence a very high peak on the Bode plot.

There are several other aspects of systems integration which normally would be investigated, but were not included in the scope of this analytical study. Typical items are loop signal dynamic range (adverse when differencing one integrator output with another, as in the inner loop); failure of various feedbacks (safe for outer loop opening, dangerous for inner loop opening in the proposed system); and compatibility with hands-off flight during other distractions (safe, here). These problems can be efficiently checked by using USAM techniques in close cooperation with a simulation program.

SECTION VII

LOAD RELIEF

A. BASIC CONCEPTS

The worst structural loading conditions for most large boosters occur at altitudes near the stratosphere, where jet stream "wind spikes" cause a sudden build-up and drop-off of the apparent wind angle of attack over a period of several seconds. Large liquid-fueled boosters happen to accelerate so slowly that the maximum dynamic pressure is reached at about the same altitude at the jet stream. A booster 100 meters long is nearly the size of a naval destroyer, so it cannot be pointed rapidly into the wind. Furthermore, at this time most boosters are aerodynamically unstable, mainly because the aerodynamic loads occur on expanding sections of the booster which are concentrated near the nose. The design structural bending loads are thus due to a formidable combination of large crosswind pulses, sluggish vehicle response, maximum-q conditions, and destabilizing lift forces near the nose.

This problem has been attacked from many angles, including improved representations for wind measurement and prediction (Ref. 35), increasingly detailed methods for analyzing the vehicle loads and response (Ref. 36), and load alleviation flight control systems (Refs. 37-39). A careful survey of this and similar material revealed that, at least for the preliminary design stages being considered here, a few basic facts underlie all the detailed results. These concepts are discussed in the next few paragraphs.

The critical structural loads nearly always result from the gross features of the wind profile: the obvious peaks, large shears, shear reversals, and any low-frequency periodic components. The fine structure of the wind may excite certain elastic modes, but it seldom adds more than a few percent to the structural loading ("gross" $\gg$ 10 booster lengths; "fine" < 10 lengths)(e.g., see Ref. 36, 40).

41

Load relief control can be accomplished in two ways:

1. Point the vehicle away from the wind and drift with it.

2. Point the vehicle into the wind (weathervane) to reduce the net angle of attack toward zero.

Drifting with the wind, which amounts to augmenting the effective lift curve slope, has the advantage that the programmed vertical pitch attitude can be ultimately regained, at the expense of both a large increase in trajectory displacement and a long time to achieve the desired wind velocity. Meanwhile, the angle of attack (and the loads) remains high. This scheme is feasible only for very low-frequency, quasi-steady changes, and not suitable for alleviating jet-stream wind spikes. Pointing into the wind, which is equivalent to augmenting the aerodynamic weathercock stability, can be made rapid enough to cope with wind spikes, but has other drawbacks. Pointing an accelerating rocket into the local relative wind results in a path mode which diverges asymptotically to horizontal flight toward the source of wind. This gravity-induced effect shows up in the linearized perturbation dynamics as an unstable root having a long time constant given by: $T_1 \doteq V/g'$, where $g' = (T - D - W)/M$. Consequently, load relief control cannot be maintained for any length of time beyond the high-crosswind period.

B. WIND SPIKE SPECTRUM

It is useful to convert the time-history of a given wind spike to a frequency-domain specification by taking its Fourier transform and plotting this as a disturbance input "spectrum." The resulting curve is the envelope of the set of Fourier line spectra of the discrete input, and so the dominant bandwidth and significant frequencies of the input are revealed. (See Ref. 41, p. 365ff., for a more complete discussion of this concept.) Figure 10 shows the Fourier envelope for the typical wind spike specified in Fig. 2b, from which it is apparent that the dominant frequency content of the wind spike is below about 0.2 rad/sec. To weathercock the booster into this wind spike, the response of the closed-loop load relief control system must have a bandwidth of at least 0.2 rad/sec and should have some response out to 0.5 rad/sec.

C. CONSTANT PITCH ATTITUDE CONTROL, $\varphi = 0$

Before proceeding with the load-relief system, it is helpful to examine the basic causes and severity of the gust load problem. The simplest way to estimate the potential severity of the structural load due to a wind spike is to consider the case when the vehicle penetrates the wind spike with its thrust vector moved so as to always maintain the pitch attitude and its derivatives identically zero; an ideally rigid pitch control. Because the booster is unstable, an actual attitude system (which will have an error away from the wind) will always be worse than this ideal case.

With $\ddot{\varphi} = \dot{\varphi} = \varphi = 0$, the equations of motion for the rigid-body degrees of freedom reduce to the following set:*

$$\ddot{x} - F_\alpha \alpha = F_\beta \beta$$

$$\frac{57.3}{V} \dot{x} + \alpha = + \alpha_w$$

$$M_\alpha \alpha = M_\beta \beta$$

$$\frac{-q}{11 \; q_{max}} \alpha + \mu = 0.2\beta$$

(11)

The transfer function relating the booster angle of attack, α, to the wind input, α_w, is then simply:

$$\frac{\alpha}{\alpha_w} = \frac{s}{(s + 1/T_2)} = \frac{T_2 s}{(T_2 s + 1)}$$

(12)

where:

$$\frac{1}{T_2} = \frac{57.3}{V} (F_\alpha + F_\beta \frac{M_\alpha}{M_\beta})$$

(13)

Lift force   Thrust vector force

---

*Other more detailed calculations showed that the elastic mode contributions to μ were negligible for the ideal $\varphi = 0$ case.

43

At t = 77 sec, the data of Table II give:

$$\frac{1}{T_2} = \frac{57.3}{486}\left[0.13 + \frac{(0.3)(0.14)}{1.15}\right]$$

(14)

$$= 0.018 \text{ sec}^{-1}$$

Since the vehicle is free only to drift, but not to pitch, the inverse time constant of the response is dominated by the very low lift-curve effectiveness of the vehicle; $1/T_2 \doteq 57.3\, F_\alpha/V$, as can be seen above. The above results imply that for a step crosswind input, the booster drift will reach about 85 percent of the crosswind velocity only after a period of over 100 sec has elapsed.[*] The net angle of attack is equal to the wind input for all frequencies above about $\omega = 0.02$ rad/sec.

The constraint of $\varphi = 0$ and $\dot{\varphi} = 0$ further dictate that no net pitching moments exist from the rate derivatives, so the ideal thrust vector angle required to maintain constant pitch angle is:

$$\beta_{ideal} = \alpha(M_\alpha/M_\beta)$$

(15)

$$= 0.12\alpha, \qquad \text{at } t = 77 \text{ sec}$$

Finally, the rigid mode contribution to the bending moment parameter of Table I (at the design condition of t = 77 sec) is found from Eqs. 11 and 15:

$$\mu \equiv 0.091\alpha + 0.2\beta$$

$$= (0.091 + 0.2\, M_\alpha/M_\beta)\alpha$$

(16)

$$= (0.091 + 0.024)\alpha \qquad \text{at } t = 77 \text{ sec}$$

$$= 0.115\alpha$$

Equation 16 shows that μ is completely dependent on α, and is therefore dominated by α_w when the pitch attitude is held constant.

―――――――――――

[*] Eighty-six percent of α_w is reached in $2T_2$ ($2 \times 0.018^{-1} \doteq 2 \times 55 = 110$ sec).

44

These simplified equations permit easy calculation of the time response to the gust of the constant φ case, by either digital or analog computation, or by partial fraction expansions of the input times transfer responses to a succession of ramp inputs, comprising the trapezoidal wind spike shown in Fig. 10 (e.g., see Ref. 21). The resulting time history is shown in Fig. 11. The net acceleration, $\ddot{x}_{max} \doteq 0.15g$, is surprisingly low, considering that the peak bending load parameter of $\mu = 0.96$ considerably exceeds the safety level of $\mu = 0.75$.

The fact that the limiting μ is reached near the first corner of the wind spike in Fig. 11 implies that a rapid response wind-relief system is required to accomplish any alleviation. Fortunately, Fig. 11 also shows that the thrust control angle, β, required to hold $\Delta \varphi = 0$ lies well below its saturation limit of 5 deg. This means that there probably will be sufficient margin of control moment available to perform the required weathercock maneuver. Thus this extremely simple analysis has revealed several important insights into the sources of gust-induced bending moments, has indicated crucial information on the need for load relief, and has shown the possibility of achieving it.

Separate approximate computations were made with the pitch attitude loop closed with an automatic flight control system closely approximating the fully manual control loop (described in Appendix A). The resulting bending moment parameter was $\mu = 1.32$, worse than for $\varphi = 0$ as expected. Load relief is obviously necessary since both the foregoing values of μ_{max} exceed the criterion level of $\mu \leq 0.75$.

D. LOAD-RELIEF LOOP

Considerable effort was spent in gaining a good understanding of the load-relief synthesis problem. After this work was complete, Refs. 38 and 39 appeared; since these reports include similar results, the presentation herein will be brief.

A number of sensors are candidates for feedback in a load-relief loop. These could include strain gauges to measure the critical stress points directly, optical deformation sensors, angle-of-attack vanes; an array of differential pressure sensors to measure the aerodynamic load, and

finally, a sensitive transverse accelerometer. In a more exhaustive investigation, all of these would be considered, but the scope of the present study was limited to a transverse accelerometer sensor.

The placement of the accelerometer is critical from the standpoints of both closed-loop stability and practical considerations.

The load accelerometer senses wind input by the wind's effect on the vehicle, which shows up as translational and angular accelerations. Because of the low lift/mass ratio of a slender booster, the wind-induced accelerations are low and hard to distinguish from the accelerations due to the thrust vector control. The situation is shown in the sketch below, where the instantaneous centers of rotation, "ICR," for crosswind and thrust-vector control forces are also shown.* If the
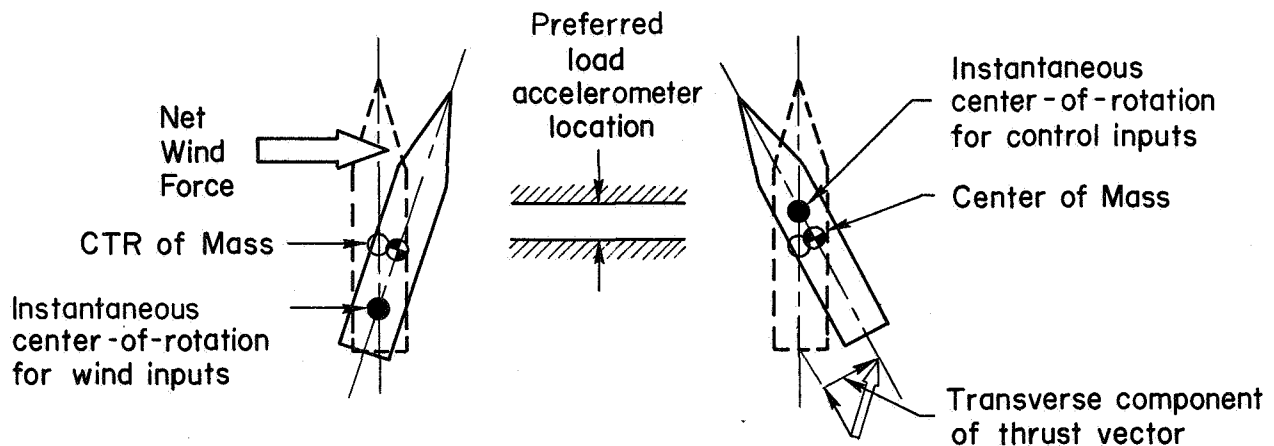
Sketch Showing Instantaneous Centers-of-Rotation (ICR)
for both Wind and Control Inputs

sensor is placed near the ICR for wind inputs (which is behind the c.g. for aerodynamically unstable vehicles) then it won't pick up the desired signals at all. If it is placed far ahead of the center of rotation for thrust control inputs, which is ahead of the c.g., then it will pick up as much signal due to control inputs as it does to wind inputs. Therefore,

---

*The instantaneous center of rotation is defined as that point on a body for which the net transverse accelerations induced by a force acting at a specified point (the center of percussion) on the body is initially zero.

the ideal location from practical considerations is as near to the control ICR as permitted by the availability of space. Although its ideal location changes with time of flight, it is only necessary to optimize the load accelerometer location for the wind spike condition, because the load-relief loop need be used only during this period.

The piloted load-relief loop was then synthesized by iterative analysis, with a display of acceleration near the control ICR as a starting point. A system survey for the piloted load-relief loop is shown in Fig. 12. The following is a summary of the assumptions and conclusions reached during the evolution of this system:

Assumptions

1. The proposed load-relief system operates with the augmentation loop closed.

2. The pilot is only required to act as a pure gain at very low frequency. The pilot delay times and low frequency phase contributions were neglected in closing the outer low-bandwidth loop:

$$Y_{p\ddot{y}} \doteq K_{p\ddot{y}}$$

Implications

1. For best stability margins, a series of system surveys showed that the accelerometer should be placed just to the rear of the control ICR and that low-pass, second-order filtering of the elastic mode inputs to the accelerometer would be feasible and advisable. The best sensor location is near Station +11.4, which lies in a "feasible" area of Fig. 1, about 10 m ahead of the c.g.

2. To provide the tight-enough loop at the dominant low-frequency portion of the wind spike (below $\omega_i = 0.1$ rad/sec), outer-loop integration at low frequencies is required. This integrator also helps to attenuate pilot remnant inputs to the elastic modes, as in the attitude loop. The integrator is placed downstream of the pilot's stick, enabling the pilot to switch from attitude to load-relief modes by merely devoting his full attention to the accelerometer display.

3. Further lead/lag equalization of the display or by the pilot may be desirable. This is to increase the permissible crossover frequency toward 1.0 to 2.0 rad/sec, while retaining greater phase margin

at crossover. A better closed-loop damping ratio
results, which minimizes the transient overshoots
at wind spike frequencies.

4. The closed-loop integration pole drives into the
unstable g'/V path mode described previously. This
is unavoidable in any good load relief system having
a sufficiently tight response at the wind spike
frequencies (e.g., see Ref. 38). It does mean that
the pilot cannot maintain both φ and $\ddot{\gamma}_a$ small, and
must use every clue and logic at his command to
switch back to the attitude loop as promptly as
possible.

A lower gain of $K_{p\dot\gamma}$, which would place the very low-frequency root
exactly on the origin, corresponds to the "Drift Minimum" mode of opera-
tion (Ref. 37). Thus in a steady-state condition the booster would point
just enough into a steady wind so that the sum of the thrust, lift, and
weight vectors would lie parallel to the desired flight direction (making
$\dot{x} \rightarrow 0$ as $t \rightarrow \infty$). Thus the new trajectory would lie parallel to, but be
displaced from, the desired trajectory by an amount roughly proportional
to the total crosswind force impulse in the wind spike.

The dynamic response of the final load-relief system to the wind spike
is shown in Fig. 13, where the closed-loop rigid-body contribution to the
bending moment parameter, μ, is compared to the $\varphi = 0$ case examined
earlier. The peak value of $\mu_{max} = -0.35$ is well within the specified
limit of $\mu = 0.75$, and in fact shows a slight overcompensation for this
particular wind spike. The computed load-relief parameters for the previous
and present computations are compared in Table VII.

A remaining problem for load relief is when to switch to it from the
basic trajectory control. As noted previously, the low-frequency accele-
rations due to the wind spike are not large, and may be masked by elastic
mode vibrations due to turbulence. Probably the best judge (provided suit-
able information is provided to him) is the pilot. By studying a wind profile
an hour or so before launching, and by correlating this against the hundreds
of simulated wind load maneuvers which he would have accomplished prior
to actual flight, a pilot should be able to detect the onset of the real

wind spike and to switch over to the load relief display almost instantly.*

Since he need only adopt a pure-gain behavior, the load relief and pitch attitude display gains can be adjusted so that the required pilot gain is the same in either case and the switchover transients will thereby be minimized. Thus the pilot takes the active role in load relief.

*A directly comparable situation exists during the landing of naval aircraft aboard an aircraft carrier when the carrier wake or "burble" is traversed by the aircraft. The "shape" of the burble and the required control action can be learned, but the time of occurrence and degree of control action vary with each landing. Pilots cope with this burble disturbance routinely, and quickly learn to detect its onset.

49

SECTION VIII

PILOT-REMNANT-INDUCED VIBRATIONS

A. GENERAL APPROACH

This section demonstrates the use of available pilot remnant data to analyze some of the effects of inadvertent pilot control movements.[*] Such movements comprise (a) large discrete, but "wrong," motions, typified by inadvertent reversals of polarity which frequently accompany learning, and (b) fine movements of varying smoothness and frequency, typified by the pilot "remnant" observed in fixed-base measurements of the pilot's quasi-linear characteristics. For trained pilots the first type of movements are eliminated; this leaves only the remnant to consider. Unless properly filtered, the higher frequency components of the remnant will excite the elastic modes, and thus produce undesirable vibrations at the pilot's station. As noted in previous sections, the control motions required for guidance and wind load relief are at low frequency; hence they will not excite the bending modes.

B. ANALYSIS

Following the model laid down in Section IV, the remnant is assumed to be injected into the visual perception point of the pilot/vehicle system, while the pilot is closing the pitch attitude loop in either the fully manual or the stability-augmented configurations. The block diagram for the analysis is given in Fig. 14.

The remnant is represented as a power spectrum, Φ_{nn_e}, of filtered white noise injected into the visual perception point of the pilot/vehicle system. The spectrum, Φ_{nn_e}, and shaping filter, $H_n(j\omega)$, are related by

$$\Phi_{nn_e} = \left| H_n(j\omega) \right|^2 \tag{17}$$

---

[*]Excitation of bending modes by the fine-grained wind profile and by atmospheric turbulence is beyond the scope of this study.

and the mean-square value is defined as:

$$\sigma_{\bar{n}}^2 = \frac{1}{2\pi} \int_0^\infty \Phi_{nn_e}(\omega)\,d\omega \tag{18}$$

The most applicable remnant data (from Ref. 15) has already been given in Fig. 4. As indicated on that figure, a reasonable representation of the shape of these spectra is a first-order filter having the following characteristics:

$$H_n(j\omega) = \frac{2\sigma_n\sqrt{\omega_n}}{j\omega + \omega_n} \tag{19}$$

where:

$$\omega_n \doteq 1.0 \text{ rad/sec}$$

The conclusions which will be made have been found to be relatively insensitive to the above representation insofar as the chosen shape of $H_n(j\omega)$, or to moderate variations in ω_n. The importance of the level of σ_n will be discussed in a later section; until then it is convenient to carry out the analysis in a normalized fashion.

The analysis itself makes use of standard techniques (see, e.g., Ref. 42). Given the transfer function characteristics of a constant-coefficient linear system, $Y(s)$, and a stationary random input with the spectrum $\Phi_i(\omega)$, the system output spectrum is given by:

$$\Phi_0(\omega) = |Y(j\omega)|^2 \Phi_i(\omega) \tag{20}$$

In the present case we are interested in the acceleration at the pilot's station induced by the remnant, with the attitude loop closed (Fig. 14). The total acceleration will be separated into that due to tne rigid-body modes, $\ddot{\gamma}_p^R$, and that due to the elastic modes, $\ddot{\gamma}_p^E$. These components are given by:

$$\ddot{\gamma}_p^R = F_\alpha \alpha + F_\beta \beta + \frac{l_p}{57.3}\ddot{\varphi}$$

$$\ddot{\gamma}_p^E = K_3\ddot{\eta}_1 + K_4\ddot{\eta}_2 \tag{21}$$

51

For the fully manual case, a single-loop closure, the transfer functions are computed from:

$$\frac{\ddot{\gamma}_p^i}{n}\Bigg]_{\varphi_{RG} \to \beta_c} = \frac{Y_{P_A} Y_{\ddot{\gamma}_p^i}}{1 + Y_{D_\varphi} Y_{P_A} Y_{\varphi_{RG}}} \tag{22}$$

where $\qquad i = $ elastic or rigid

and the subscript notation $\varphi_{RG} \to \beta$ implies that the attitude loop is closed. The normalized output spectrum is then given by:

$$\frac{\Phi_{\ddot{\gamma}_p^i}}{\sigma_n^2} = \left| \frac{\ddot{\gamma}_p^i}{n}\Bigg]_{\varphi_{RG} \to \beta_c}^{(j\omega)} \right|^2 \frac{\Phi_{nn_e}}{\sigma_n^2} \tag{23}$$

The pertinent transfer functions are given in Table IV-A-2.

With the augmented vehicle control system plus series pilot, two loops are closed and both affect the accelerations felt by the pilot (see Ref. 22 for details of this multiloop analysis procedure). Accounting for all the block algebra is straightforward and yields the closed-loop acceleration response to remnant as:

$$\frac{\ddot{\gamma}_p^i}{n}\Bigg|_{\substack{\dot{\varphi}_{RG} \to \beta_c \\ \varphi_{AG} \to \beta_p}} = \frac{Y_{P_c} Y_{E_3} Y_{E_1} Y_{\ddot{\gamma}_p^i}}{1 + Y_{E_1} Y_{E_2} Y_{\dot{\varphi}_{RG}} + Y_{D_\varphi} Y_{P_c} Y_{E_3} Y_{E_1} Y_{\varphi_{AG}}} \tag{24}$$

$$i = \text{rigid or elastic}$$

The output spectrum is computed from

$$\frac{\Phi_{\ddot{\gamma}_p^i}}{\sigma_n^2} = \left| \frac{\ddot{\gamma}_p^i}{n}\Bigg]_{\substack{\dot{\varphi}_{RG} \to \beta_c \\ \varphi_{AG} \to \beta_p}} \right|^2 \frac{\Phi_{nn_e}}{\sigma_n^2} \tag{25}$$

Transfer functions for this case are also listed in Table IV-C-1.

C. RESULTS

When the operations indicated by Eq. 20 are carried out, the transverse vibration spectra induced by remnant are those given in Fig. 15. Note that the spectra shown in Fig. 15 have been normalized by the rms level of the remnant input, σ_n^2 (cm^2), which was inserted at the visual perception point of the pilot, the display, see Fig. 14. For the fully manual case, Fig. 15 shows that the vibrations felt by the pilot are dominated by the first bending mode (near $\omega = 7.5$ rad/sec, or about 1.19 cycles/sec) while the second bending mode and the rigid-body contributions are much smaller contributors.

The theoretical effectiveness of the augmentation in reducing the normalized bending vibrations is also illustrated in Fig. 15. The second bending mode is barely excited (it's not visible on the scale of Fig. 15), and even the first is reduced by five orders-of-magnitude from the fully manual case. This is as would be expected from comparing the relative amplitudes of the closed-loop magnitude plots of Figs. 6 and 9 near $\omega = 7.5$ rad/sec. The rigid-mode remnant contributions to the power spectrum at very low frequency ($\omega \doteq 0.1$ rad/sec) are reduced in the augmented case to a factor of $\Phi_{augmented}/\Phi_{manual} = 0.46/0.80 = 0.58$. This would be expected, since the remnant acts as a command input to the attitude loop, and the corresponding squared ratio of the closed-loop attitude response magnitudes from Figs. 6 and 9 is $|Y_{CL}|^2_{augmented}/|Y_{CL}|^2_{manual} = (0.76)^2 = 0.58$.

The appearance of the dip in the rigid-mode contributions near $\omega = 0.45$ rad/sec in Fig. 15 is due to a pair of zeros in the acceleration transfer function. Their position at low frequency on the $j\omega$-axis results from the extreme forward location of the pilot, whereby he picks up predominantly pitching acceleration from the rigid modes. At some frequency (about 0.45 rad/sec for this flight condition and body station) the phasing between the translational and angular accelerations is such that they nearly cancel, leaving the dip in the rigid-body frequency response shown in Fig. 15. This dip in acceleration response is present at some frequency for all stations ahead of the control ICR with reducing frequency for more forward locations.

53

If the level of the remnant is assumed the same for both the fully manual and augmented manual systems the effectiveness of the augmentation in reducing the accelerations due to remnant felt by the pilot can be seen by comparing the normalized outputs given in Fig. 15, i.e.,

$$\frac{\left(\sigma\ddot{\gamma}_p^E\right)_{augmented}}{\left(\sigma\ddot{\gamma}_p^E\right)_{fully\ manual}} = \frac{\left(\sigma\ddot{\gamma}_p^E/\sigma_n\right)_{augmented}}{\left(\sigma\ddot{\gamma}_p^E/\sigma_n\right)_{fully\ manual}} = \frac{0.10}{30.9} = 0.0032$$

$$\frac{\left(\sigma\ddot{\gamma}_p^R\right)_{augmented}}{\left(\sigma\ddot{\gamma}_p^R\right)_{fully\ manual}} = \frac{\left(\sigma\ddot{\gamma}_p^R/\sigma_n\right)_{augmented}}{\left(\sigma\ddot{\gamma}_p^R/\sigma_n\right)_{fully\ manual}} = \frac{0.42}{4.4} = 0.096$$

Besides the effects of the augmentation loop described above, it has additional vibration attenuating benefits because of a reduction in the level of σ_n^2. As explained in Section III-D, the augmented vehicle, which appears as a K/s-like controlled element, will not require lead equalization by the pilot, and will not engender as much remnant as the fully manual case. For example, in Fig. 4, using the Pilot 8 data, the ratio of σ_n^2 for $Y_c = K_c/s$ to σ_n^2 for $Y_c \doteq K_c/s^2$ is approximately the ratio of their dc spectrum levels (corresponding to the difference in power dB of about -6 dB), which implies a factor of two improvement for the augmented case.

The analytic model for the remnant spectrum shown in Fig. 4 well approximates the Pilot 8, $Y_c = K_c/s^2$ data and as indicated has a level of $\sigma_n = 0.56$ cm; a reasonable value for the Pilot 8, $Y_c = K_c/s$ data is $\sigma_n = 0.28$ cm. Combining these values with the normalized outputs given in Fig. 15 results in the following remnant-induced accelerations:

For Fully-Manual Control:

Elastic: $\sigma\ddot{\gamma}_p^E = \left(\sigma\ddot{\gamma}_p^E/\sigma_n\right)\sigma_n = (30.9)(0.56) = 17.3$ m/sec^2

Rigid: $\sigma\ddot{\gamma}_p^R = \left(\sigma\ddot{\gamma}_p^R/\sigma_n\right)\sigma_n = (7.8)(0.56) = 4.4$ m/sec^2

For Augmented-Vehicle Control:

Elastic: $\sigma_{\ddot{\gamma}_p}^{E} = \left(\sigma_{\ddot{\gamma}_p}^{E}/\sigma_n\right)\sigma_n = (0.10)(0.28) = 0.028 \text{ m/sec}^2$

Rigid: $\sigma_{\ddot{\gamma}_p}^{R} = \left(\sigma_{\ddot{\gamma}_p}^{R}/\sigma_n\right)\sigma_n = (0.42)(0.28) = 0.12 \text{ m/sec}^2$

It should be noted that the above calculation of absolute acceleration levels is based on data from fixed base, single pilot experiments with simple controlled elements. Insofar as absolute level of motions, there does not exist enough remnant data to allow a great deal of confidence in extrapolating these to the moving base, complex controlled element represented by the booster. Extensive research in this area is urgently required before accurate engineering predictions can be made of remnant effects in elastic vehicles.

SECTION IX

CONCLUSIONS

The problem of designing manual control systems for large flexible boosters of the Saturn V class has been treated by extensions of recently developed system analysis techniques which employ mathematical models for the human pilot. Because many of the detailed conclusions are presented at the end of each major section and in Tables V, VI, and VII only the most important are given below.

A quasi-linear pilot model consisting of a random-input describing function, a set of parameter adjustment rules, plus a remnant to account for inadvertent control action, was used for: analyzing the tracking of guidance commands, the stabilization of the boost vehicle, the regulation against various random disturbances, and the estimation of remnant-induced vibrations. For these applications, measured data on the describing function parameters in a similar laboratory task were available to give confidence in the predicted results. In cases of less random inputs, such as wind spikes and isolated oscillations of poorly damped elastic modes, there is less confidence in the random-input model predictions. Gross trends in the pilot/vehicle response should be predicted adequately for preliminary design purposes, however.

This model was applied to the analysis of a fully-manual booster control and the synthesis of a series-pilot-plus-augmented-vehicle pitch attitude control system. Fully manual control during the worst flight condition was predicted to be barely possible, even with only one axis to control. (Page 31 and Table V give a summary of detailed analytical predictions for fully-manual control.)

The final mechanization for the augmented manual control system is given in Fig. 16. This system was predicted to have good stability, accurate attitude tracking performance, good handling qualities, and a wide tolerance to flight condition, pilot, and system parameters.

A load relief mode, integrated with the attitude mode, was evolved in which the pilot could play the dominant role in compensating for large jet stream wind spikes. Significant load relief is possible from the proposed system. The ratio of: maximum-bending-stress:design-stress-limit was reduced from 1.32 with fully manual control of attitude only to −0.36 with augmented manual control using the load relief mode. It is suggested that the pilot's ability to learn, during countdown, the control action required to cope with the persistent portions of the wind profile existing just before launch be further exploited.

A noise injection model for the pilot's remnant was used to compute the self-induced vibrational accelerations felt by the pilot during closed-loop tracking of attitude commands. The first elastic bending mode was shown to be dominant over rigid or other modes during fully manual control, but, due to the stick filter and other equalization, it was effectively suppressed to below the rigid mode levels in the augmented vehicle case.

It is recommended that the systems proposed herein be tested by simulation to validate and refine the approach techniques. Particularly needed is applied research on: the nature of pilot remnant during the control of large elastic vehicles, pilot models to cope with low frequency sinusoidal vibrations felt by the pilot, and the pilot's higher level mode switching behavior.

TABLE I

EQUATIONS OF MOTION

Equations of Motion

$$\ddot{x} = F_\alpha \alpha + F_\varphi \varphi + F_\beta \beta$$

$$\ddot{\varphi} = M_\alpha \alpha - M_\beta \beta$$

$$\varphi_{AG} = \varphi + C_1 \eta_1 + C_2 \eta_2$$

$$\dot{\varphi}_{RG} = \dot{\varphi} + C_3 \dot{\eta}_1 + C_4 \dot{\eta}_2$$

$$\alpha = \varphi + \alpha_w - \frac{\dot{x}}{V} 57.3$$

$$\ddot{\gamma}_a = F_\alpha \alpha + F_\beta \beta + \frac{l_a}{57.3}(\ddot{\varphi}) + K_1 \ddot{\eta}_1 + K_2 \ddot{\eta}_2$$

$$\ddot{\eta}_1 = 0.46\beta + 0.00077\ddot{\beta} - 2\zeta\omega_{\eta_1}\dot{\eta}_1 - \omega_{\eta_1}^2 \eta_1$$

$$\ddot{\eta}_2 = 0.418\beta + 0.000735\ddot{\beta} - 2\zeta\omega_{\eta_2}\dot{\eta}_2 - \omega_{\eta_2}^2 \eta_2$$

Engine Actuator Dynamics

$$\frac{\beta}{\beta_c} = \frac{27,000}{(s^2 + 18s + 900)(s + 30)}$$

Bending Moment Criterion

$$\mu = \frac{M_x}{M_{design}} = \frac{q\alpha}{q_{max}(11.0)} + \frac{\beta}{5} + 0.9\ddot{\eta}_1 + 0.5\ddot{\eta}_2$$

TABLE II

CONSTANTS AND PARAMETERS

	TIME OF FLIGHT			UNITS
	$t = 10$	$t = 77$ (time of max. q)	$t = 150$	sec
F_α	0.006	0.131	0.006	meters/sec^2/deg
F_φ	0.22	0.36	0.87	meters/sec^2/deg
F_β	0.18	0.30	0.70	meters/sec^2/deg
M_α	0.004	0.14	−0.016	1/sec^2
M_β	0.85	1.15	3.3	1/sec^2
V	25	486	2300	meters/sec
l_a	12.4	10.0	− 4.6	meters
K_1		− 0.70		
K_2		− 0.59		
K_3		4.8		
K_4		−1.1		
$2\zeta\omega_{\eta_1}$	0.032	0.0735	0.0877	rad/sec
$2\zeta\omega_{\eta_2}$	0.100	0.123	0.176	rad/sec
$\omega_{\eta_1}^2$	32	54	77	(rad/sec)^2
$\omega_{\eta_2}^2$	100	151	310	(rad/sec)^2
q	50	3650	100	Kg/n^2
c_1	6.98	8.32	4.4	
c_2	−2.98	1.15	2.46	
c_3	3.15	2.86	0.57	
c_4	4.58	5.16	3.44	

TABLE III

OPEN-LOOP TRANSFER FUNCTIONS

Legend: $\begin{bmatrix} 0.30 \\ 30 \end{bmatrix}$ denotes $\begin{bmatrix} \zeta \\ \omega \end{bmatrix}$, i.e., $\left[s^2 + 2(0.30)(30)s + 30^2 \right]$

$Y(\ )_i$ denotes $\dfrac{(\ )_i}{\beta_c} = \dfrac{N(\ )_i(s)}{\Delta(s)}$

A. BOOSTER PLUS SERVO

1. Lift-off, t = 10 sec

$$\Delta = (s + 0.14)(s + 30)\begin{bmatrix} -0.54 \\ 0.12 \end{bmatrix}\begin{bmatrix} 0.0028 \\ 5.7 \end{bmatrix}\begin{bmatrix} 0.005 \\ 10 \end{bmatrix}\begin{bmatrix} 0.30 \\ 30 \end{bmatrix}$$

$$N_{\varphi_{RG}} = 156(s + 0.016)(s + 4.3)(s - 4.3)\begin{bmatrix} 0.0037 \\ 7.5 \end{bmatrix}\begin{bmatrix} 0.00054 \\ 21 \end{bmatrix}$$

$$N_{\varphi_{AG}} = 86(s + 0.015)(s + 3.8)(s - 3.8)\begin{bmatrix} 0.0085 \\ 14 \end{bmatrix}\begin{bmatrix} -0.0020 \\ 18 \end{bmatrix}$$

2. Maximum q, t = 77 sec

$$\Delta = (s - 0.043)(s - 0.34)(s + 0.40)(s + 30)\begin{bmatrix} 0.005 \\ 7.4 \end{bmatrix}\begin{bmatrix} 0.005 \\ 12 \end{bmatrix}\begin{bmatrix} 0.30 \\ 30 \end{bmatrix}$$

$$N_{\varphi_{RG}} = 162(s + 0.02)(s + 6.6)(s - 6.6)\begin{bmatrix} 0.005 \\ 9.1 \end{bmatrix}\begin{bmatrix} 0.001 \\ 21 \end{bmatrix}$$

$$N_{\varphi_{AG}} = 196(s + 0.02)(s + 4.5)(s - 4.6)\begin{bmatrix} 0.005 \\ 12 \end{bmatrix}\begin{bmatrix} 0.00066 \\ 21 \end{bmatrix}$$

$$N_{\ddot{\gamma}_a} = -26.3(s - 0.042)(s - 1.5)(s + 1.5)(s - 3.6)(s + 3.6)\begin{bmatrix} 0.0048 \\ 10 \end{bmatrix}\begin{bmatrix} 0.00023 \\ 22 \end{bmatrix}$$

$$N_{\ddot{\gamma}_p^E} = 78s^2(s - 0.043)(s - 0.34)(s + 0.40)\begin{bmatrix} 0.0051 \\ 13 \end{bmatrix}\begin{bmatrix} 0.00004 \\ 25 \end{bmatrix}$$

$$N_{\ddot{\gamma}_p^R} = -26,300(s - 0.042)\begin{bmatrix} 0.075 \\ 0.45 \end{bmatrix}\begin{bmatrix} 0.005 \\ 7.4 \end{bmatrix}\begin{bmatrix} 0.005 \\ 12 \end{bmatrix}$$

3. Burnout, t = 150 sec

$$\Delta = (s - 0.021)(s + 30)\begin{bmatrix} 0.083 \\ 0.13 \end{bmatrix}\begin{bmatrix} 0.005 \\ 8.8 \end{bmatrix}\begin{bmatrix} 0.005 \\ 18 \end{bmatrix}\begin{bmatrix} 0.30 \\ 30 \end{bmatrix}$$

$$N_{\varphi_{RG}} = 80(s + 0.00007)(s + 30)(s - 30)\begin{bmatrix} 0.0051 \\ 9 \end{bmatrix}\begin{bmatrix} 0.004 \\ 19 \end{bmatrix}$$

$$N_{\varphi_{AG}} = 140(s + 0.000068)(s + 18)(s - 18)\begin{bmatrix} 0.0053 \\ 11 \end{bmatrix}\begin{bmatrix} 0.0039 \\ 19 \end{bmatrix}$$

TABLE III - Con't

B. DISPLAYS, EQUALIZATIONS, AND GAINS

1. Displays

$$Y_{D_\varphi} = \frac{\varphi_D}{\Delta\varphi} = 0.5 \text{ cm/deg}$$

$$Y_{D_{\ddot{\gamma}_a}} = \frac{\ddot{\gamma}_D}{\ddot{\gamma}_E} = 0.5 \text{ cm/m/sec}^2$$

2. Equalizations and Gains

$$Y_{E_1} = \frac{\beta_c}{\beta_\epsilon} = \frac{25}{(s+5)^2} \quad ; \text{ (Bending Filter)}$$

$$Y_{E_2} = \frac{\beta_f}{\varphi_{RG}} = \left(\frac{K_d}{s} + K_r\right) = K_r\left(\frac{s+0.5}{s}\right) \quad ; \quad \text{(Rigid Mode Lead)}$$

$$Y_{E_3} = \frac{\beta_p}{\delta} = \frac{\kappa_3}{s}$$

t, sec	K_r, deg/deg/sec	κ_3, deg/deg/sec
10	−1.26	0.5
77	−1.26	0.5
150	−0.29	0.5

TABLE III - Concl'd

C. **PILOT DESCRIBING FUNCTIONS**

1. **Fully Manual**

$$Y_{P_A} = \frac{\beta_c}{\varphi_D} = \frac{K_{P_A}(2j\omega + 1)e^{-0.2j\omega}}{\left[\left(\frac{j\omega}{10}\right)^2 + \frac{2(1)(j\omega)}{10} + 1\right]}$$

$$\doteq \frac{K_{P_A}(2j\omega + 1)(-0.1j\omega + 1)}{(0.1j\omega + 1)^3}$$

t, sec	K_{P_A}, deg/cm
10	−1.0
77	−1.0
150	−0.51

2. **Series Pilot—Augmented-Vehicle**

a. **Attitude loop**

$$Y_{P_C} = \frac{\delta}{\varphi_D} = K_{P_C}e^{-0.5j\omega}$$

$$\doteq K_{P_C}\frac{(-0.25j\omega + 1)}{(0.25j\omega + 1)}$$

At t = 77 sec, $K_{P_C} = -0.79$ deg/cm

b. **Load relief loop (t = 77 sec only)**

$$Y_{P_{\ddot{\gamma}}} = \frac{\delta}{\ddot{\gamma}_D} = K_{P_{\ddot{\gamma}}} = -5.14 \text{ deg/cm}$$

62

TABLE IV

CLOSED-LOOP TRANSFER FUNCTIONS

Notation: $\begin{bmatrix} 0.30 \\ 30 \end{bmatrix}$ denotes $\begin{bmatrix} \zeta \\ \omega \end{bmatrix}$, i.e., $\left[s^2 + 2(0.30)(30)s + (30)^2 \right]$

$\dfrac{\ddot{\gamma}_p^E}{n}\Bigg]_{\varphi_{RG} \longrightarrow \beta_c}$ denotes the response of $\ddot{\gamma}_p^E$ to remnant inputs, n, with the φ_{RG}-to-β_c loop closed

A. FULLY MANUAL ATTITUDE CONTROL (see block diagram, Fig. 6)

1. t = 10 sec

$$\frac{\varphi_{RG}}{\varphi_c}\Bigg]_{\varphi_{RG} \longrightarrow \beta_c} = \frac{15,600(s+0.016)(s+0.5)(s+4.3)(s-4.3)(s-10)\begin{bmatrix} 0.0037 \\ 7.5 \end{bmatrix}\begin{bmatrix} 0.00054 \\ 21 \end{bmatrix}}{(s+0.021)\begin{bmatrix} 0.64 \\ 0.84 \end{bmatrix}\begin{bmatrix} 0.14 \\ 5.2 \end{bmatrix}\begin{bmatrix} 0.67 \\ 5.6 \end{bmatrix}\begin{bmatrix} 0.040 \\ 10 \end{bmatrix}\begin{bmatrix} 0.99 \\ 25 \end{bmatrix}\begin{bmatrix} 0.29 \\ 30 \end{bmatrix}}$$

2. t = 77 sec

$$\Delta' = (s+0.041)(s+0.81)(s+5.6)\begin{bmatrix} 0.95 \\ 2.1 \end{bmatrix}\begin{bmatrix} 0.066 \\ 7.4 \end{bmatrix}\begin{bmatrix} 0.014 \\ 13 \end{bmatrix}\begin{bmatrix} 0.99 \\ 25 \end{bmatrix}\begin{bmatrix} 0.29 \\ 30 \end{bmatrix}$$

$$\frac{\varphi_{RG}}{\varphi_c}\Bigg]_{\varphi_{RG} \longrightarrow \beta_c} = \frac{16,200(s+0.02)(s+6.6)(s-6.6)(s+0.5)(s-10)\begin{bmatrix} 0.0050 \\ 9.1 \end{bmatrix}\begin{bmatrix} 0.0010 \\ 21 \end{bmatrix}}{\Delta'}$$

$$\frac{\ddot{\gamma}_p^E}{n}\Bigg]_{\varphi_{RG} \longrightarrow \beta_c} = \frac{15,600s^2(s+0.5)(s-10)(s-0.043)(s-0.34)(s+0.40)\begin{bmatrix} 0.0051 \\ 13 \end{bmatrix}\begin{bmatrix} 0.00004 \\ 25 \end{bmatrix}}{\Delta'}$$

$$\frac{\ddot{\gamma}_p^R}{n}\Bigg]_{\varphi_{RG} \longrightarrow \beta_c} = \frac{-5,250,000(s+0.5)(s-10)(s-0.042)\begin{bmatrix} 0.075 \\ 0.45 \end{bmatrix}\begin{bmatrix} 0.005 \\ 7.35 \end{bmatrix}\begin{bmatrix} 0.005 \\ 12.3 \end{bmatrix}}{\Delta'}$$

3. t = 150 sec

$$\frac{\varphi_{RG}}{\varphi_c}\Bigg]_{\varphi_{RG} \longrightarrow \beta_c} = \frac{4,090(s+0.000066)(s+30)(s-30)(s+0.5)(s-10)\begin{bmatrix} 0.0051 \\ 9 \end{bmatrix}\begin{bmatrix} 0.0040 \\ 19 \end{bmatrix}}{(s-0.00034)(s+0.74)(s+30)\begin{bmatrix} 0.38 \\ 2.2 \end{bmatrix}\begin{bmatrix} 0.0085 \\ 8.8 \end{bmatrix}\begin{bmatrix} 0.92 \\ 15 \end{bmatrix}\begin{bmatrix} 0.0036 \\ 18 \end{bmatrix}\begin{bmatrix} 0.30 \\ 30 \end{bmatrix}}$$

TABLE IV - Con't

B. AUGMENTER LOOP (see block diagram, Fig. 8)

1. t = 10 sec

$$\Delta' = (s + 0.02)(s + 30)\begin{bmatrix} 0.77 \\ 1.1 \end{bmatrix}\begin{bmatrix} 0.99 \\ 3.5 \end{bmatrix}\begin{bmatrix} 0.056 \\ 5.2 \end{bmatrix}\begin{bmatrix} 0.025 \\ 9.9 \end{bmatrix}\begin{bmatrix} 0.30 \\ 30 \end{bmatrix}$$

$$\left.\frac{\varphi_{RG}}{\beta_p}\right]_{\dot{\varphi}_{RG} \to \beta_c} = \frac{3,900(s + 0.016)(s + 4.3)(s - 4.3)\begin{bmatrix} 0.0037 \\ 7.5 \end{bmatrix}\begin{bmatrix} 0.00054 \\ 21 \end{bmatrix}}{\Delta'}$$

$$\left.\frac{\varphi_{AG}}{\beta_p}\right]_{\dot{\varphi}_{RG} \to \beta_c} = \frac{2,150(s + 0.015)(s + 3.8)(s - 3.8)\begin{bmatrix} 0.0085 \\ 14 \end{bmatrix}\begin{bmatrix} -0.0020 \\ 18 \end{bmatrix}}{\Delta'}$$

2. t = 77 sec

$$\Delta' = (s + 0.035)(s + 0.62)(s + 6)(s + 30)\begin{bmatrix} 0.56 \\ 2 \end{bmatrix}\begin{bmatrix} 0.038 \\ 7.2 \end{bmatrix}\begin{bmatrix} 0.018 \\ 12 \end{bmatrix}\begin{bmatrix} 0.30 \\ 30 \end{bmatrix}$$

$$\left.\frac{\varphi_{RG}}{\beta_p}\right]_{\dot{\varphi}_{RG} \to \beta_c} = \frac{4,000(s + 0.02)(s + 6.6)(s - 6.6)\begin{bmatrix} 0.0050 \\ 9.1 \end{bmatrix}\begin{bmatrix} 0.0010 \\ 21 \end{bmatrix}}{\Delta'}$$

$$\left.\frac{\varphi_{AG}}{\beta_p}\right]_{\dot{\varphi}_{RG} \to \beta_c} = \frac{4,900(s + 0.019)(s + 4.5)(s - 4.6)\begin{bmatrix} 0.0050 \\ 12 \end{bmatrix}\begin{bmatrix} 0.00066 \\ 21 \end{bmatrix}}{\Delta'}$$

$$\left.\frac{\ddot{\gamma}_a}{\beta_p}\right]_{\dot{\varphi}_{RG} \to \beta_c} = \frac{-660(s - 0.042)(s - 1.5)(s + 1.5)(s - 3.6)(s + 3.6)\begin{bmatrix} 0.0048 \\ 10 \end{bmatrix}\begin{bmatrix} 0.00023 \\ 22 \end{bmatrix}}{\Delta'}$$

$$\left.\frac{\ddot{\gamma}_p^E}{\beta_p}\right]_{\dot{\varphi}_{RG} \to \beta_c} = \frac{1,950s^2(s - 0.043)(s - 0.34)(s + 0.40)\begin{bmatrix} 0.0051 \\ 13 \end{bmatrix}\begin{bmatrix} 0.00004 \\ 25 \end{bmatrix}}{\Delta'}$$

$$\left.\frac{\ddot{\gamma}_p^R}{\beta_p}\right]_{\dot{\varphi}_{RG} \to \beta_c} = \frac{-660,000(s - 0.042)\begin{bmatrix} 0.075 \\ 0.45 \end{bmatrix}\begin{bmatrix} 0.005 \\ 7.4 \end{bmatrix}\begin{bmatrix} 0.005 \\ 12 \end{bmatrix}}{\Delta'}$$

TABLE IV - Concl'd

3. t = 150 sec

$$\Delta' = (s - 0.00064)(s + 1.8)(s + 7)(s + 30)\begin{bmatrix}0.59\\1\end{bmatrix}\begin{bmatrix}0.0059\\8.8\end{bmatrix}\begin{bmatrix}0.0054\\18\end{bmatrix}\begin{bmatrix}0.30\\30\end{bmatrix}$$

$$\left.\frac{\varphi_{RG}}{\beta_p}\right]_{\dot{\varphi}_{RG} \to \beta_c} = \frac{2{,}000(s + 0.00007)(s + 30)(s - 30)\begin{bmatrix}0.005\\9\end{bmatrix}\begin{bmatrix}0.004\\19\end{bmatrix}}{\Delta'}$$

$$\left.\frac{\varphi_{AG}}{\beta_p}\right]_{\dot{\varphi}_{RG} \to \beta_c} = \frac{3{,}500(s + 0.000068)(s + 18)(s - 18)\begin{bmatrix}0.0053\\11\end{bmatrix}\begin{bmatrix}0.0039\\19\end{bmatrix}}{\Delta'}$$

C. SERIES PILOT/AUGMENTED VEHICLE (OUTER LOOP)

1. Attitude Loop (see block diagram, Fig. 9, 14)

t = 77 sec

$$\Delta'' = (s + 0.018)(s + 4)(s + 6)(s + 30)\begin{bmatrix}0.29\\0.47\end{bmatrix}\begin{bmatrix}0.59\\2.2\end{bmatrix}\begin{bmatrix}0.038\\7.2\end{bmatrix}\begin{bmatrix}0.018\\12\end{bmatrix}\begin{bmatrix}0.3\\30\end{bmatrix}$$

$$\left.\frac{\varphi_{AG}}{\varphi_c}\right]_{\substack{\dot{\varphi}_{RG} \to \beta_c\\\varphi_{AG} \to \beta_p}} = \frac{970(s + 0.02)(s - 4)(s + 4.5)(s - 4.6)\begin{bmatrix}0.0050\\12\end{bmatrix}\begin{bmatrix}0.00066\\21\end{bmatrix}}{\Delta''}$$

$$\left.\frac{\ddot{\gamma}_p^E}{n}\right]_{\substack{\dot{\varphi}_{RG} \to \beta_c\\\varphi_{AG} \to \beta_p}} = \frac{816s^2(s - 0.043)(s - 0.34)(s + 0.40)(s - 4)\begin{bmatrix}0.0051\\13\end{bmatrix}\begin{bmatrix}0.00004\\25\end{bmatrix}}{\Delta''}$$

$$\left.\frac{\ddot{\gamma}_p^R}{n}\right]_{\substack{\dot{\varphi}_{RG} \to \beta_c\\\varphi_{AG} \to \beta_p}} = \frac{-226{,}000(s - 0.042)(s - 4)\begin{bmatrix}0.075\\0.45\end{bmatrix}\begin{bmatrix}0.005\\7.4\end{bmatrix}\begin{bmatrix}0.005\\12\end{bmatrix}}{\Delta''}$$

2. Load Relief Loop (see block diagram, Fig. 12)

t = 77 sec

$$\left.\frac{\ddot{\gamma}_a}{\ddot{\gamma}_c}\right]_{\substack{\dot{\varphi}_{RG} \to \beta_c\\\ddot{\gamma}_a \to \beta_p}} = \frac{840(s - 0.042)(s + 1.51)(s - 1.53)(s - 3.6)(s + 3.7)\begin{bmatrix}0.0048\\10\end{bmatrix}\begin{bmatrix}0.00023\\22\end{bmatrix}}{(s - 0.036)(s + 6.2)(s + 30)\begin{bmatrix}0.40\\0.61\end{bmatrix}\begin{bmatrix}0.68\\1.8\end{bmatrix}\begin{bmatrix}0.029\\7.2\end{bmatrix}\begin{bmatrix}0.016\\12\end{bmatrix}\begin{bmatrix}0.30\\30\end{bmatrix}}$$

TABLE V

ESTIMATED PILOT COMMENTS FOR FULLY MANUAL BOOSTER CONTROL

TECHNICAL FEATURES OF THE ESTIMATED CLOSURE	TRANSLATION INTO LIKELY PILOT COMMENTS
Low-frequency lead equalization is required to achieve stability.	Constant monitoring is required to avoid overcontrol. It is most important not to make a wrong correction since this is likely to result in loss of control. Because reversal errors can be intolerable, the pilot tends to take great care in his control corrections, and to insure that each one is in the proper sense.
The system is conditionally stable; with too-low a gain the penalty is a low-frequency oscillatory divergence; with too-high a gain a higher-frequency oscillatory divergence.	Pilot finds tendency to emphasize control of the high frequencies, which result in large amplitude errors, and not to attempt to correct many of the low-frequency effects.
Both the high- and low-frequency crossover are fairly sensitive to pilot gain adjustment.	While learning, the pilot feels he should be operating with different gains at high and low frequencies to do the best job; subconsciously he doesn't want to do this because of the tremendous and tiring effort involved.
Gain margins are small, i.e., available ranges of pilot lead and gain adjustment are not large.	After learning, the pilot technique which appears best is to reduce the frequency of control actions and stay with fixed gain in order to control both the low and high frequencies to a reasonable degree. Pilot effort has reduced considerably, but he also accepts a larger mean error in tracking.

66

TABLE VI

EVOLUTION OF THE STABILITY AUGMENTATION LOOP MECHANIZATION

FEEDBACK AND EQUALIZATION FORM	FEASIBILITY	COMMENT
1. Pure φ_{AG} (present attitude gyro)	No	Not enough damping to bring roots into left-half plane.
2. Pure $\dot{\varphi}_{RG}$ (present rate gyro)	No	No increase in static stability, for hands-off-flight safety. Second bending mode problems.
3. Combined pure $K_d \varphi_{AG} + K_r \dot{\varphi}_{RG}$ (measured at separate stations)	Maybe	OK for rigid modes. Bending mode problems.
4. $\varphi_{AG} \times \dfrac{\text{lead}}{\text{double lag}}$ (φ_{AG} measured at present attitude gyro location)	Maybe	OK for rigid modes (lead >1.0 sec). OK for bending modes at maximum-q conditions only (lags $\doteq 0.2$ sec each).
5a. $\int \dot{\varphi}_{RG}$ or 5b. φ_{RG} $\bigg\} \times \dfrac{\text{lead}}{\text{double lag}}$ (φ measured at rate gyro location)	Best for stability augmentation	Bending modes OK for three flight conditions (lags $\doteq 0.2$ sec each). Rigid modes OK for lead >1.0 sec.

TABLE VII

LOAD RELIEF PARAMETER FOR VARIOUS CONTROL MODES

(t = 77 sec)

| CONTROL MODE	LOAD PARAMETER, μ
Vehicle alone (no control)	∞ (unstable)
Ideal attitude control, $\Delta\varphi \equiv 0$	0.96
Fully manual, attitude control only	1.32
Pilot plus augmented vehicle, load relief loop closed	−0.36

Distance in meters

Pilot

Attitude Gyro

Feasible Accelerometer Locations

$X_p = -42$

$X_{AG} = -28$

-14.8
-11.8

Rate Gyro

-6.4

-2.9

Geometric Center

$X_{RG} = -10$

(Reference)

$X_{CG_{150}} = 6.8$

$X_a = 11.4$

6.8

$X_{CG_{77}} = 21.4$

Load Relief Accelerometer

$X_{CG_0} = 23.8$

13.9

18.6

22.6

55.0

33.4

42.3

Gimbal
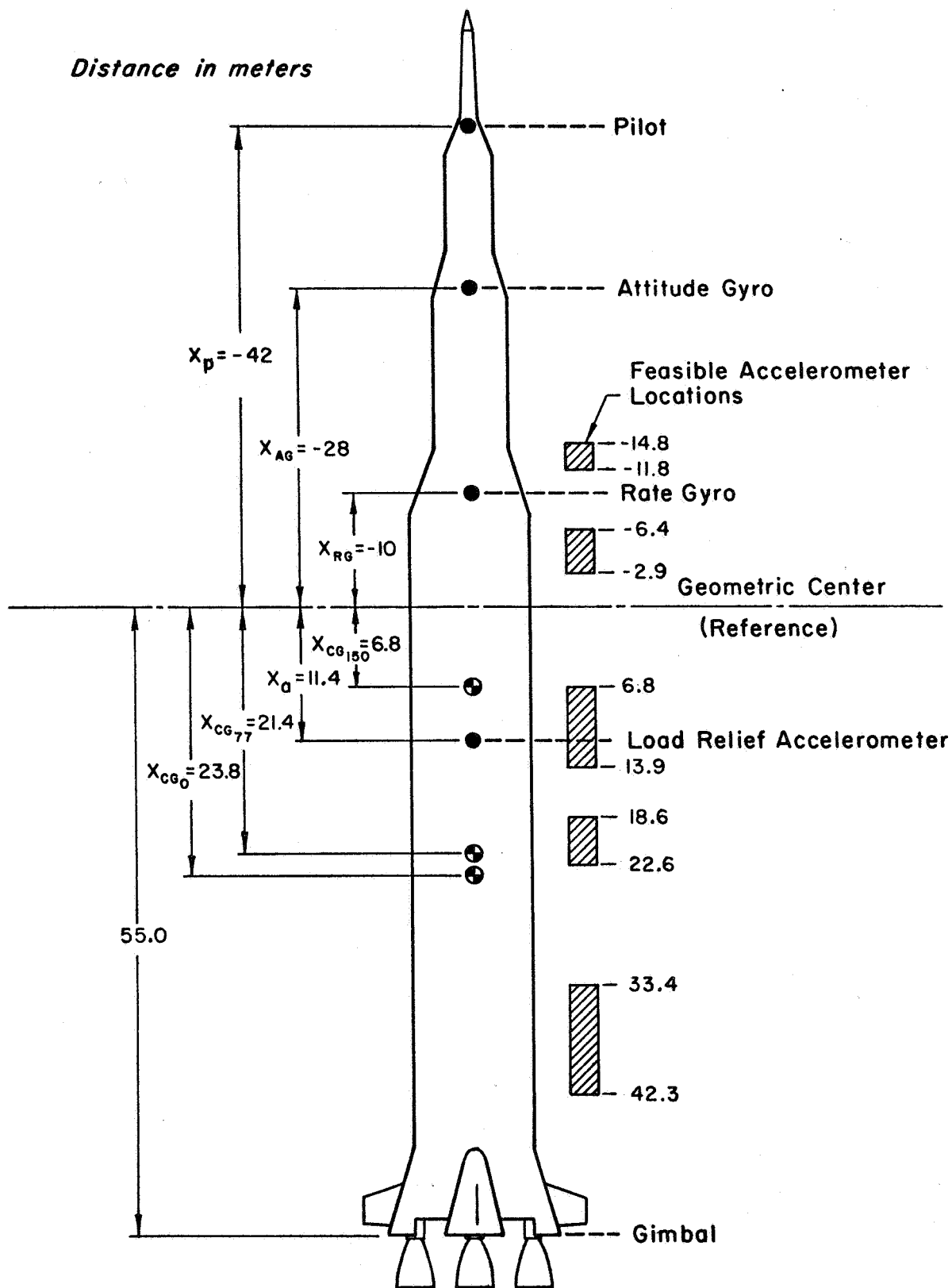
Figure 1. Booster Configuration and Locations of CG, Sensors, and Pilot
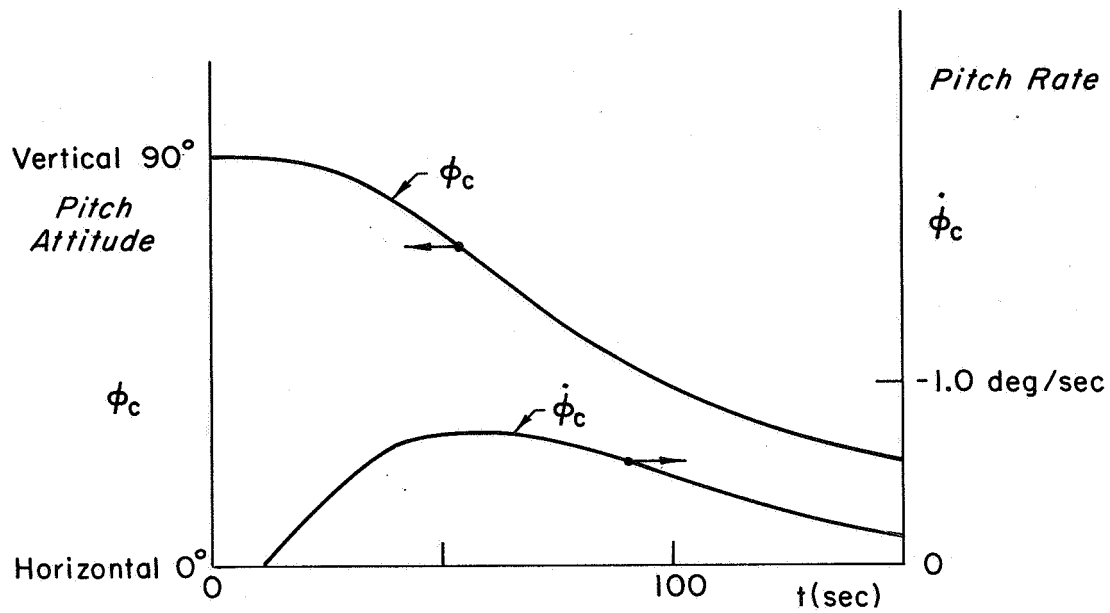
a. Nominal Pitch Attitude Program
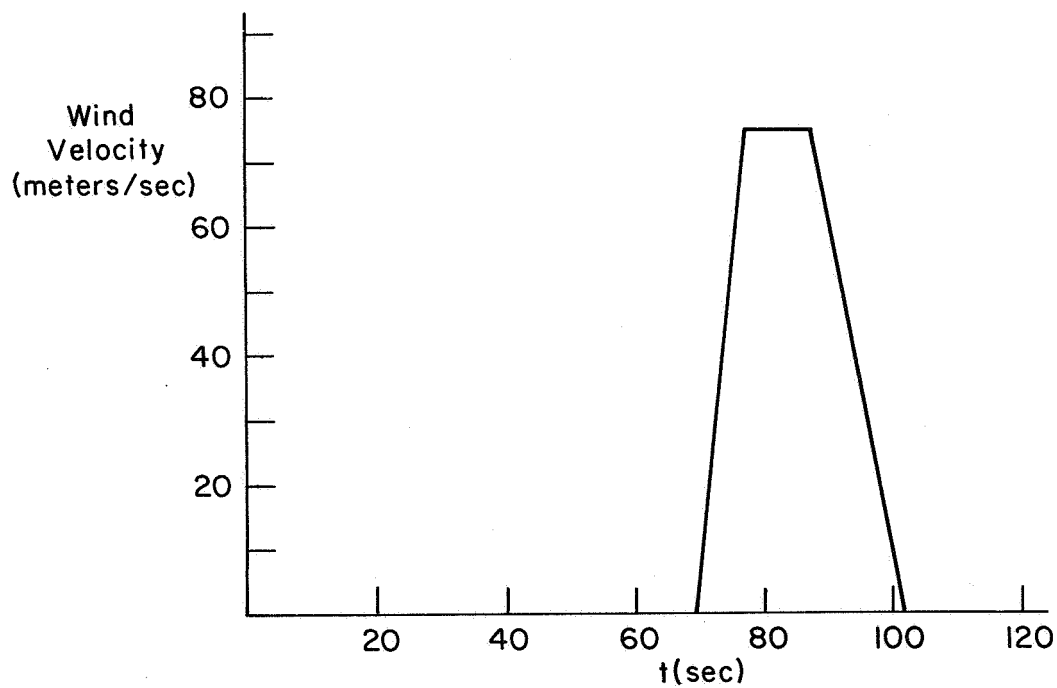
b. Wind Spike

Figure 2.   Commands and Disturbance

70
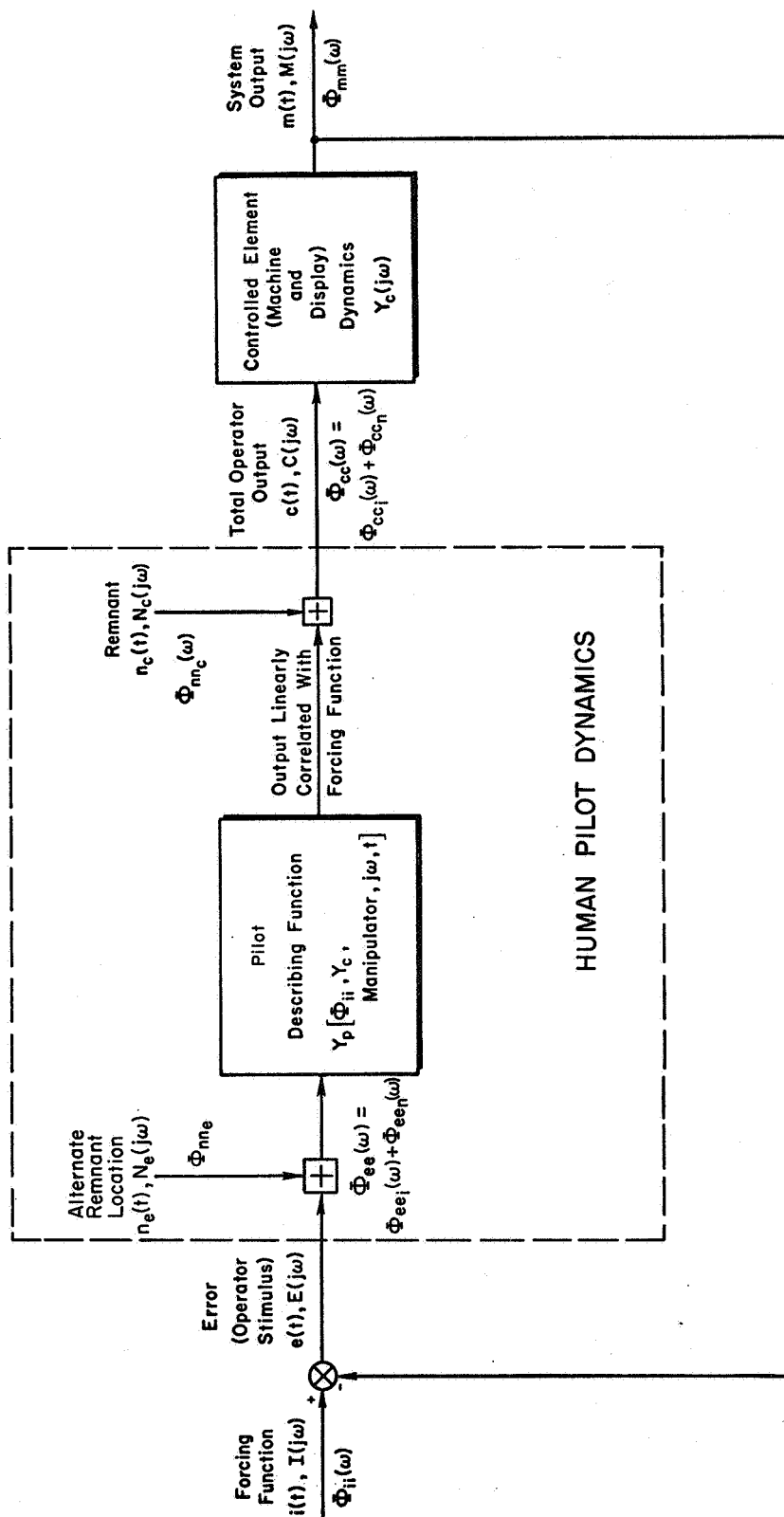
Figure 3. Equivalent Block Diagram of the Pilot/Vehicle System

71

Open
Loop
Remnant

$\dfrac{\text{in}^2\,(\text{CRT})}{\text{rad/sec}}$

Analytic Model

$\left|\dfrac{2\,\sigma_n\,\sqrt{\omega_N}}{j\omega+\omega_N}\right|^2$; $\omega_N = 1.0$; $\sigma_n = .22$ in
($\sigma_n = .56$ cm)

20

0

1.0

Φ_{nn_e}

-20

.1

dB

Linear

-40

.01

	Pilot	Y_c	T_L Req'd
◇	8	$1/j\omega$	No
◈	8	$50/j\omega$	No
◈	8	$2/(j\omega)^2$	Yes
◈	8	$50/(j\omega)^2$	Yes
⌂	7	$6/j\omega$	No
⊙	3	$5/(j\omega)^2$	Yes
⊡	2	$5/(j\omega - 2)$	No
△	5	$2.5/s(s-1.5)$	Yes
O	db	$= 1.0\,\text{in}^2/\text{rad/sec}$	

0.1

1.0

10.0

ω (rad/sec)
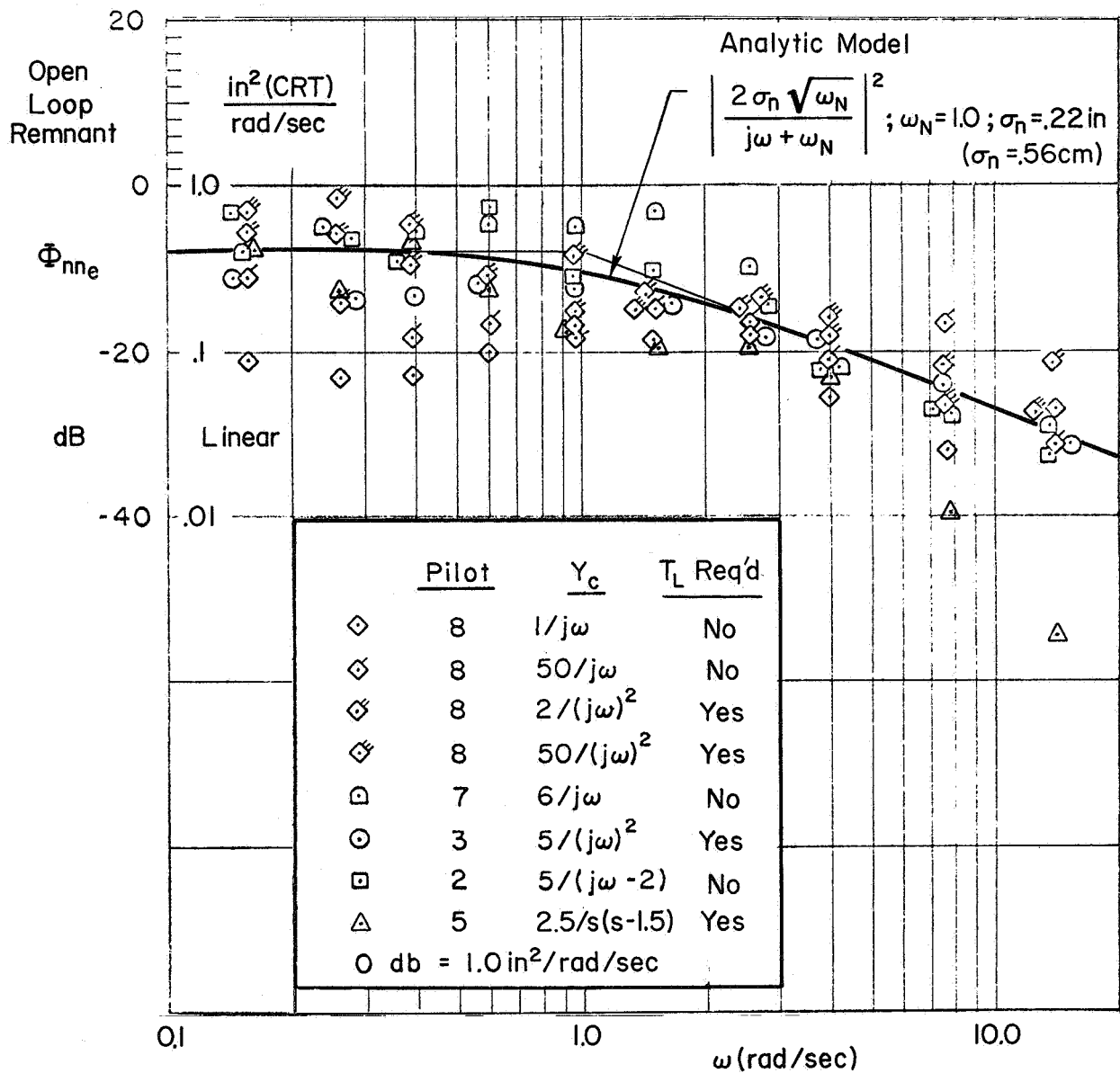
Figure 4. Typical Open-Loop Remnant Data,
Referred to the Displayed Pilot Input (From Ref. 15)

72

$$\frac{\phi_{RG}}{\beta_c} = \frac{162(s+.02)(s+6.6)(s-6.6)\left[s^2+2(.005)(9.1)s+(9.1)^2\right]\left[s^2+2(.001)(21)s+(21)^2\right]}{(s-.04)(s-.34)(s+.40)\left[s^2+2(.005)(7.4)s+(7.4)^2\right]\left[s^2+2(.005)(12)s+(12)^2\right](s+30)\left[s^2+2(.30)(30)s+(30)^2\right]}$$

a) Plot of Roots

b) Bode Plot
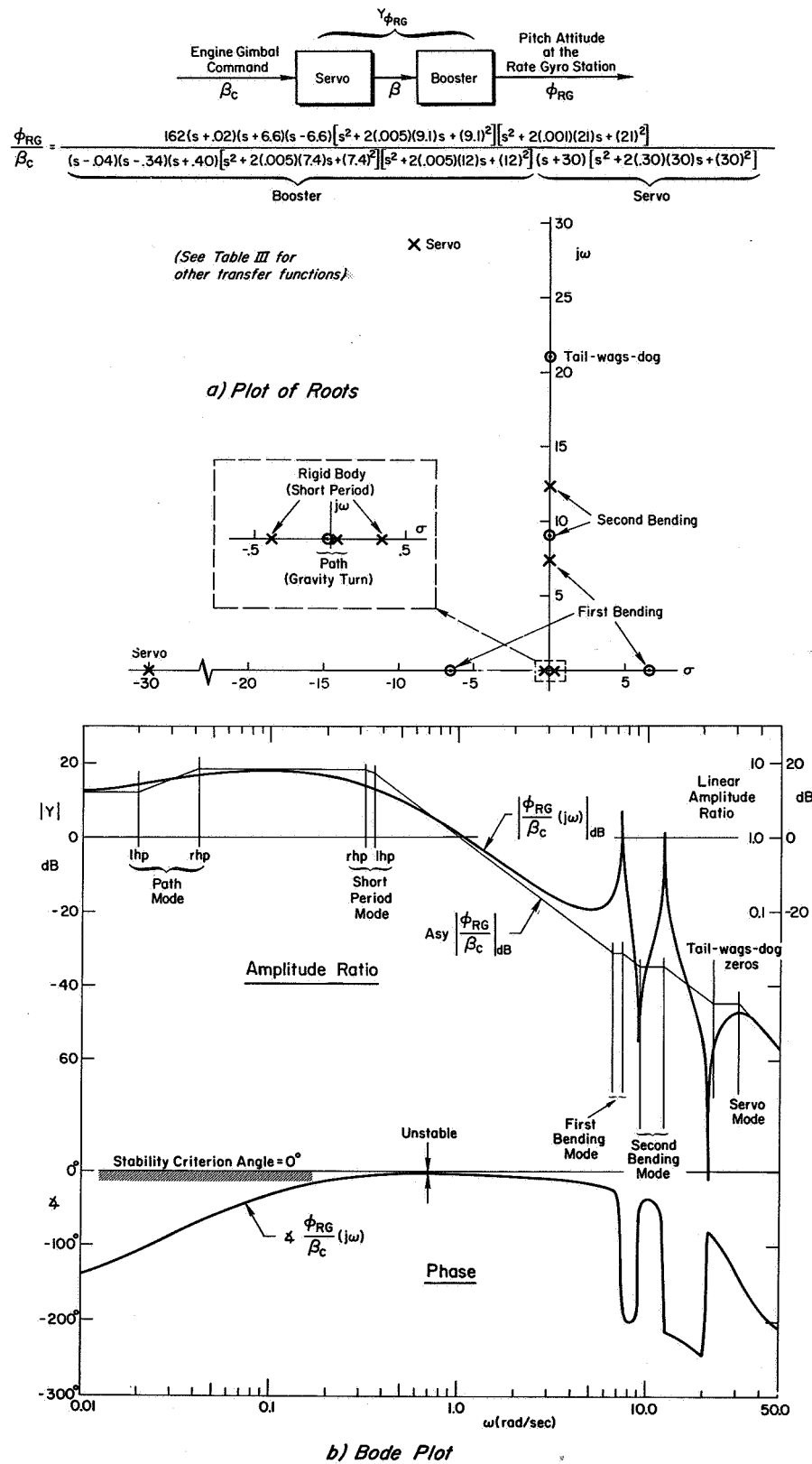
Figure 5. Basic Dynamic Modes of the Booster Plus Servo
(Attitude Response at the Rate Gyro Station for t = 77 sec)

73
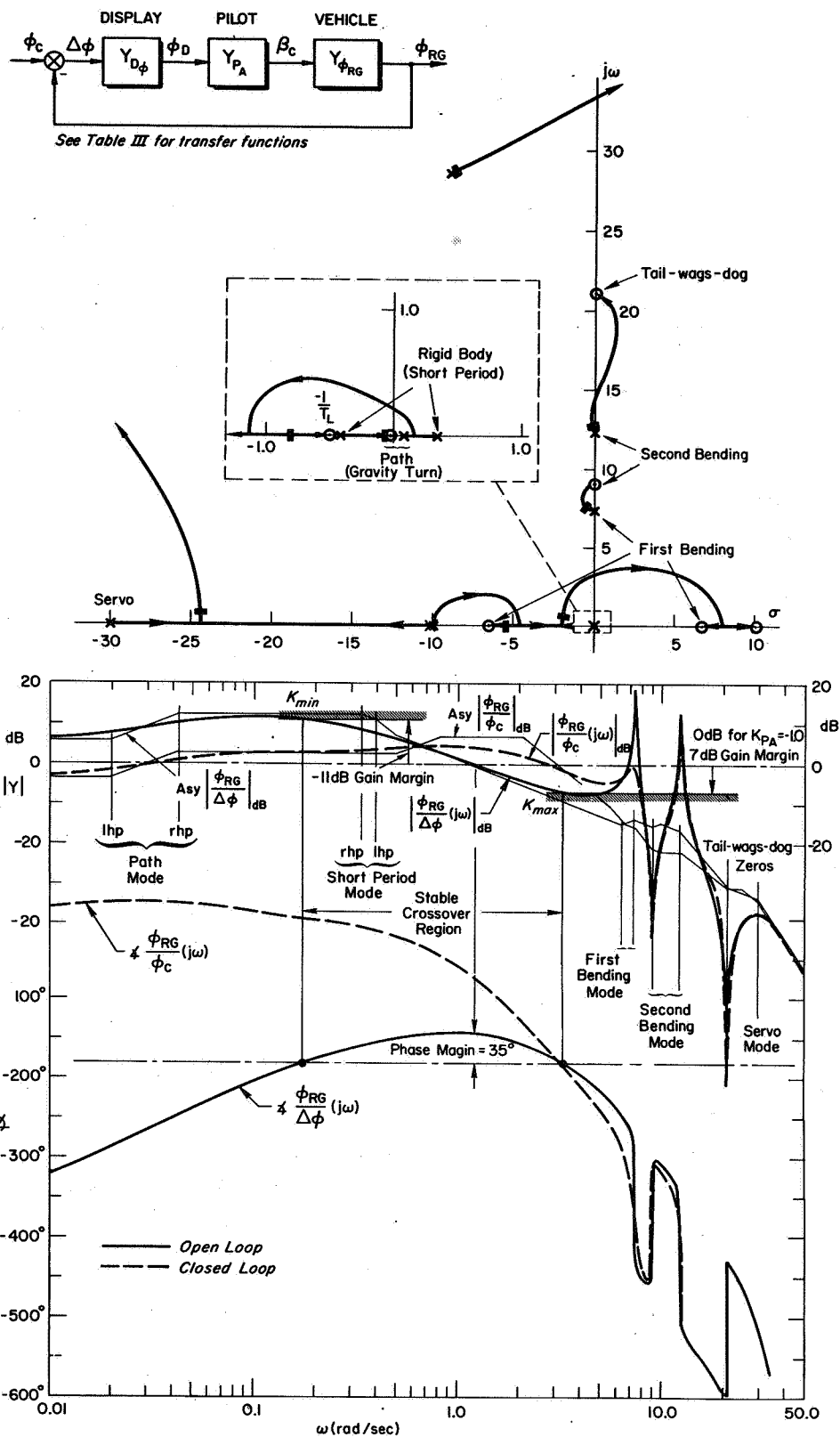
Figure 6. System Survey for Fully Manual Control, t = 77 sec
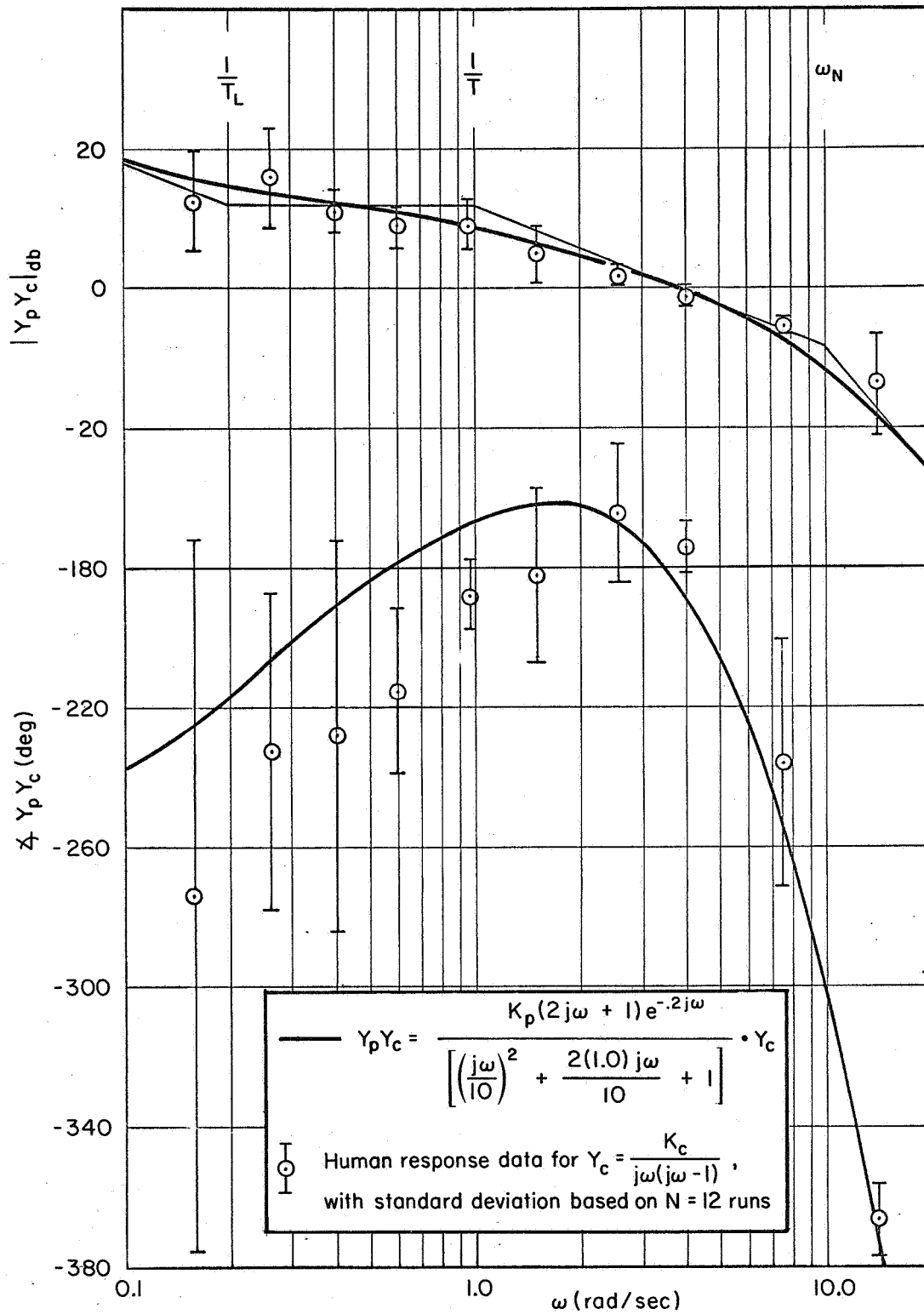
Figure 7. Comparison of Estimated Pilot Describing Function for Booster with Pilot Response Data for a Similar Unstable Controlled Element, $Y_c = K_c/j\omega(j\omega-1)$

75
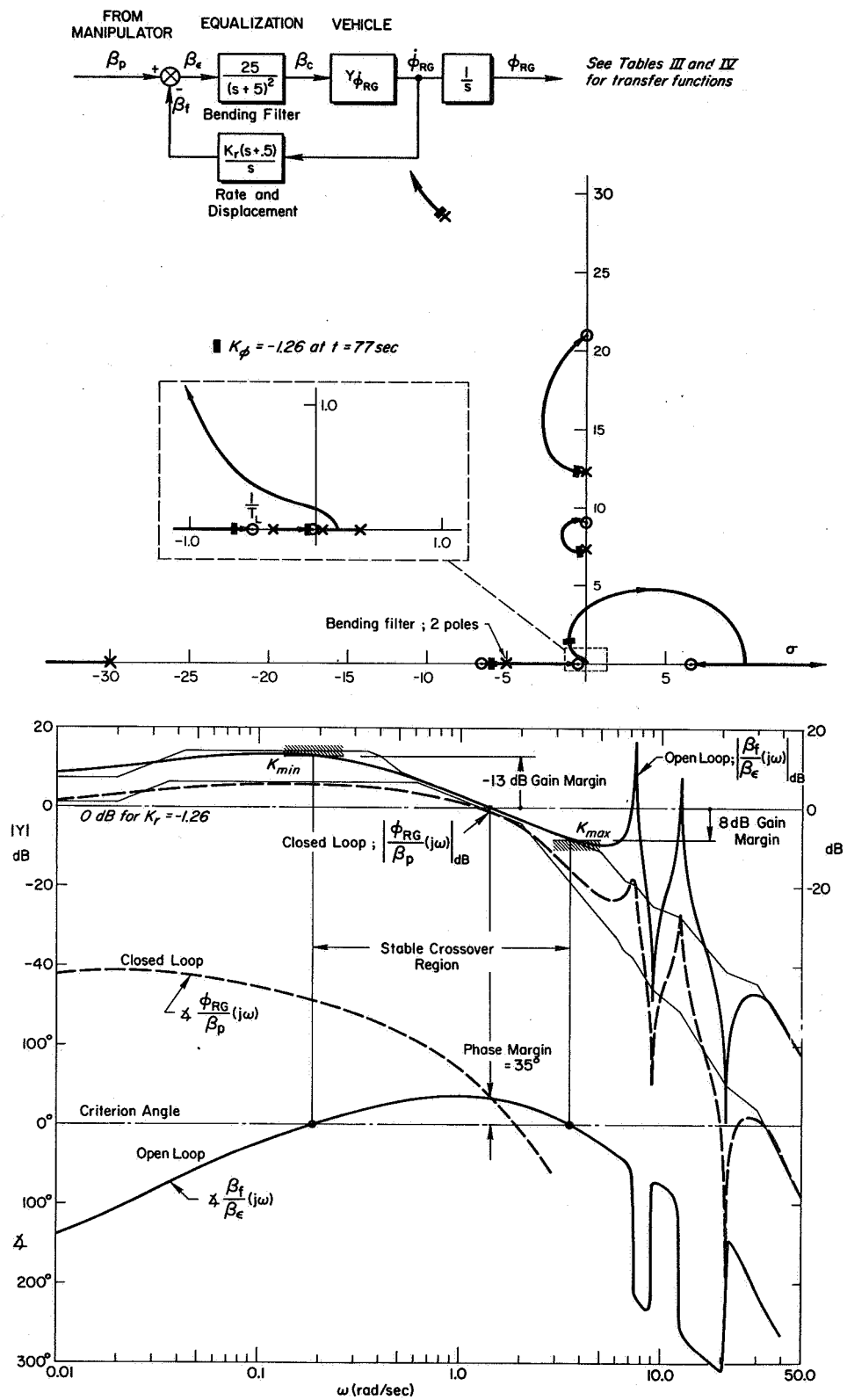
Figure 8.   System Survey for Attitude Stability Augmenter Loop
(t = 77 sec)
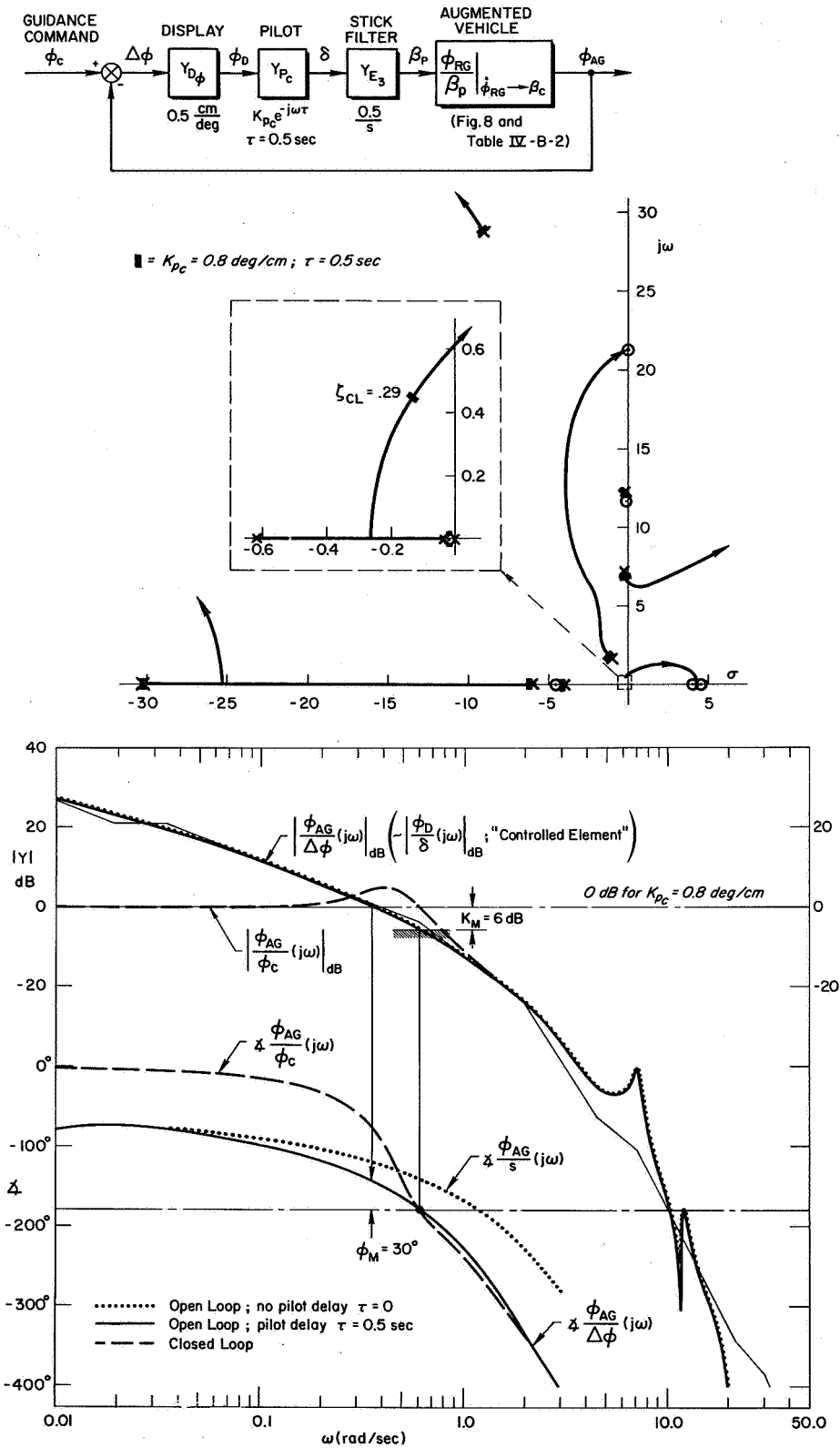
Figure 9. System Survey for the Augmented Manual Guidance Loop, t = 77 sec
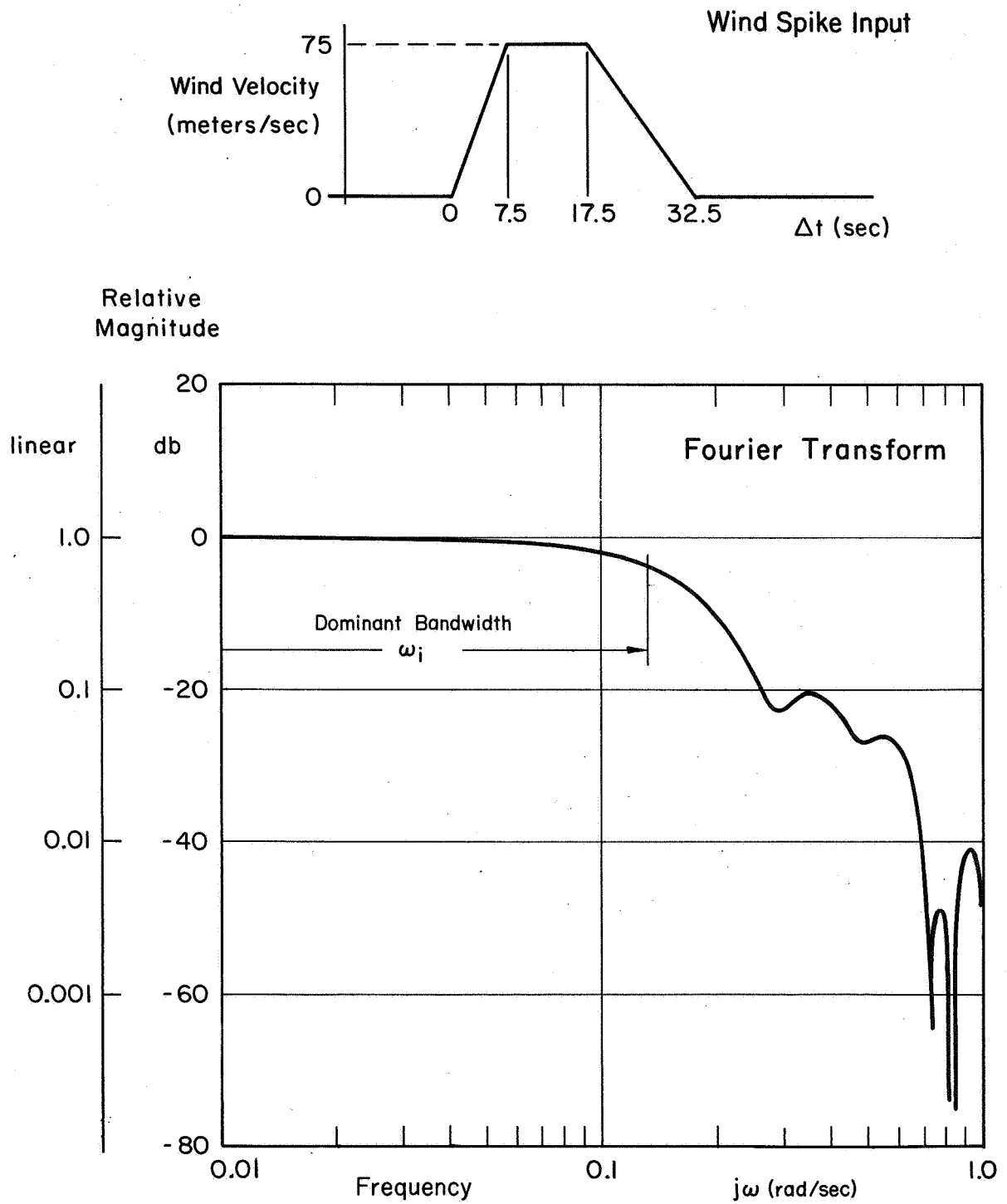
Figure 10. Equivalent Spectrum of Wind Spike
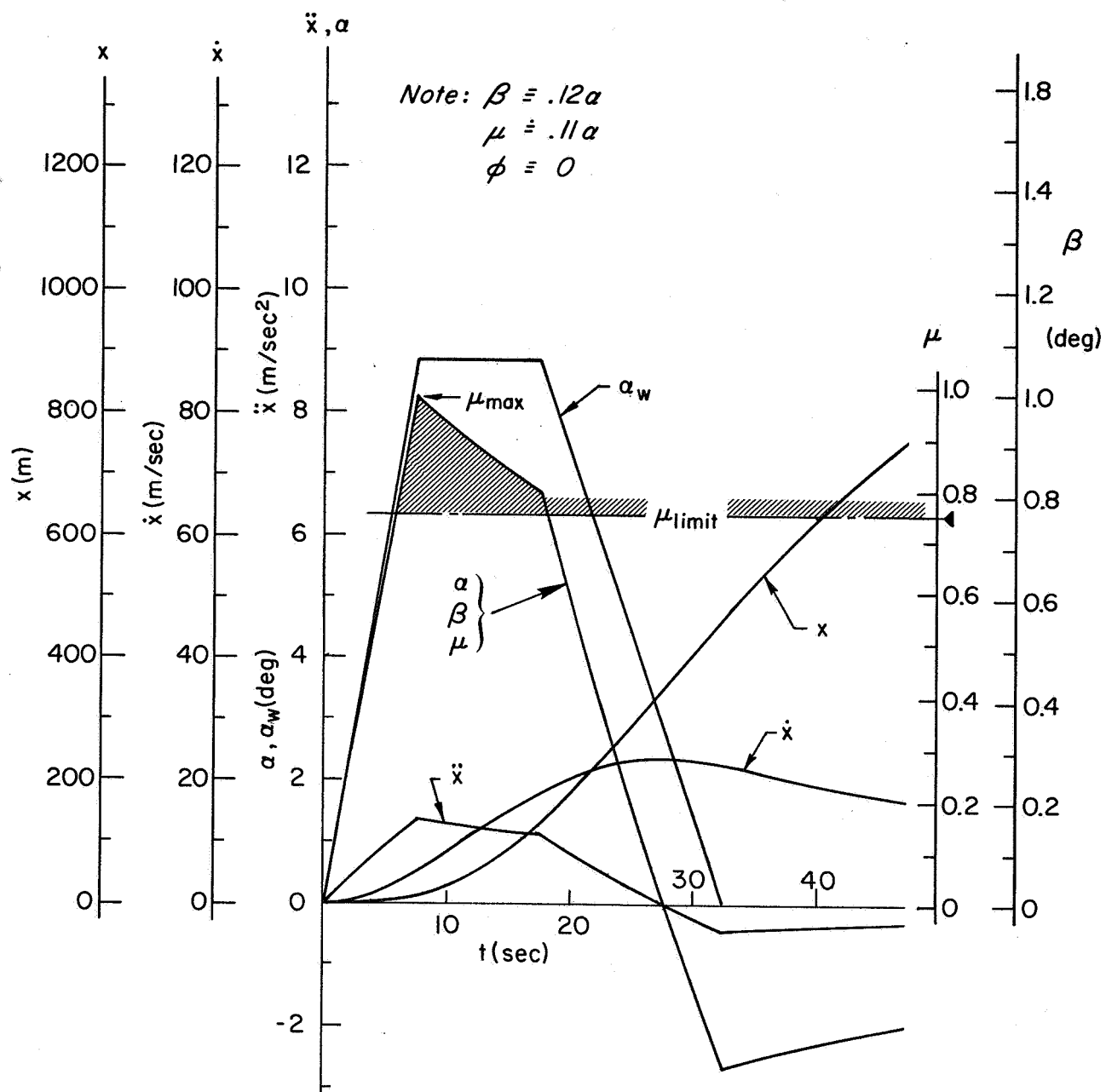
Figure 11. Time Response through Wind Spike
With Constant Attitude Control; $\Delta\varphi \equiv 0$

79
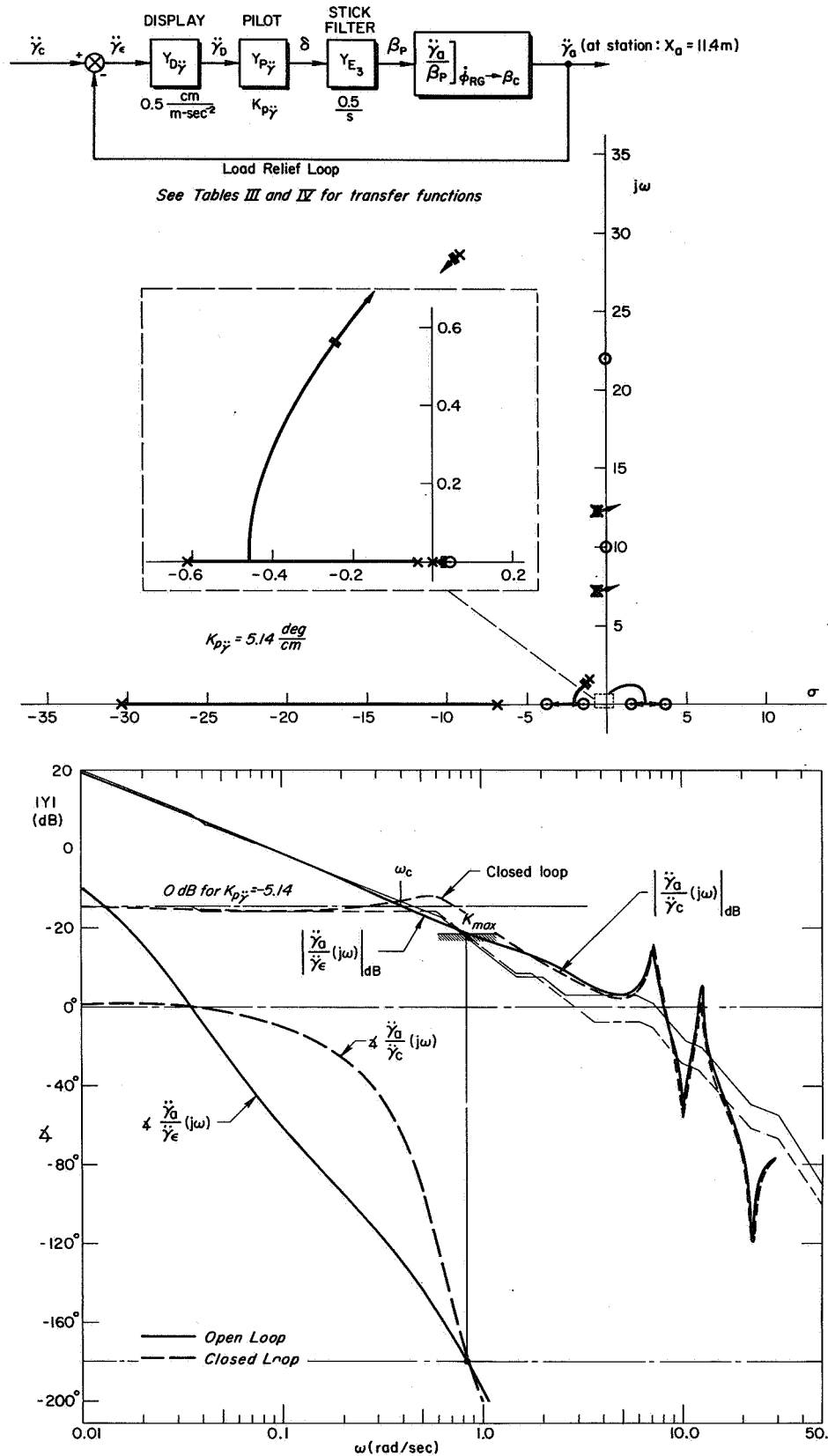
Figure 12. System Survey for Piloted Load Relief Loop

80
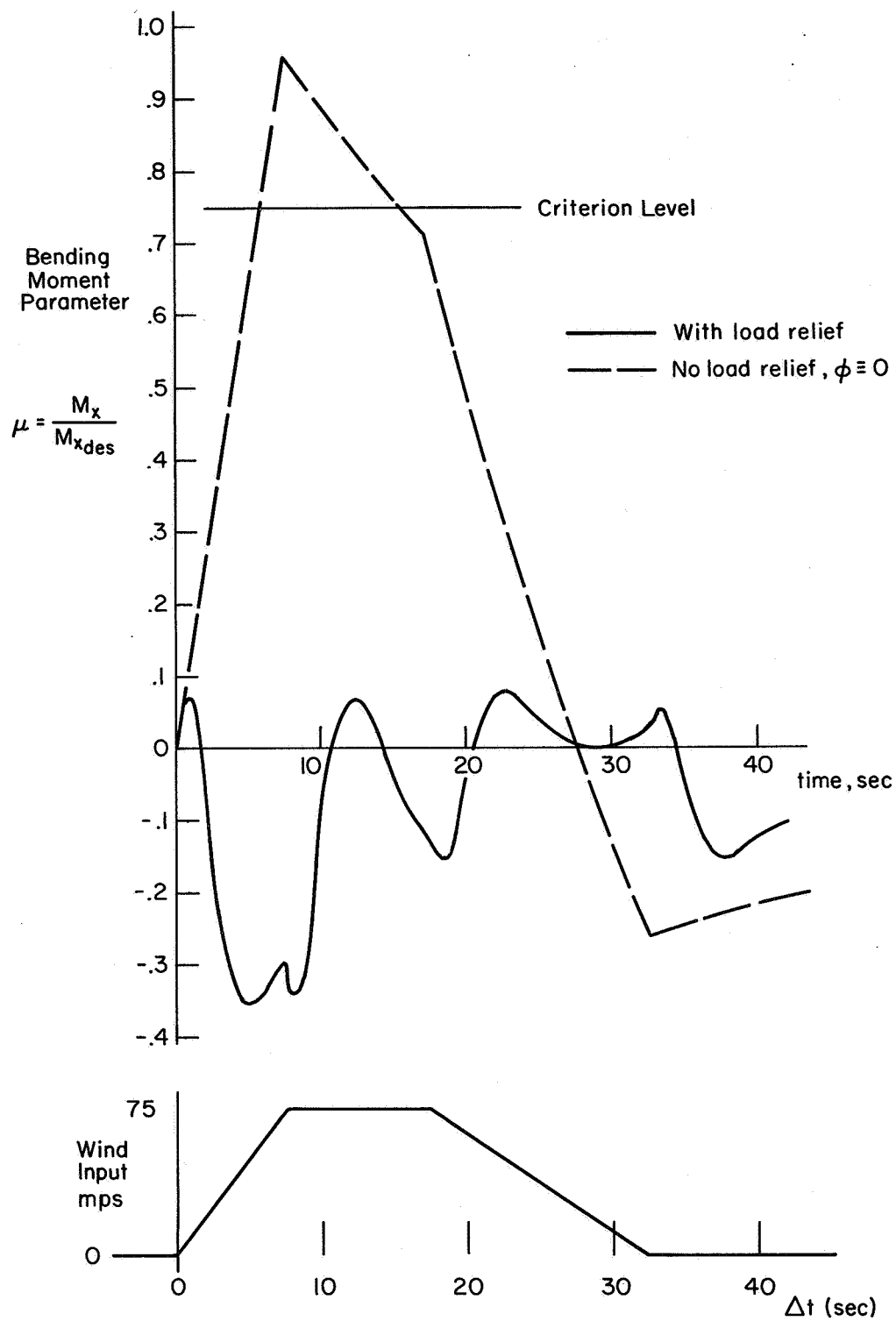
Figure 13. Time Response of Bending Moment Parameter
with $\varphi \equiv 0$ and with Load Relief Loop Closed

81
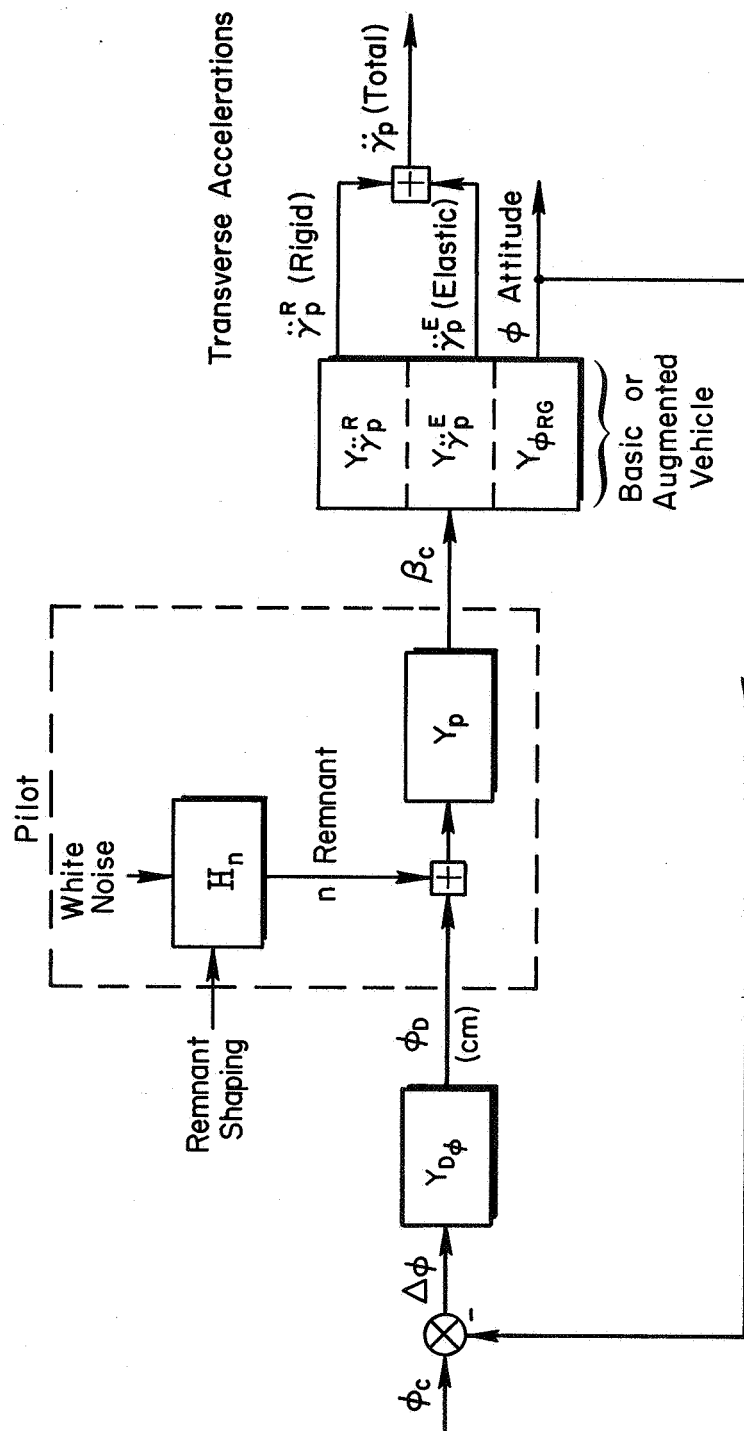
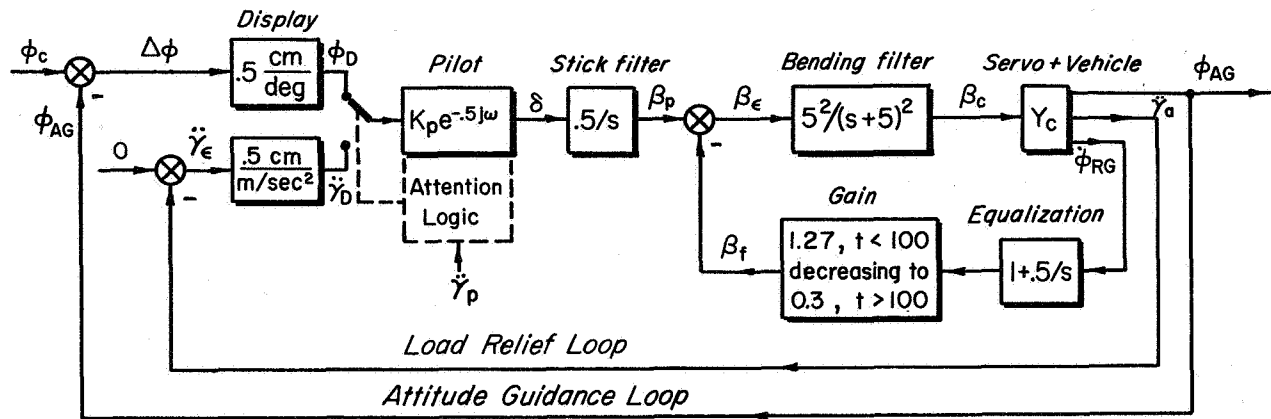Figure 14. Block Diagram for Analysis of Pilot's Remnant Effects
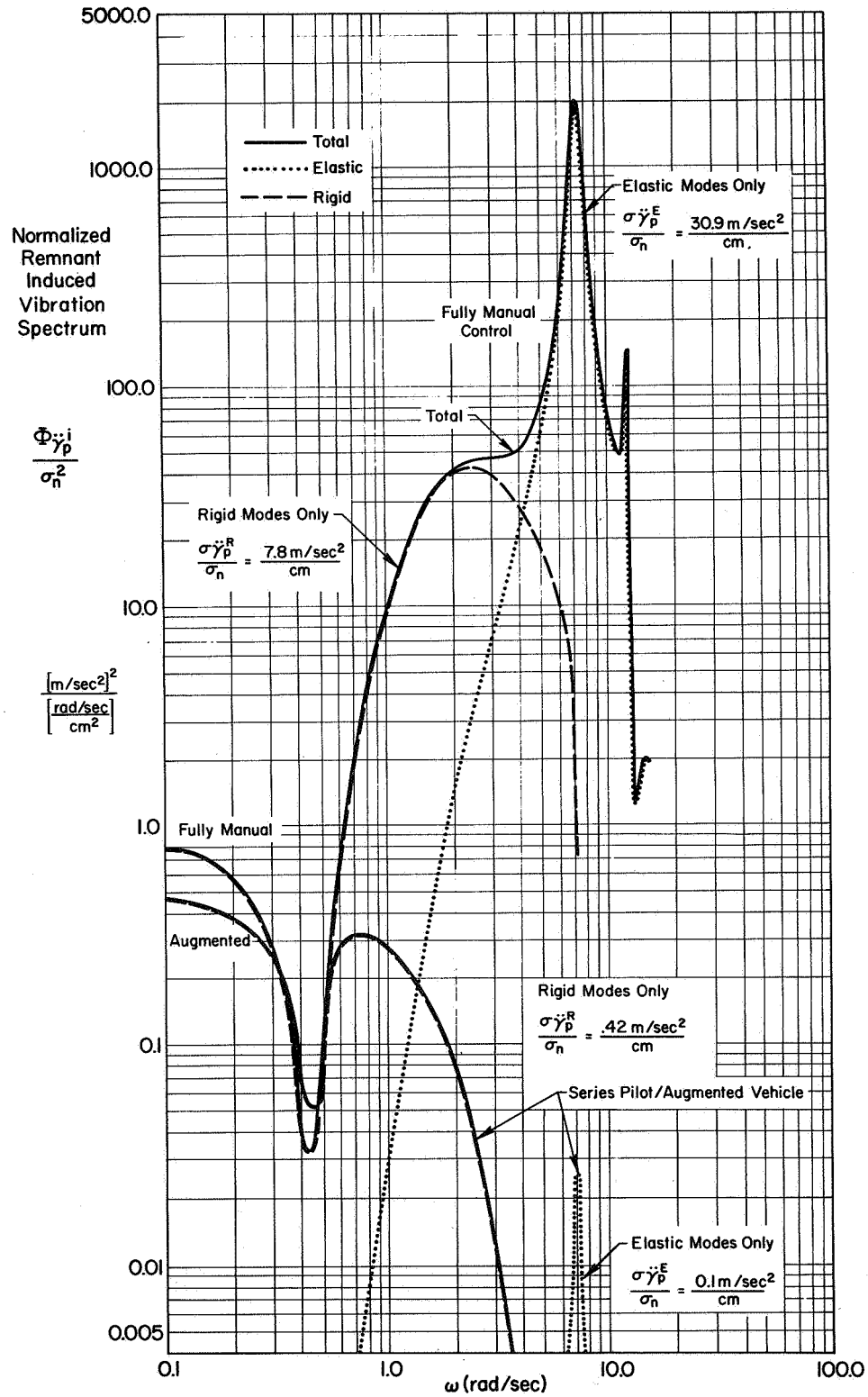
Figure 15. Vibration Spectrum Due to Remnant

Figure 16. Final Configuration of the Augmented Manual Control System
for the First-Stage Saturn V Booster

84

REFERENCES

1. Holleman, E. C.; Armstrong, N. A.; and Andrews, W. H.: Utilization of the Pilot in the Launch and Injection of a Multistage Orbital Vehicle. Paper 60-16, Inst. of Aeron. Sci., Jan. 1960.

2. Muckler, F. A.; Hookway, R. O.; and Burke, H. H.: Manned Control of Large Space Boosters. Trans. Seventh Symp. on Ballistic Missile and Space Technology, vol. II, Space Systems Div., AF Systems Command, Los Angeles, 1962.

3. Muckler, F. A.; and Obermayer, R. W.: The Use of Man in Booster Guidance and Control. NASA CR-81, July 1964. (Also available as AIAA Paper 63-312, Aug. 1963.)

4. Wood, J. W.: Pilot Control of the X-20/Titan III Boost Profile. Seventh Annual Symp., Proc. of the 1963 "Report to the Aerospace Profession," Soc. Exper. Test Pilots, Lancaster, Calif., Sept. 1963.

5. Rogers, R. L.; and Hoey, R. G.: Pilot Control During Boost. Air Force Flight Test Center, Edwards AFB, Calif., Mar. 1963. (Vol. V, ASD-TDR-63-148, Proc. of 1962 X-20A (Dyna-Soar) Symp., Bioastronautics, pp. V-10-3-1 — V-10-3-21. Report confidential, paper unclassified.)

6. Hookway, R.; and Solov, E.: Manual Guidance of Large Space Boosters. IEEE Proc. of MIL-E-CON, Feb. 1964.

7. Ashkenas, I. L.; and McRuer, D. T.: A Theory of Handling Qualities Derived from Pilot—Vehicle System Considerations. Aerospace Eng., vol. 21, no. 2, Feb. 1962, pp. 60, 61, 83—102.

8. McRuer, D. T.; and Graham, D.: Pilot—Vehicle Control System Analysis. Paper 63-310, Amer. Inst. Aeron. and Astronaut., Aug. 1963.

9. Ashkenas, I. L.; and McRuer, D. T.: Competing Flight Control Systems for Entry Glider Lateral Control. Tech. Rept. 107-1 (ASD-TDR-62-699, DDC AD-432190), Systems Technology, Inc., Feb. 1964.

10. Stapleford, R. L.; and Jex, H. R.: A Study of Manual and Automatic Control Systems for the Terminal Phase of Orbital Rendezvous. Tech. Rept. 13 (ASD-TR-62-82, ASTIA AD285528), Systems Technology, Inc., June 1962.

11. Stapleford, R. L.; Johnston, D. E.; Teper, G. L.; and Weir, D. H.: Development of Satisfactory Lateral—Directional Handling Qualities in the Landing Approach. NASA CR-239, July 1965.

12. Lester, H. C.; and Morgan, H. G.: Determination of Launch-Vehicle Response to Detailed Wind Profiles. Preprint 64-82, Amer. Inst. Aeron. and Astronaut., Jan. 1964.

13. Parks, D. L.; and Snyder, F. W.: Human Reaction to Low Frequency Vibration. Rept. D3-3512-1, The Boeing Co., Wichita, July 24, 1961.

14. Cooper, G. E.: Understanding and Interpreting Pilot Opinion. Aeronaut. Eng. Rev., vol. 16, no. 3, Mar. 1957, pp. 47−52.

15. McRuer, Duane; Graham, Dunstan; Krendel, Ezra; and Reisener, William, Jr.: Human Pilot Dynamics in Compensatory Systems—Theory, Models, and Experiments with Controlled Element and Forcing Function Variables. Tech. Rept. 115-1 (AFFDL-TR-65-15), Systems Technology, Inc., Jan. 1965.

16. McRuer, D. T.; and Krendel, E. S.: Dynamic Response of Human Operators. Contracts AF33(616)-3080 and AF33(616)-2804 (WADC-TR-56-524, ASTIA AD-110693), Control Specialists, Inc., and The Franklin Institute, Oct. 1957.

17. Elkind, J. E.: Characteristics of Simple Manual Control Systems. Tech. Rept. 111, Lincoln Lab., Mass. Inst. of Tech., Apr. 1956.

18. Wierwille, W. W.; and Gagne, G. A.: A Theory for the Optimal Deterministic Characterization of the Time-Varying Dynamics of the Human Operator. NASA CR-170, Feb. 1965.

19. McDonnell, J. D.: A Preliminary Study of Human Operator Behavior Following a Step Change in the Controlled Element. IEEE Trans., vol. HFE-7, no. 3, Sept. 1966, pp. 125−128.

20. McRuer, D. T.: Unified Analysis of Linear Feedback Systems. Tech. Rept. 14 (ASD-TR-61-118, ASTIA AD270593), Systems Technology, Inc., July 1961.

21. McRuer, D. T.; and Stapleford, R. L.: Sensitivity and Modal Response for Single-Loop and Multiloop Systems. Tech. Rept. 123-3 (ASD-TDR-62-812, ASTIA AD-298267), Systems Technology, Inc., Jan. 1963.

22. McRuer, D. T.; Ashkenas, I. L.; and Pass, H. R.: Analysis of Multiloop Vehicular Control Systems. Tech. Rept. 123-1 (ASD-TDR-62-1014, ASTIA AD-434799), Systems Technology, Inc., Mar. 1964.

23. Jex, H. R.; and Cromwell, C. H.: Theoretical and Experimental Investigation of Some New Longitudinal Handling Quality Parameters. Tech. Rept. 16 (ASD-TR-61-26, ASTIA AD-282879), Systems Technology, Inc., Mar. 1961.

24. Durand, T. S.; and Jex, H. R.: Handling Qualities in Single-Loop Roll Tracking Tasks: Theory and Simulator Experiments. Tech. Rept. 120-1 (ASD-TDR-62-507, ASTIA AD-293236), Systems Technology, Inc., Nov. 1962.

25. McRuer, D. T.; Ashkenas, I. L.; and Guerre, C. L.: A Systems Analysis View of Longitudinal Flying Qualities. Tech. Rept. 6 (WADD-TR-60-43, OTS PB-171551), Systems Technology, Inc., Jan. 1960.

26. Ashkenas, I. L.: A Study of Conventional Airplane Handling Qualities
    Requirements. Pt. I. Roll Handling Qualities. Tech. Rept. 133-2
    (AFFDL-TR-65-138I, ASTIA AD-627659), Systems Technology, Inc.,
    May 1965.

27. Seckel, E.; Hall, I. A. M.; McRuer, D. T.; and Weir, D. H.: Human Pilot
    Dynamic Response in Flight and Simulator. Contracts AF 33(616)-3080
    and AF 33(616)-2506 (WADC-TR-57-520, ASTIA AD-130988), Princeton
    Univ. and Control Specialists, Inc., Aug. 1958.

28. Hall, I. A. M.: Effects of Controlled Element on the Human Pilot.
    Contract AF 33(616)-2506 (WADC-TR-57-509, ASTIA AD-130979), Princeton
    Univ., Aug. 1958.

29. Todosiev, E. P.; Rose, R. E.; Bekey, G. A.; and Williams, H. L.: Human
    Tracking Performance in Uncoupled and Coupled Two-Axis Systems.
    Rept. 4380-6003-R000 (Contract NAS1-4419), TRW Systems, 8 Dec. 1965.

30. Levison, W. H.; and Elkind, J. I.: Studies of Multi-Variable Manual
    Control Systems: Two Axis Compensatory Systems with Compatible
    Integrated Display and Control. NASA CR-554, Aug. 1966.

31. Dander, V. A.: Predicting Pilot Ratings of Multi-Axis Control Tasks from
    Single-Axis Data. IEEE Trans., vol. HFE-4, no. 1, Sept. 1963,
    pp. 15−17.

32. McRuer, D. T.; and Ashkenas, I. L.: Design Implications of the Human
    Transfer Function. Paper 62-188, Inst. of Aeron. Sci., Aug. 1962.
    (Also available in Aerospace Eng., vol. 21, no. 9, Sept. 1962.)

33. Stapleford, R. L.; Hofmann, L. G.; Best, J. J.; Wezeman, C. D.; and
    Johnson, W. A.: Transfer Function Approximations for Large Highly
    Coupled Elastic Boosters with Fuel Slosh. NASA CR-464, Apr. 1966.

34. Hardy, G. H.; West, J. V.; and Gunderson, R. W.: Evaluation of Pilot's
    Ability to Stabilize a Flexible Launch Vehicle During First-Stage
    Boost. NASA TN D-2807, May 1965.

35. Sissenwine, N.; and Kasten, H. G.: Proceedings of the National Symposium
    on Winds for Aerospace Vehicle Design, AFCRL-62-273, vols. I and II,
    Mar. 1962.

36. Lester, H. C.; and Tolefson, H. B.: A Study of Launch-Vehicle Responses
    to Detailed Characteristics of the Wind Profile. Paper presented at
    5th Conf. on Applied Meteorology, Atmospheric Problems of Aerospace
    Vehicles, Amer. Meteorological Soc. (Atlantic City, N. J.), Mar. 1964.

37. Hoelker, R. F.: Theory of Artificial Stabilization of Missiles and Space
    Vehicles with Exposition of Four Control Principles, NASA TN D-555,
    June 1961.

38. Klenk, W. J.: An Adaptive System for Load Relief and Accurate Control
    of Launch Vehicles. Paper 64-239, Amer. Inst. Aeron. and Astronaut.,
    June 1964.

39. Burke, H. H.: Aerodynamic Load Reduction Techniques for Large Elastic Launch Vehicles. IEEE Trans., vol. AC-9, no. 4, Oct. 1964.

40. Stinson, J. R.; Weinstein, A. Y.; and Reiter, E. R.: Details of Wind Structure from High Resolution Balloon Soundings. Rept. 65-123A, Meteorology Research, Inc., 1964.

41. Halfman, R. L.: Dynamics. Vol. II. Addison-Wesley Pub. Co., Inc., 1962.

42. James, H. M.; Nichols, N. B.; and Phillips, R. S.: Theory of Servo-mechanisms. McGraw-Hill Book Co., Inc., 1947.

43. McDonnell, J. D.; and Jex, H. R.: A "Critical" Tracking Task for Man-Machine Research Related to the Operator's Effective Delay Time—Part II. Experimental Effects of System Input Spectra, Control Stick Stiffness, and Controlled Element Order. NASA CR 674, Jan. 1967.

44. Wasicko, Richard J.; and Magdaleno, Raymond E.: Effects of Nonlineari-ties on Human Operator Tracking Performance, A Review of the Litera-ture. AMRL-TR-65-158, Oct. 1965.

45. Graham, Dunstan, "Effect of Some Control System Nonlinearities on Single-Loop Compensatory Tracking," Third Annual NASA-University Conference on Manual Control, NASA SP-144, March 1-3, 1967, pp. 215 - 221.

46. McRuer, D. T.; and Magdaleno, R. E.: Human Pilot Dynamics with Various Manipulators. AFFDL-TR-66-138, Dec. 1966.

47. Magdaleno, R. E.; and McRuer, D. T.: Effects of Manipulator Restraints on Human Operator Performance. AFFDL-TR-66-72, Dec. 1966.

48. Sadoff, Melvin: Effects of High Sustained Acceleration on Pilots' Performance and Dynamic Response. NASA TN D-2067, July 1964.

49. Weisz, A. Z.; Allen, R. W.; and Goddard, C. J.: An Evaluation of Three Types of Hand Controllers Under Random Vertical Vibration. Proceed-ings of MIT-NASA Working Conference on Manual Control, Feb. 28 — Mar. 2, 1966.

50. Teper, G. L.; and Jex, H. R.: Synthesis of Manned Booster Control Systems using Mathematical Pilot Models. Sixth Annual Symposium of the Professional Group on Human Factors in Electronics, May 6-8, 1965.

APPENDIX A

SYNOPSIS OF USAM TECHNIQUES

The Unified Servo Analysis Method (USAM) is an eclectic approach
to feedback systems analysis which uses a variety of techniques in a
coordinated fashion. The many individual techniques and schemes involved
are individually treated and integrated in great detail in Refs. 20-22,
so only a cursory review of those having particular application to
booster control analysis will be covered here. To make this brief
exposure both concrete and pertinent, an equalized attitude loop,
closed about the aerodynamically unstable flexible booster, will be
used as an example (Fig. A-1). The controller parameters were based
on the factors given previously in Section VI.

Each of the techniques involved in USAM are well-known approaches
to the basic analysis problem of feedback systems: i.e., "Given the
open-loop system parameters, what are the closed-loop characteristics?"
Each individual technique is best at providing certain limited informa-
tion about the closed-loop system in an especially clear, simple, and
straightforward manner. The selected techniques are supplementary in
that the limited information best shown by each tends to emphasize
different properties of the system. When taken together, i.e., when
"unified," the composite readily provides a complete picture of the
system characteristics as a correlated whole, which enhances physical
appreciation and helps to simplify and increase understanding of the
synthesis process.

As a beginning consider the **gain-phase plot** of Fig. A-2. This type
of diagram is perhaps the most commonly used in booster controls analysis.
The obvious information displayed (and labeled) in Fig. A-2 is the gain
and phase margins. (The commonly used term "gain stabilized" and/or
"phase stabilized" originated from this view of the stability situation.)
In addition, detailed information on the closed-loop transfer function is
obtainable by superimposing Fig. A-2 over the conventional Nichols grid
(Ref. 42). One example of the combined use of gain-phase, and Bode
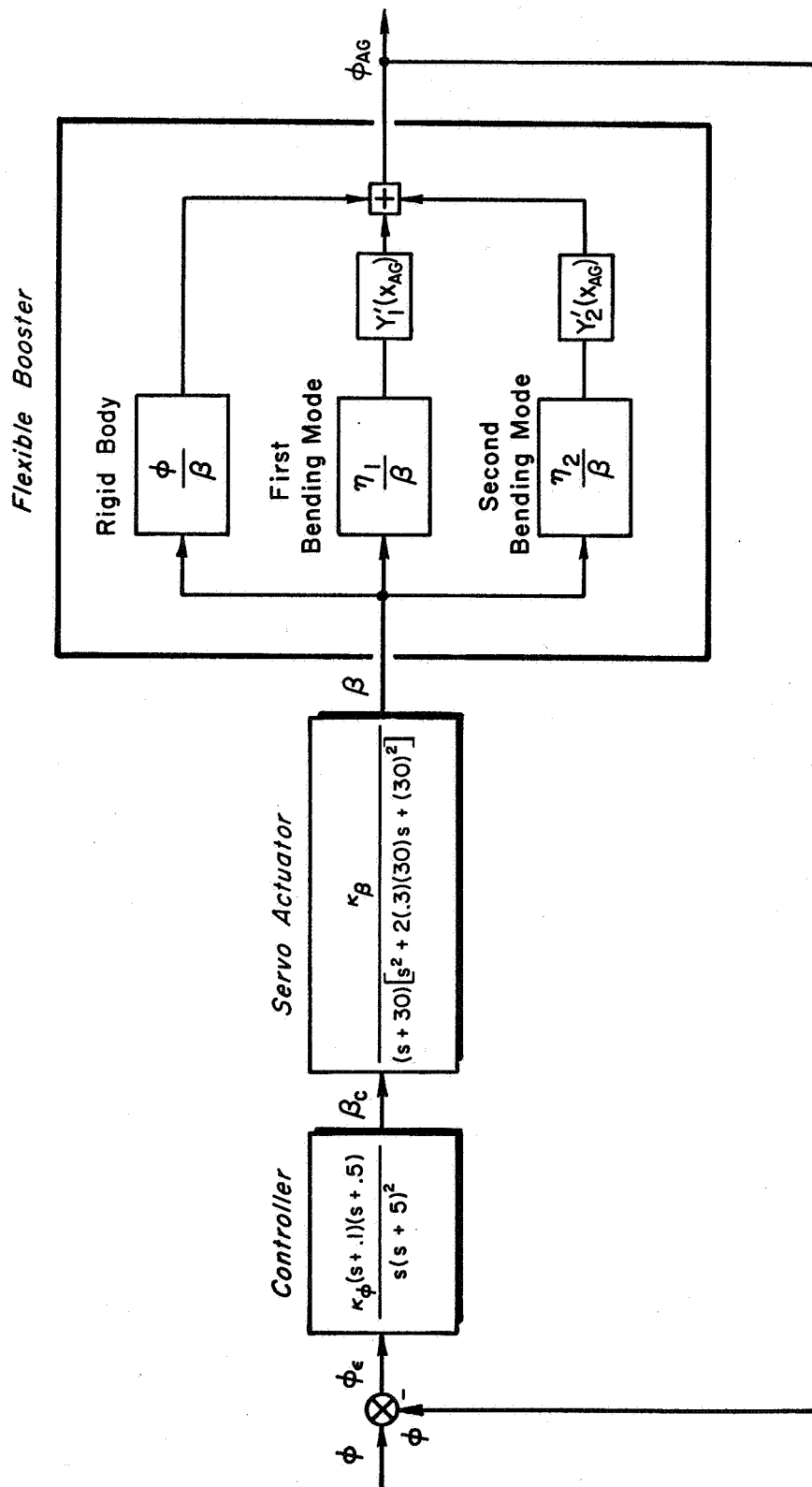
$Y'_{1,2}(x_{AG})$ – Normalized bending mode slopes at attitude gyro location

ϕ_{AG} – Rigid body plus elastic inputs to gyro
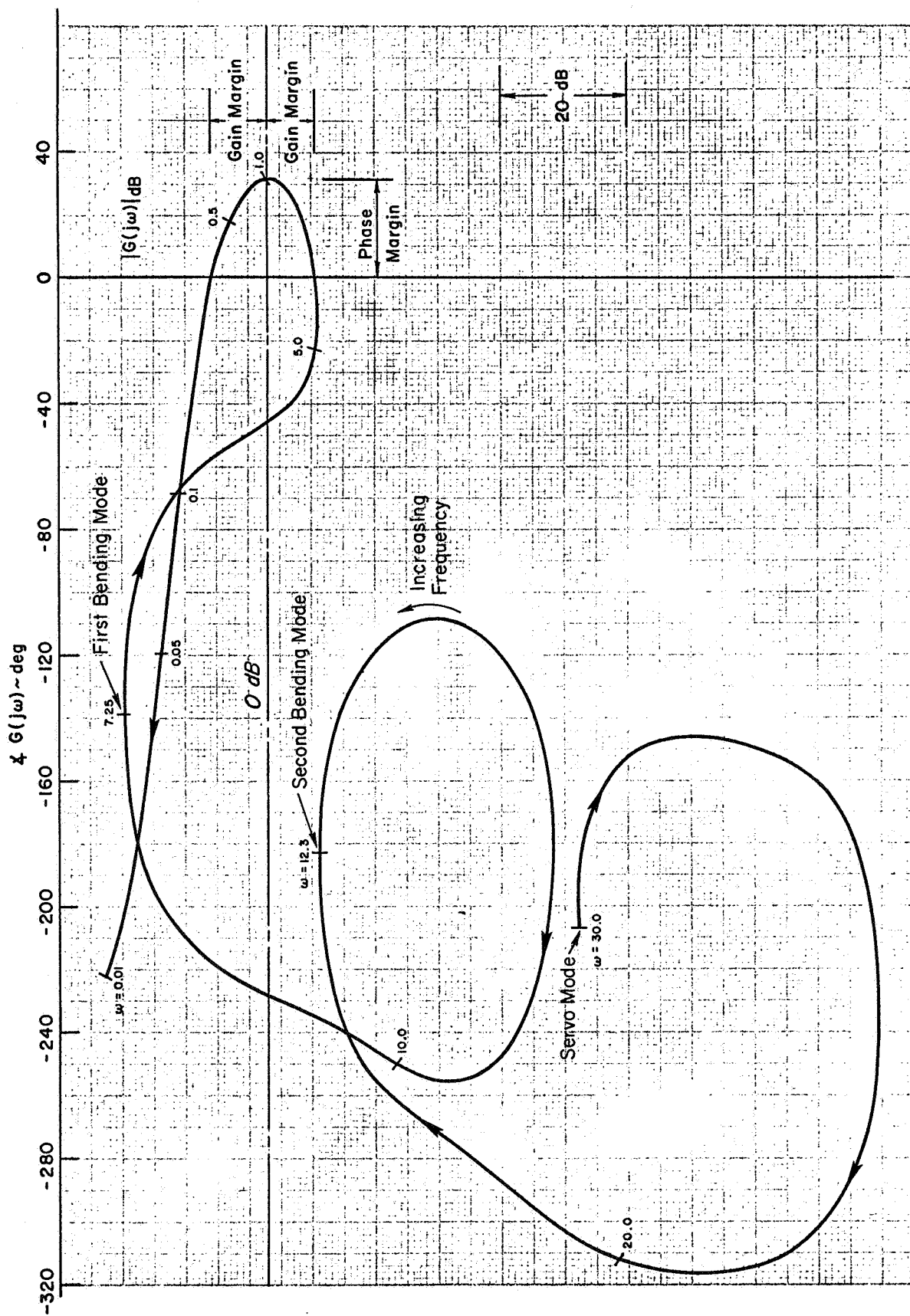
Figure A-1. System Block Diagram

A-2

Figure A-2. Gain-Phase Plot

diagrams is to find the closed-loop damping ratio, ζ, of one pair of roots of a complicated array given the open-loop transfer function. The value of ζ can be found from the Bode plot amplitude ratio departure from its asymptote break-point (converted from dB to magnitude ratio) which is given by $1/2\zeta$. The closed-loop magnitude read from the Nichols grid over the corresponding frequency on the gain-phase plot can then be plotted on the Bode plot and the above relation used to solve for ζ. Other applications of this particular set of graphical aids to servoanalysis are well known and will not be further belabored.

The majority of USAM system analyses make combined use of generalized **Bode diagrams** and the **root locus** diagram. Figure A-3 contains a root locus and three types of Bode diagrams for the example system of Fig. A-1. Some of the more pertinent features of each diagram are discussed below.

1. Figure A-3a is the conventional **root locus plot**, where the complex number eigen values (roots) of the closed-loop characteristic equation are plotted on the $s = \sigma \pm j\omega$ plane for increasing levels of an open-loop parameter, usually gain. Provided the various gain values are indicated on each branch of the loci, a very helpful picture of the changing closed-loop dynamic modes is given. Since the real part gives the total damping in each mode, the points of neutral stability are readily apparent (e.g., Points "a" and "b" on Branch ⑧ show the conditional stability of this system. Point "a" indicates where, for increasing gain, the system becomes stable; it remains so, as gain is increased further, until Point "b" where it will again become unstable. The root locus is particularly suited to picturing the transient dynamics because the modes and modal response coefficients can be directly seen as the locations and distances between the corresponding poles and zeros (see Ref. 21 for a more complete discussion on this point). Disadvantages of the root locus include: its linear scale, which requires multiple plots for a wide-frequency problem such as this, and its lack of clear information on closed-loop tracking accuracy, bandwidth, etc.

2. Figure A-3b is a the conventional $j\omega$-Bode plot, which is equivalent to the frequency response plot, for stable systems. Neutral stability frequencies and gains are readily apparent from this representation of the transfer function. The two frequencies a and b definitely establish the stability region for the system. A 0-dB line through Point "a" (line A-A) is the minimum gain; that through Point "b" (line B-B) the maximum. As
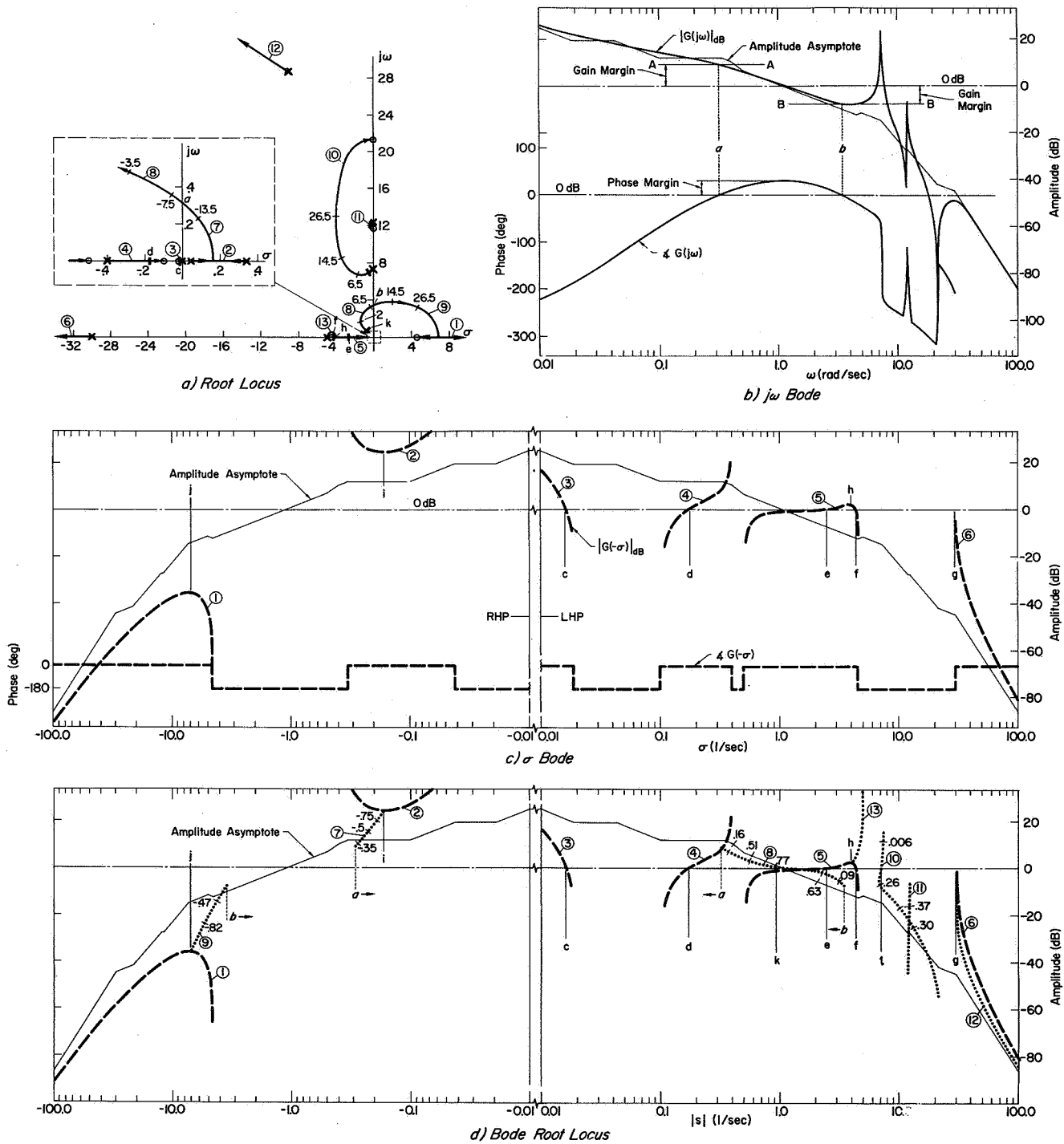
Figure A-3. Unified Servo Analysis Diagrams

A-5

indicated in the figure, the gain and phase margins
for any other open-loop 0-dB line are easily found.
The gain-phase plot considered above is derived
directly from the conventional Bode, so the correla-
tions between the two forms are readily apparent.

One of the most useful properties of a Bode presentation
is its clear indication of which open-loop poles and zeros
have the most influence on the closed-loop characteristics.
This comes about because, on the Bode plot, it is readily
apparent in what frequency regions $|G(j\omega)| \gg 1$ or $|G(j\omega)| \ll 1$.
In those regions for which $|G(j\omega)| \gg 1$, $G/(1+G) \doteq 1$; i.e.,
the closed-loop poles are nearly equal to open-loop zeros.
Consequently, variations in the open-loop poles have little
effect, whereas variations in open-loop zeros have a large
effect, on the closed-loop characteristics. Opposite
effects occur in regions for which $|G(j\omega)| \ll 1$, $G/(1+G) \doteq G$,
where the closed-loop poles are nearly equal to the open-loop
poles.

3. The Sigma Bode, "Siggy", diagram (Fig. A-3c) is a plot of
the amplitude and phase of $G(s)$ for values of $s = -\sigma$ along
the <u>real</u> axis. The phase of a Siggy diagram is either 0 or
180 deg, corresponding to a plus or minus value of the
characteristic equation. The asymptotes for the magnitudes
are identical to those for the conventional Bode, and the
departure of the actual magnitude from these asymptotes
about a given break frequency is symmetric on a log plot,
similar to that for the conventional Bode plot. The Siggy
is usually plotted with $s = -\sigma$ to put the interesting left-
half plane real roots onto a right-hand log plot, and permit
constructing the Siggy plot on the $j\omega$-Bode asymptotes. The
departures for real poles and zeros becomes infinite at their
break point. The Siggy plot clearly illustrates the variations
of the closed-loop real roots with gain. Consistent with the
0 deg stability criteria being used in the example, the 0 deg
Siggys are shown in Fig. A-3c. Then, over all "frequency"
(σ) regions where $G(-\sigma)$ is zero, the requirement for a
closed-loop root is $|G(-\sigma)| = 1$, or equivalently, $|G(-\sigma)|_{dB} = 0$.
Consequently, for the 0-dB line, Points "c", "d", "e", "f",
and "g" are the intersections of the 0-dB line and the Siggy
curve, and thus are the <u>real closed-loop poles</u>. Points "h",
"i", and "j" are significant as being those which indicate
the gains for and frequencies of two identical real roots
(root locus breakaway).

4. The **Bode root locus** is shown in Fig. A-3d. It is a plot
of the magnitude of $G(s)$ for all values of s on the root
locus. It can be seen that the Siggy is part of the Bode
root locus, as it represents those branches of the locus
which lie along the real axis. The points where the locus
crosses the imaginary axis (Points "a" and "b") can be

brought down from the conventional Bode. The remaining portion of the Bode root locus can be found in a number of ways — by "decomposition" using the Siggy and the conventional jω Bode, by mapping for a complete root locus, by direct calculation, etc. Once the Bode root locus diagram has been obtained, <u>all</u> the closed-loop roots can easily be observed at the intersections of the 0-dB line and Bode root locus. Points "k" and "l" in Fig. A-3d locate two pairs of complex-conjugate closed-loop roots. The correspondence between the conventional root locus and the Bode root locus can be seen by comparing Figs. A-3a and A-3d. Identical points are indicated by the small letters, identical branches by the circled numbers. Gain is the parameter along the conventional root locus (in Fig. A-3a it is given in dB); damping ratio, ζ, varies along the Bode root locus (as indicated in Fig. A-3d).

This example of combined use of gain-phase, root locus, and the jω, σ, and generalized Bode is sufficient to illustrate the power of the unified analysis technique. The complementary advantages of the individual plots and the tendency to offset the shortcomings of one another are especially helpful in iterative synthesis procedures because they provide several correlated, yet different, sources of insight, understanding, and physical appreciation.

Another aspect of the Unified Servo Analysis Method is the consideration of the sensitivity of closed-loop system characteristics to open-loop parameter variations. The most direct and simplest way of qualitatively approaching this problem has been touched on above. When quantitative answers are required, however, a more sophisticated approach is desirable, yet one which still can make use of the techniques and methods already described. This is accomplished by the sensitivity analysis features of USAM.

As used here, sensitivity is defined as the partial derivative of a system root with respect to some open-loop parameter. The main advantage of sensitivities is to provide a relatively simple method for assessing the variations in

1. Closed-loop poles due to variations in the open-loop transfer function gains, zeros, or poles;

A-7

2. Open-loop transfer function poles and zeros
   due to **any** parameter;

3. Closed-loop poles due to any parameter
   (combining 1 and 2).

The total effects on closed-loop poles of variations in several parameters
are obtained by summing appropriate products of sensitivities and parameter
variations.

The development of the pertinent sensitivity relationships and the
methods of computing sensitivities constitute a sizable report, and a
complete development is given in Ref. 21. Although the general deriva-
tions are rather messy, after one is familiar with the methods the calcu-
lation of sensitivities is relatively straightforward even for complicated
multiloop systems. To give some feeling for what is involved, the varia-
tion in a closed-loop pole, dq_i, for a single-loop closure can be
expressed as

$$dq_i = S_\kappa^i \frac{d\kappa}{\kappa} + S_{z_j}^i dz_j + S_{p_j}^i dp_j \qquad (A-1)$$

where κ is the open-loop gain, z_j an open-loop zero, and p_j an open-loop pole.
The sensitivities themselves are given by

$$S_\kappa^i = \frac{\partial q_i}{\partial \kappa / \kappa} = \frac{1}{(\partial G/\partial s)_{s=q_i}}$$

$$S_{z_j}^i = \frac{\partial q_i}{\partial z_j} = \frac{S_\kappa^i}{q_i + z_j} \qquad (A-2)$$

$$S_{p_j}^i = \frac{\partial q_i}{\partial p_j} = \frac{-S_\kappa^i}{q_i + p_j}$$

Corresponding relationships for multiple-loop closures are given in Ref. 21.
The general importance of the gain sensitivity, S_κ^i, as a common factor in
all the sensitivities is indicated in Eqs. A-2. Gain sensitivity can be
evaluated directly from most of the plots already shown in Fig. A-3, as
it is essentially the slope of a root locus branch evaluated at a closed-

loop root. The closed-loop poles, q_j, are also present on these plots, so the zero sensitivity, $S_{z_j}^i$, and pole sensitivity, $S_{p_j}^i$, can also be found from information presented there. The sensitivities can also be computed directly using other techniques.

In general, the sensitivities will be complex numbers, or vectors in the s-plane, which indicate directly the changes in the damping and frequency of a root due to variations in an open-loop parameter. To give more substance to the notion, the sensitivities of the closed-loop roots of the booster control system of Fig. A-1 to variations in bending mode parameters were computed. The most sensitive parameter was found to be the slope of the first bending mode at the gyro location; and the corresponding sensitivities of the closed-loop roots most affected are given in Table A-I. The table also shows the changes due to 10 percent and 20 percent reductions in the slope as predicted by sensitivities compared with the actual changes (obtained by factorization). On the whole, the sensitivities represent the complete influences quite well.

The power and efficiency of the USAM methods is even more apparent when analyzing multiloop systems such as those investigated in Ref. 22.

TABLE A-I

SENSITIVITY EXAMPLE

FIG. A-3 REF. POINT	Root (sec^{-1})	Sensitivity (sec^{-1})	ROOT CHANGES FOR REDUCED $Y_1'(x_G)$			
			10 Percent Reduction		20 Percent Reduction	
			Predicted (sec^{-1})	Actual (sec^{-1})	Predicted (sec^{-1})	Actual (sec^{-1})
k	$-0.70035 + j0.58448$	$-0.00783 - j0.1125$	$(0.078 + j1.125)10^{-2}$	$(0.118 + j1.145)10^{-2}$	$(0.157 + j2.25)10^{-2}$	$(0.323 + j2.324)10^{-2}$
e	-2.6922	-4.228	0.4228	0.3233	0.8456	0.5421
f	-4.3687	5.730	-0.5730	-0.4717	-1.1460	-0.8363
l	$-0.53100 + j6.9709$	$-0.590 - j0.433$	$0.0590 + j0.0433$	$0.0578 + j0.0427$	$0.1180 + j0.0866$	$0.1134 + j0.0841$

*This is the sensitivity to a fractional change in $Y_1'(x_G)$

APPENDIX B

SAWTOOTH BODE CONCEPT

The basic objective of the Sawtooth Bode Concept is to increase the damping of several modes simultaneously. To show how this can be done, some fundamental aspects of the tie between Bode amplitude plots and the root locus diagram will be illustrated using a sample concrete example. Consider the single-loop block diagram in Fig. B-1,
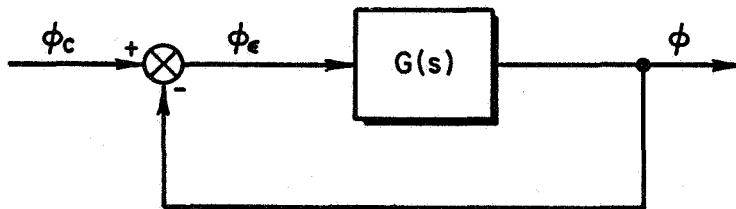

Figure B-1. Simple Unity-Feedback System

and assume $G(s)$ is of the form

$$G(s) = \frac{K(s^2 + 2\zeta_1\omega_1 s + \omega_1^2)}{s(s^2 + 2\zeta_2\omega_2 s + \omega_2^2)}$$

where ζ_1 and ζ_2 are both very low and $\omega_1 < \omega_2$. The root locus is shown in Fig. B-2, with indications of the closed-loop poles for three values of open-loop gain — low, K_L; medium, K_M; and high, K_H.
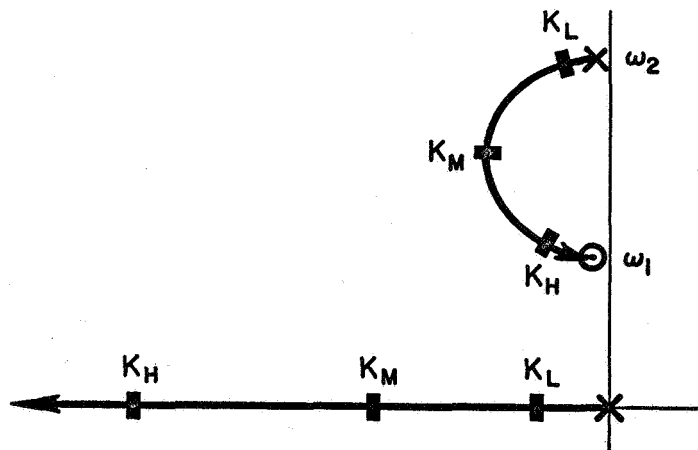
Figure B-2. Root Locus Diagram

The figure shows that maximum damping of the oscillatory closed-loop roots is achieved when the open-loop gain is K_M. If the open-loop gain is too low, the closed-loop oscillatory roots will be poorly damped, having a damping ratio only slightly higher than ζ_2. If the open-loop gain is too high, the closed-loop oscillatory roots will again be poorly damped, with a damping ratio approaching ζ_1.

Another important aspect of this simple case is revealed when the relative order of the complex pole and zero is reversed, i.e., $\omega_2 < \omega_1$. When this occurs the locus still proceeds from the pole to the zero in a counterclockwise direction, but may, enroute, pass out of the left half plane. Whether this actually takes place depends on the specific numerical values at hand, but the point is that a reversal in the pole-zero order gives rise to the possibility of instability. To avoid such possibilities the order of the quadratics should be zero-pole:zero-pole rather than pole-zero:pole-zero. This conclusion depends, of course, on the nature of the very low frequency characteristics (e.g., in the context of Fig. B-2 the free s in the denominator), and must be modified if these characteristics are changed significantly.

Now consider the open-loop Bode plot, with the 0 db lines shown for these three cases of gain, Fig. B-3. Comparison with the corresponding root locus case shows that when the 0 db line passes above or through the top of an open-loop Bode peak due to poorly damped denominator roots (poles), the closed-loop damping characteristics will be very poor. Also, when the 0 db line passes below or through the bottom of an open-loop Bode valley due to poorly damped numerator roots (zeros), the closed-loop damping again is very poor. The higher values of closed-loop damping occur when the 0 db line cuts deeply into the open-loop Bode peak, but well above the open-loop Bode valley.

The application of the above considerations in the synthesis of booster control systems where more complex open-loop transfer functions exist can now be shown fairly easily. Consider that the generalized single-loop block diagram shown in Fig. B-4 represents a booster control system. Here the response variable, q, is used as the feedback, the actuator servo is represented by a first-order element, and the controller is a pure gain with no
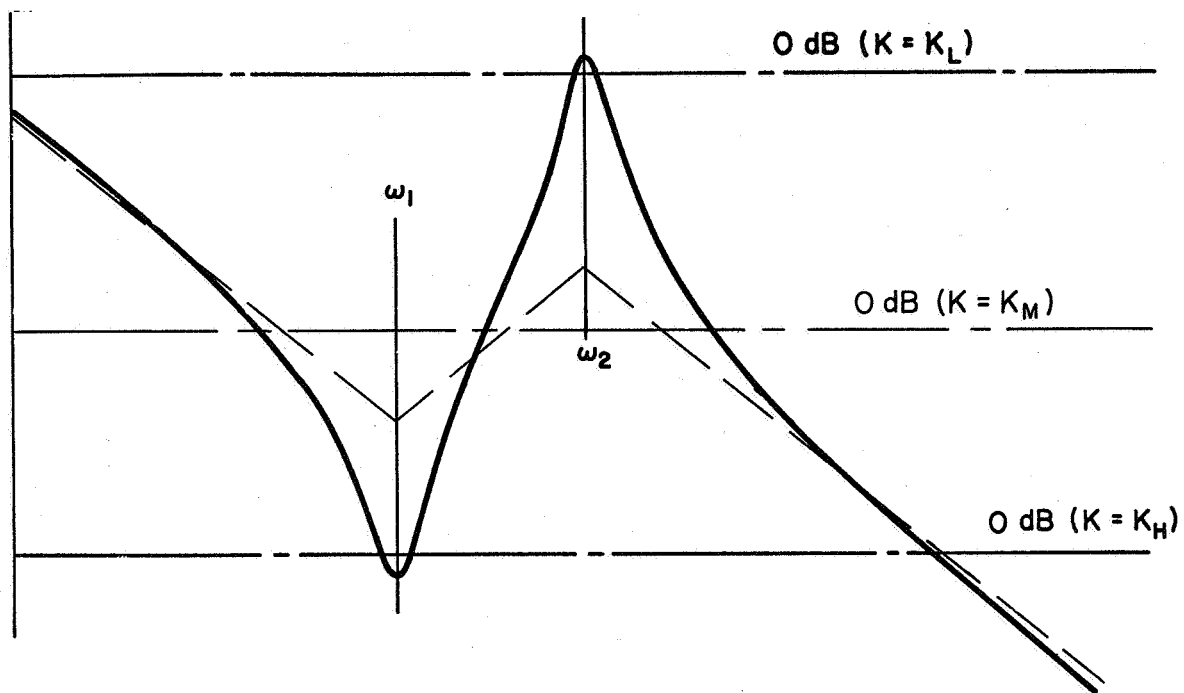
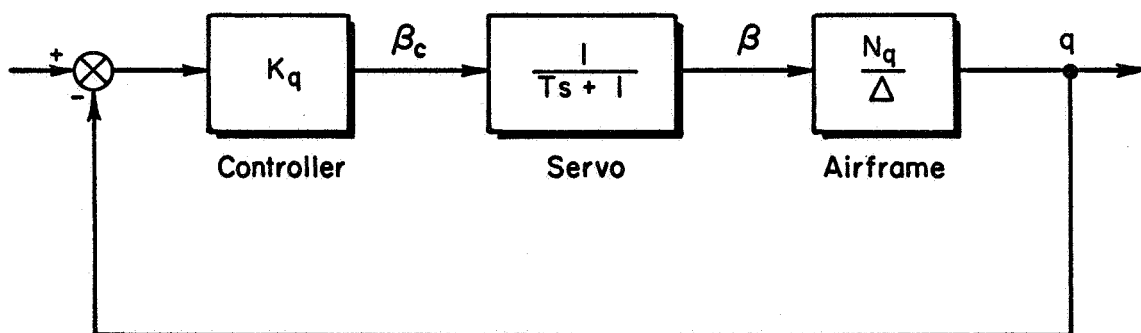Figure B-3. Open-Loop Amplitude Bode Plot

Figure B-4. Booster Control System Block Diagram

equalization. Also assume that the booster transfer function now is of the more complicated form

$$\frac{N_q}{\Delta} = \frac{A_q s (s^2 + 2\zeta_a \omega_a s + \omega_a^2)(s^2 + 2\zeta_b \omega_b s + \omega_b^2)}{(s^2 + 2\zeta_1 \omega_1 s + \omega_1^2)(s^2 + 2\zeta_2 \omega_2 s + \omega_2^2)(s^2 + 2\zeta_3 \omega_3 s + \omega_3^2)}$$

and that all the damping ratios (ζ) are very small. With the servo bandwidth high ($1/T > \omega_3$), a possible Bode plot for the controller-servo-booster open loop might appear as in Fig. B-5. In this case, closing the loop with a low gain is adequate to damp the first two modes, ω_1 and ω_2, but leaves the damping of the highest mode essentially unaffected. If the open-loop gain were increased to damp the ω_3 mode by having the 0 db line cut deeply into the Bode peak associated with ω_3, the closed-loop damping of the ω_2 mode would be substantially decreased, for the 0 db line now passes through the Bode valley of the poorly damped ω_a zeros. Thus, simultaneous damping of all three airframe oscillatory modes is not possible.
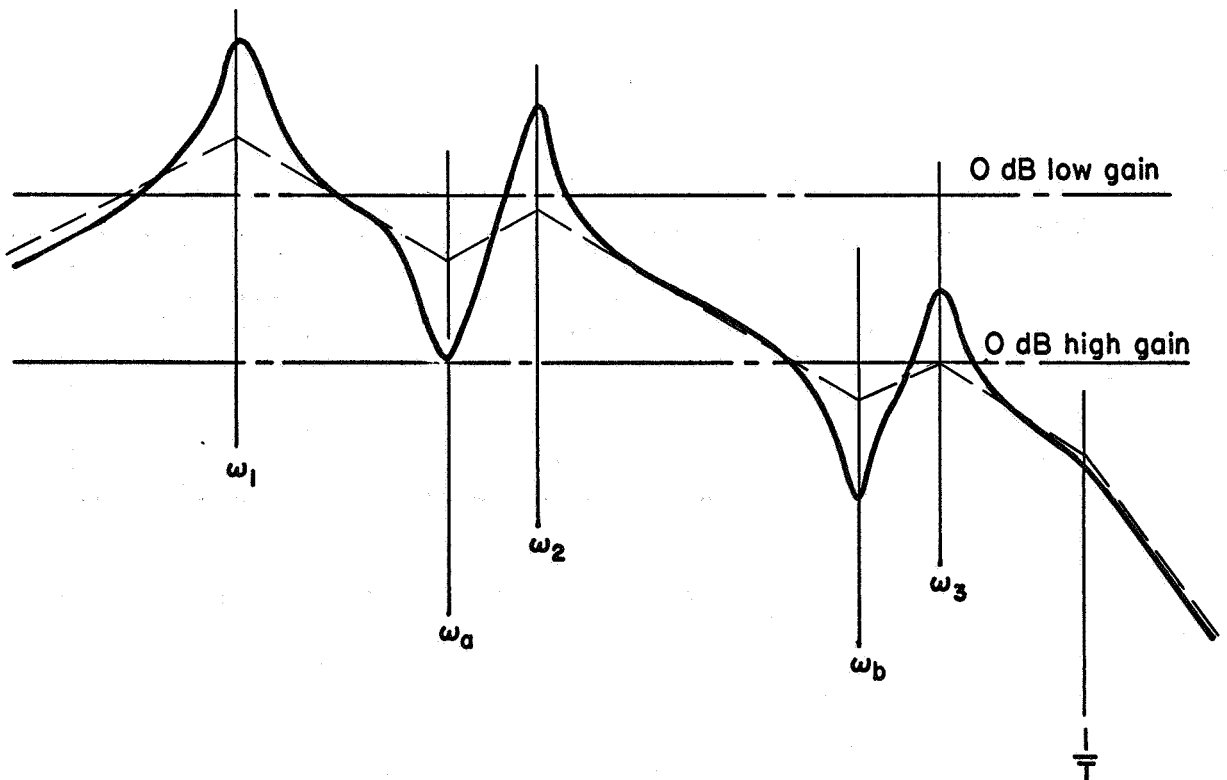

Figure B-5. Original Controller-Servo-Booster Open-Loop Bode Plot

If it were possible to modify the numerator of the airframe by relocating the sensor of q so that the numerator roots occur midway (on the Bode plot) between the adjacent booster poles (which are not affected by sensor location) then the Bode plot would appear as in Fig. B-6. Now the damping of all three modes can be increased simultaneously by having the 0 db line cut deeply into all three Bode peaks. This is the essence of the Sawtooth Bode Concept.
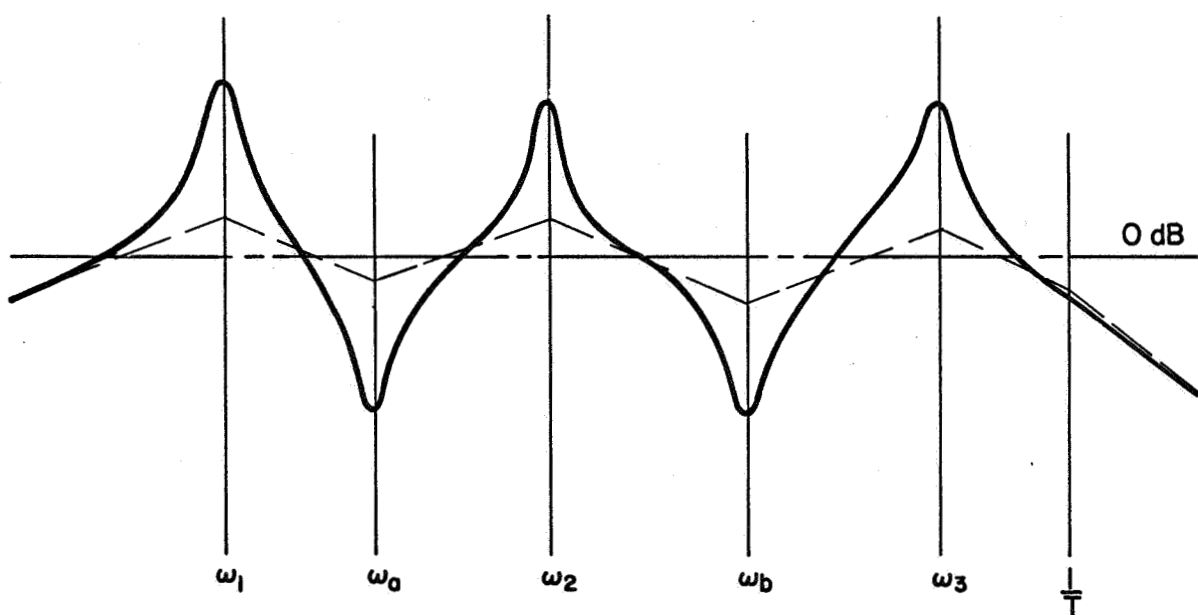

Figure B-6. Modified Controller—Servo—Booster Open-Loop Bode Plot

APPENDIX C

ADDITIONAL REMNANT DATA

GENERAL

The analyses of remnant-induced vibrations in Section VIII pointed up the scarcity of measured pilot remnant and the consequent lack of a suitably detailed and validated remnant model. Since an adequate data base is a prerequisite for modeling, some relevant remnant data obtained during the past few years at Systems Technology, Inc., is presented in this appendix. They are in the form of discrete power spectral densities, measured with various narrowband filters as described in Ref. 15.

The integral convention used here relating the power spectral density and mean-square remnant is:

$$\sigma^2 = \frac{1}{2\pi} \int_0^\infty \Phi(\omega) d\omega \qquad (C-1)$$

Several forms of remnant spectra are given, corresponding to those presented in the referenced sources. These are identified on Fig. C-1, and their relationship is given below for convenience. (Note: $Y_{OL} = Y_p Y_c$; the open-loop describing function.)

	OPEN-LOOP REMNANT (INJECTED)		CLOSED-LOOP REMNANT (MEASURED)
REMNANT REFERENCED TO:			
Pilot input (error point)	Φ_{nn_e}	$=$	$\Phi_{ee_n} \left\| \dfrac{1 + Y_{OL}}{Y_{OL}} \right\|^2$ $\quad$ (C-2)
Pilot output (control point)	Φ_{nn_c}	$=$	$\Phi_{cc_n} \left\| 1 + Y_{OL} \right\|^2$ $\quad$ (C-3)

Data will be given for the following task variables:

> Controlled element — Form and gain
> Forcing function — Bandwidth and amplitude
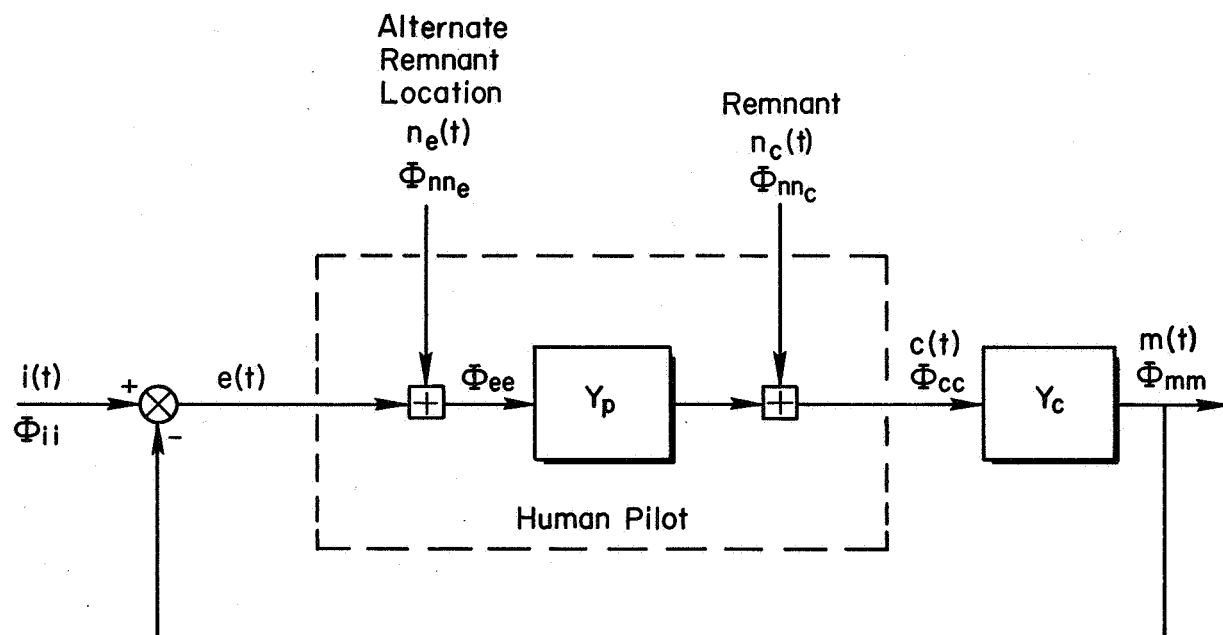> Manipulator (control stick) restraint

Figure C-1. Pilot/Vehicle System Block Diagram

The data are based, where possible, on controlled elements relevant to the booster control problem: e.g., $Y_c = K_c/s(s-1/T)$, which is an approximation to the rigid-body modes of an unstable booster; or $Y_c = K_c/s$, which is an idealization of the attitude dynamics of an augmented vehicle.

Following the short summaries of task variable effects, two environmental variables shall be considered. These will be vibration and acceleration, both highly pertinent to booster manual control.

REMNANT VARIATIONS WITH CONTROLLED ELEMENT FORM AND GAIN

Both controlled element form and gain have important influences on the pilot remnant. Reference 15 indicates that remnant increases as the controlled element gain is increased from the value for best pilot rating, but that the relative increase in rms remnant is not nearly as large as that of the gain itself.

The largest remnant differences due to the controlled element are between data for systems requiring low frequency lead generation versus systems which do not. Typical results illustrating this are shown in Fig. C-2a. Among other things, these data show a severalfold increase in the remnant level when lead (T_L) is required, and provide a strong incentive for the use of augmentation (when vehicle dynamics approximate K_c/s^2) to make Y_c "look like" a K_c/s in the region of pilot/vehicle crossover. Figure C-2b shows the effect of making a K/s^2 controlled element divergent, other parameters being equal. The remnant level increases by roughly a factor of two or more across nearly the entire spectrum.

REMNANT VARIATIONS WITH FORCING FUNCTION
BANDWIDTH AND AMPLITUDE

Variations of remnant with forcing function bandwidth, ω_i, and amplitude, σ_i, seem to be relatively minor. For instance, Fig. C-3 shows that the closed-loop remnant Φ_{cc_n} is essentially invariant with forcing function bandwidth for the first-order, divergent controlled element test results reported in Ref. 15. These conclusions are
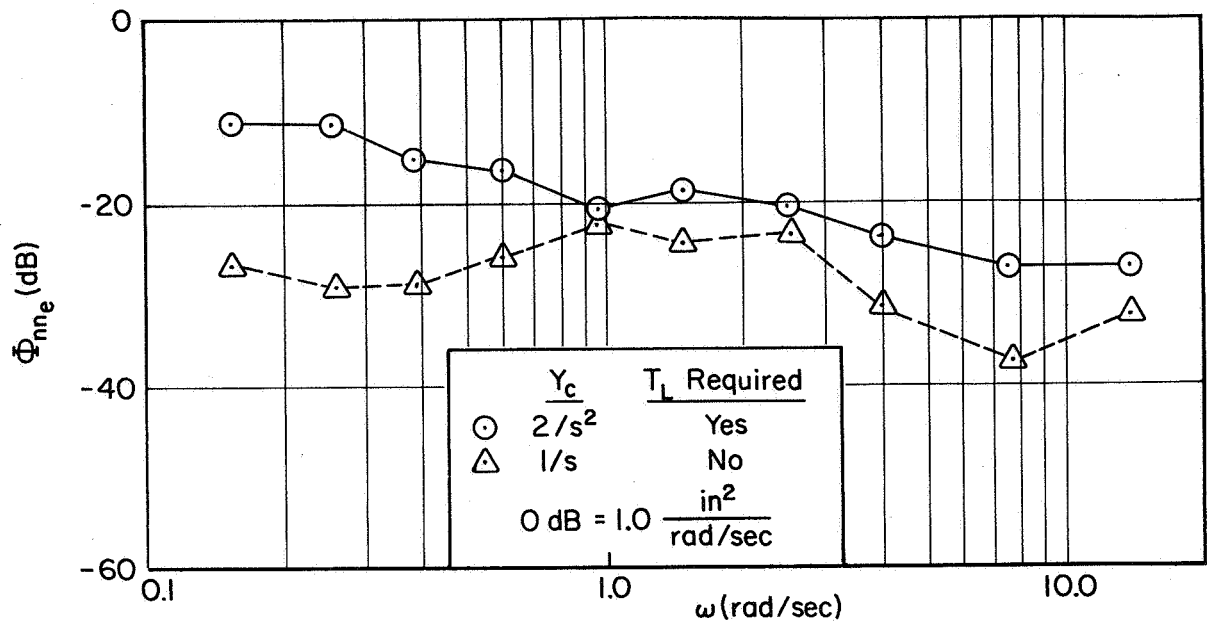
(a) $Y_c = K_c/s$, K_c/s^2, $\omega_i = 2.5$, 1/2 in., Pilot 8 (Ref. 15)
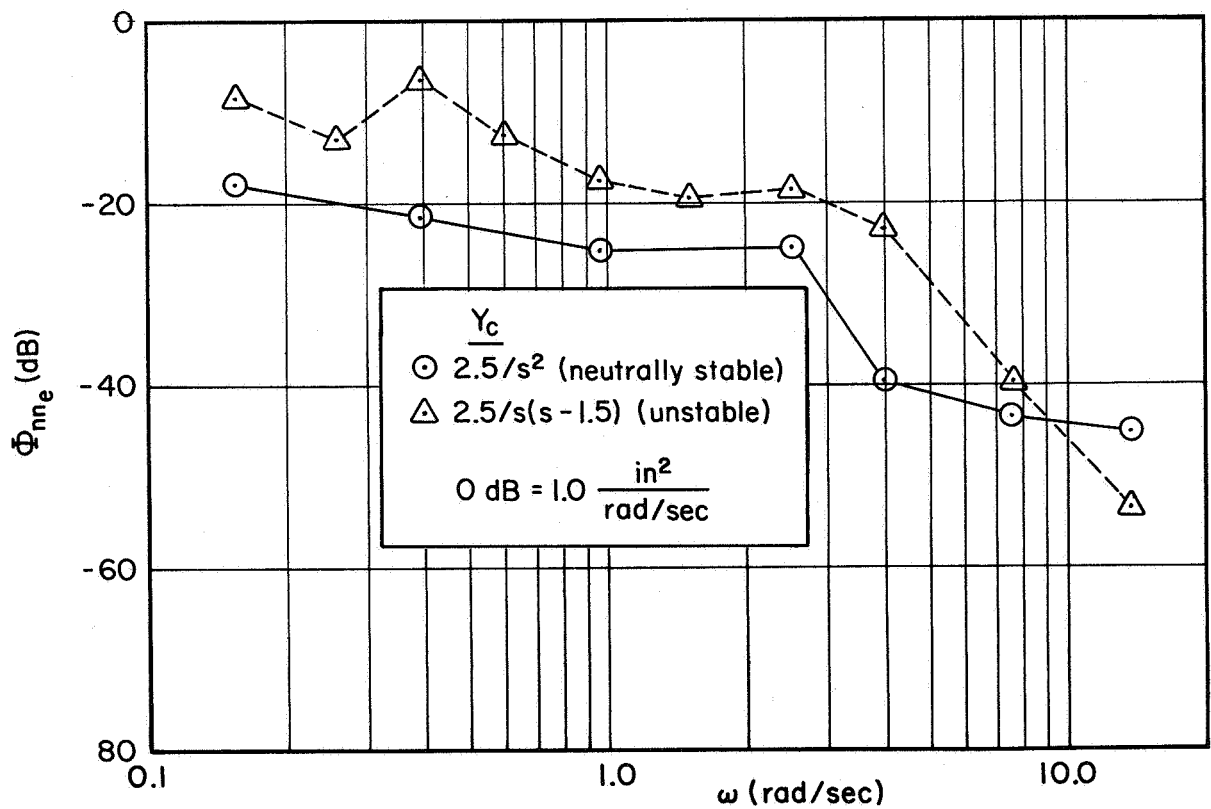
(b) $Y_c = K_c/s(s-\lambda)$, $\omega_i = 1.5$, 1/4 in., Pilot 5 (Ref. 15)

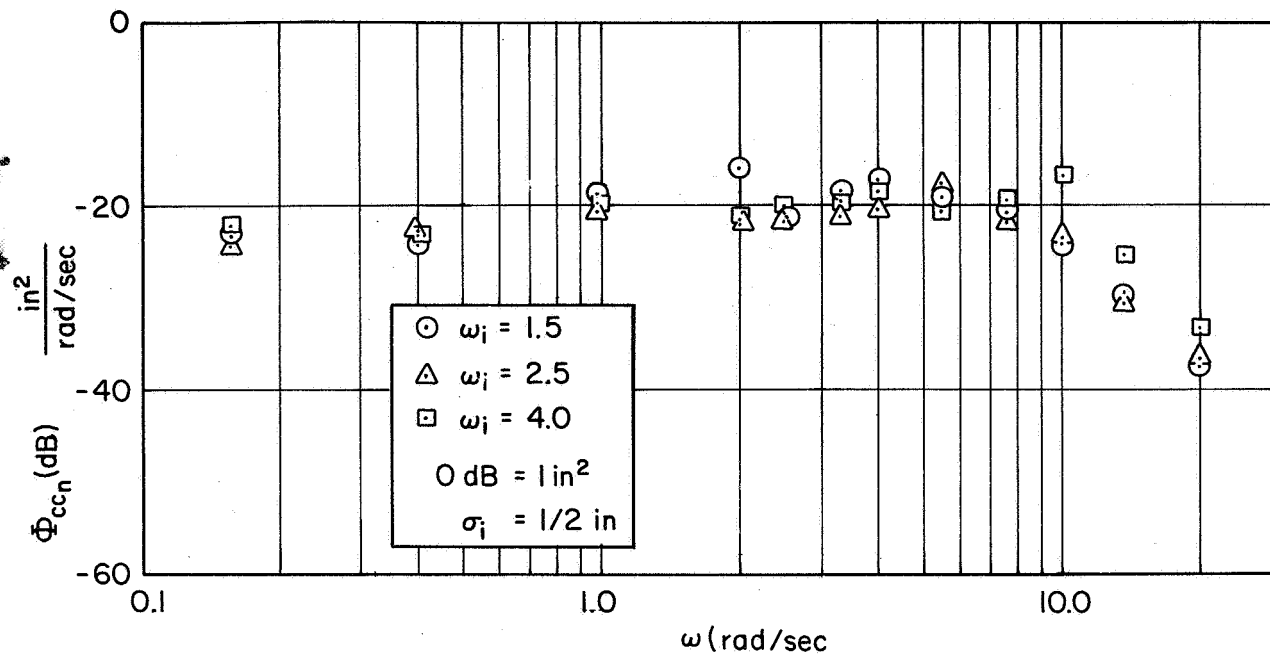Figure C-2. Effect of Y_c Variation on Open-Loop Remnant

Figure C-3. Effect of ω_i Variation on Closed-Loop Remnant;
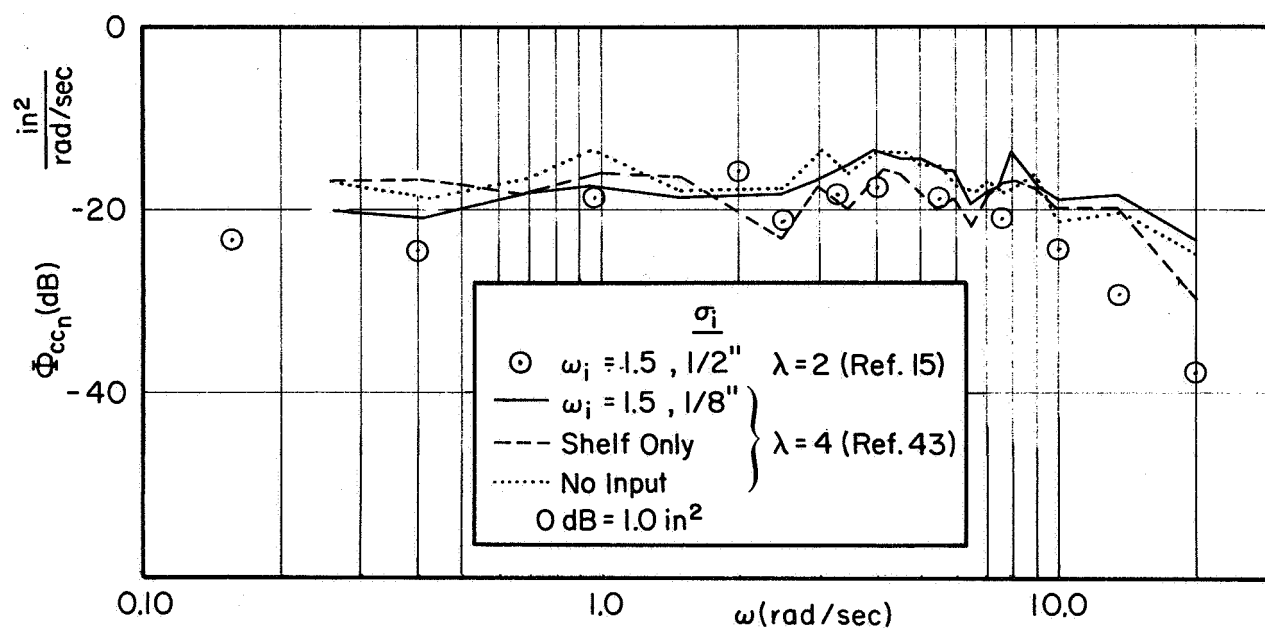$Y_c = K_c/(s-2)$ (Ref. 15)

Figure C-4. Effect of ω_i and σ_i Variation on Closed-Loop Remnant;
$Y_c = K_c/(s-\lambda)$ (Ref. 43)

are broadened by subsequent data (Ref. 43) taken with various components of the forcing function deleted and shown in Fig. C-4. Closed-loop remnant spectra were measured at successively lower input amplitudes by, first, using only the very low-amplitude shelf frequencies from the forcing function, and finally, for no forcing function at all. It is apparent from Fig. C-4 that the level of remnant does not vary widely as the input level is varied, but this result may not be general for more stable controlled elements. Also in Fig. C-3, Ref. 43 remnant data for $\omega_i = 1.5$ are shown to compare favorably with the earlier Ref. 15 runs by different pilot subjects. The remnant spectral shape with this strongly divergent first-order controlled element is somewhat wider band than most of the other remnant spectra.

REMNANT VARIATIONS WITH MANIPULATOR

The type of manipulator (control stick) can have a large effect on closed-loop tracking performance and pilot rating (Refs. 44 − 47). However, when properly designed, the manipulator influences on remnant can be made relatively minor. This is demonstrated in Fig. C-5, where remnant data for an almost rigid pressure control stick are compared with those for a spring-restrained stick. At all but low frequencies the pressure controller has a larger remnant than the spring-restrained stick, although the differences are not large.

REMNANT VARIATIONS WITH ENVIRONMENTAL VARIABLES

There are very few experiments in which describing function measurements have been taken for similar controlled elements under conditions of different external environments. There are even fewer data on the remnant. However, those that do exist (Refs. 48 − 49) show some degradation of pilot characteristics when exposed to acceleration or vibration. These degradations are primarily in describing function gain, although some subjects also exhibited remnant increases for some situations. Specifically, in Ref. 48 the imposition of either eyeballs-out or eyeballs-in accelerations caused an increase in remnant. Nevertheless, for this case the added remnant was less than the large errors due to decreased
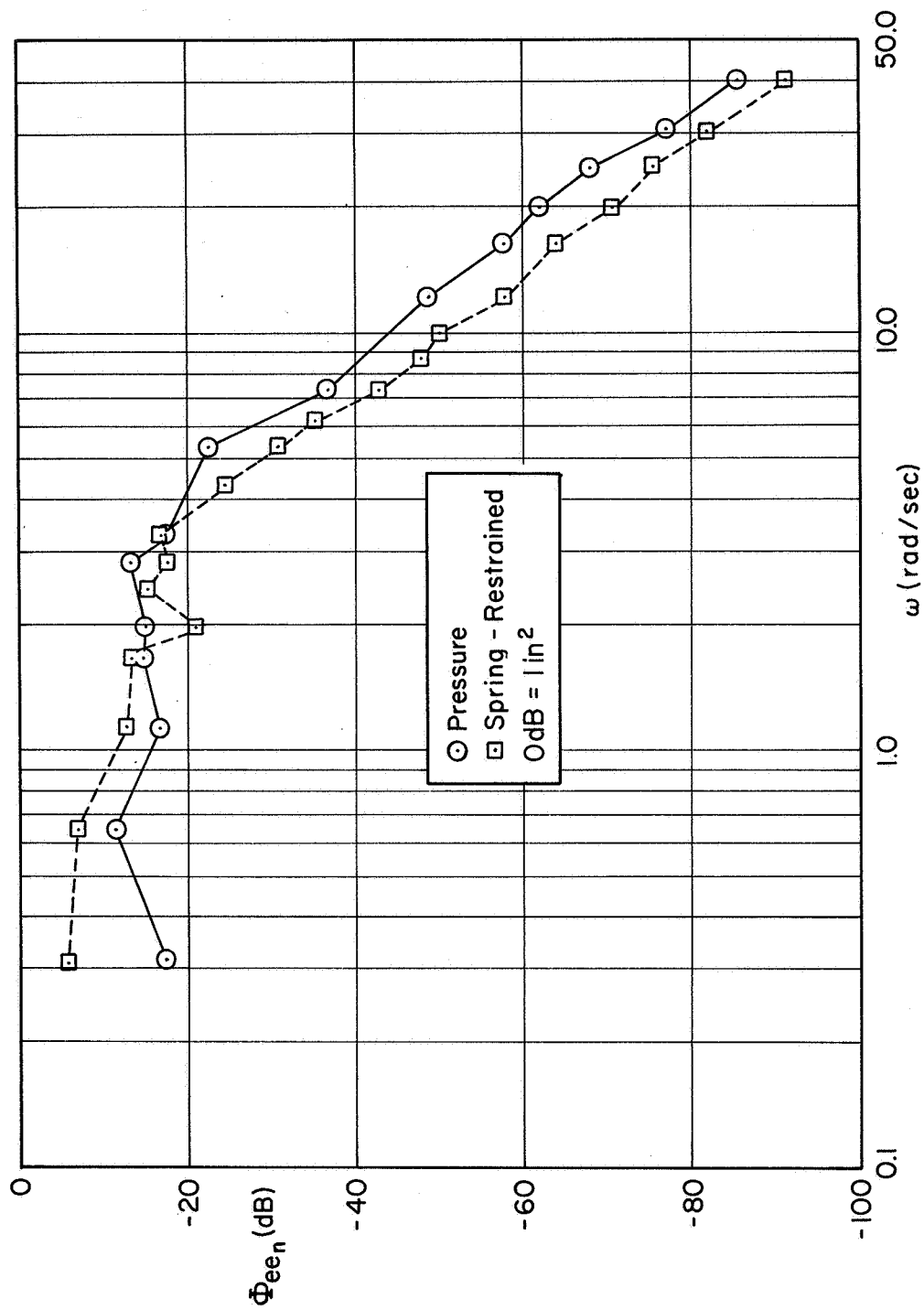
Figure C-5. Effect of Manipulator on Closed-Loop Remnant;
$Y_c = K_c/s^2$, $\omega_1 = 2.5$, 1/2 in. (Unpublished STI data)

pilot gain which also accompanied acceleration stress. An increase in remnant was also exhibited in vibration studies reported in Ref. 49. There, in a two-axis task the remnant in the plane in which vibration was effective increased with either random vibration or quasi-periodic vibration stresses. The latter vibration condition was a 5 Hz random amplitude wave which approximates a bending mode with gusty excitation. In the out-of-plane axis, vibration had little effect on remnant or describing function.